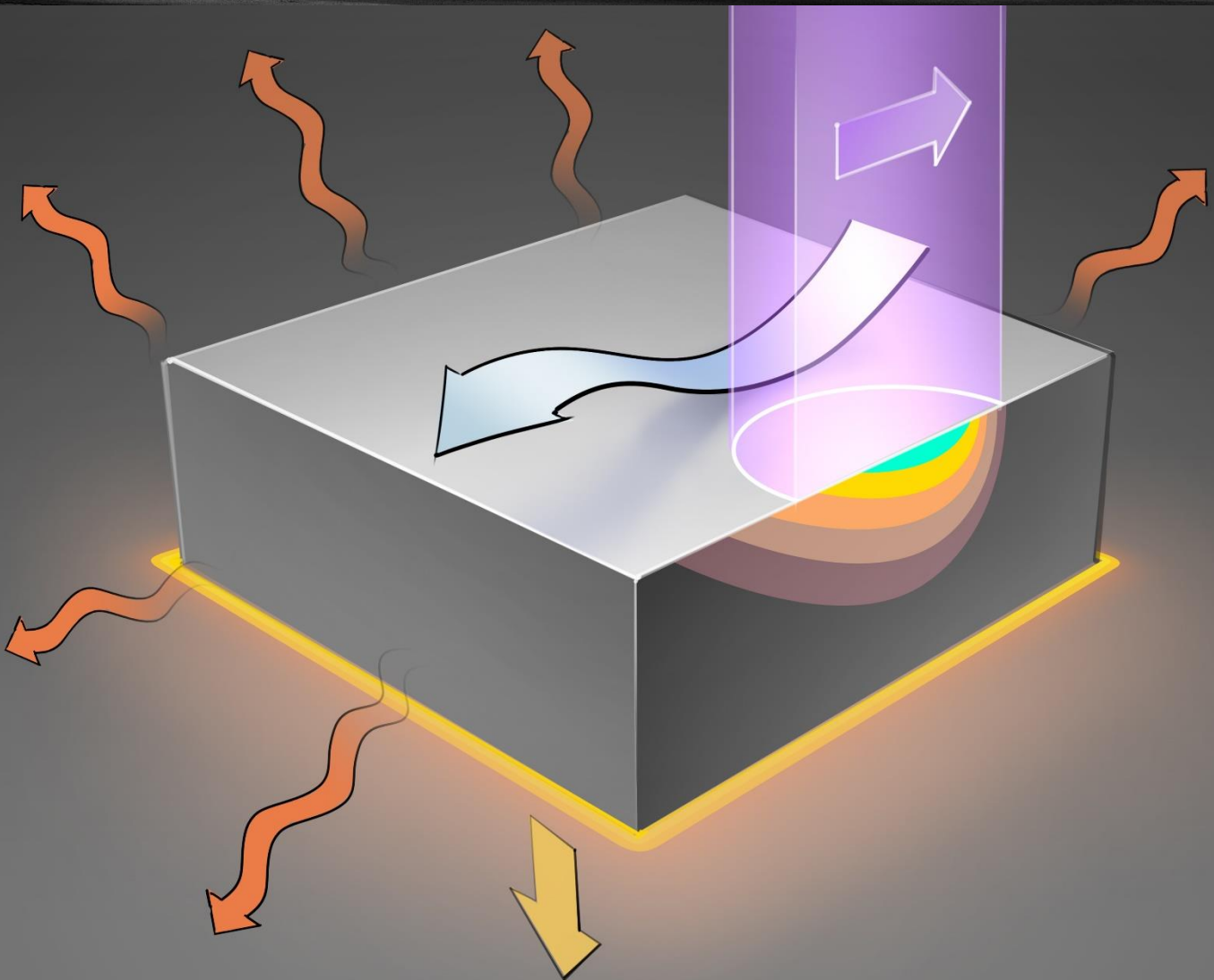


H.J. Breukelman

Architected Microstructures

The effect of localized laser heat treatment on the microstructure of a FeCNi steel



Architected Microstructures
The effect of localized laser heat treatment on the
microstructure of a FeCNi steel

By

H.J. Breukelman

in partial fulfilment of the requirements for the degree of

Master of Science

in Material Science and Engineering

at the Delft University of Technology,
to be defended publicly on Thursday August 29, 2019 at 09:30 AM.

Supervisor:	Dr. J. Hidalgo Garcia,	TU Delft
Thesis committee:	Prof. dr. M.J. Santofimia,	TU Delft
	Dr. ir. M.J.M. Hermans,	TU Delft
	Dr. M.H.F. Sluiter	TU Delft

An electronic version of this thesis is available at <http://repository.tudelft.nl/>.

Preface & Acknowledgements

This thesis regards the localised laser heat treatment of a metastable austenitic steel, which was investigated using a thermal model and microstructural characterisation of the treated samples. This work was carried out in fulfilment of the requirements for a Master of Science at Delft University of Technology in the period of September 2018 to August 2019. This thesis is the culmination of my collegiate education at the TU Delft, starting with a B.Sc. in Applied Earth Sciences, focussing on mining engineering. Various study trips, courses on extractive metallurgy and mineral processing guided me towards the Material Science and Engineering department, where I developed an interest in steel metallurgy.

This project was initiated by an informal discussion with Javier Hidalgo Garcia, regarding a poster presenting first attempts at laser treating the steel also studied in this thesis. The local creation of novel microstructures was deemed an interesting subject, and the project was started under Javier's daily supervision. I would like to take this opportunity to thank him for this first discussion, as well as all the ones that followed. From the project scope to minute details regarding etching of the material, the guidance and practical support was of immense value, for which I would like to offer my sincere gratitude. I would also like to thank Maria Santofimia Navarro, for her role as supervisor and chairwoman of the Thesis Committee. Her interesting and in-depth comments on the thesis were a tremendous help focussing the story into this final product.

Furthermore, I would like to acknowledge the help of Marcel Hermans, for all his efforts in realising the laser experiments despite equipment issues in the laboratory. For these experiments, carried out at Tata Steel IJmuiden's Product Application Centre, I would also like to express my immense gratitude to Tony van der Veldt and Robin Aaij, for hosting me at Tata and operating the equipment.

I also would like to thank various people at the Material Science laboratories, for their help and advice regarding experimental procedures and characterisation. Kees Kwakernaak, for training me to operate an electron microscope, and carrying out EBSD measurements with me. Nico Geerlofs, for guiding the dilatometry experiments despite the high heating rate's effects on the apparatus. Jurriaan van Slingerland and Remko Seijffers, for practical laser set-up knowledge and a crash course thermocouple measurements during welding experiments. Sander van Asperen for all the practical tips regarding optical microscopy. And all of the aforementioned, and many others, notably Ton Riemslog and Elise Reinton, for the great atmosphere at the lab, during my thesis work.

Lastly, I would like to thank my friends, some of whom by name. Jan, Michiel, Jaap, Stefan, Talitha, Marien, Marijn, and Javad, you have all contributed more to this thesis and my general well-being during this process than you know. Lastly, my dear girlfriend, Laura, for her patience when I was absorbed by my work, and my parents, brother, and sister, for being there, always.

*H.J. Breukelman
Delft, August 2019*

Contents

1. Introduction	11
1.1. Motivation	11
1.2. Research Question	12
1.3. Method.....	12
1.3.1. Characterisation of the Material	13
1.3.2. Modelling of the Heat Response	13
1.4. Thesis Contents.....	14
2. Literature and Key Concepts	17
2.1. Laser Surface Treatment	17
2.2. Laser Surface treatment and the Heat Equation	19
2.3. Modelling of laser surface treatment	20
2.3.1. Analytical Models	20
2.3.2. Numerical Models	21
2.4. Phases in Fe-C-Ni.....	26
2.4.1. Austenite in Fe-C-Ni.....	26
2.4.2. Martensite.....	27
2.4.3. Austenite stability	27
2.5. Fe-C-Ni Steels and the Reverse Transformation.....	29
3. Materials & Methodology	31
3.1. Material.....	31
3.2. Sample Preparation	33
3.3. Initial Heat Treatment.....	34
3.4. Initial microstructures	34
3.5. Dilatometry	34
3.6. Laser Heat Treatment	37
3.7. Light Optical Microscopy	40
3.7.1. Grain Boundary Etching.....	41
3.7.2. Tint Etching.....	41
3.8. Scanning Electron Microscopy and Electron Backscatter Diffraction	42
3.9. Combustion Infrared Detection	42
3.10. Hardness Measurements	42
4. Thermal Model	43
4.1. Finite Element Methods for Time-Dependent Heat Modelling in COMSOL Multiphysics	43
4.2. Model Set-up	45
4.3. Process Parameters	45
4.3.1. Beam Power Density and Distribution	46
4.3.2. Heat fluxes in Laser Surface Treatment.....	47
4.4. Transient Properties.....	49

5.	Results and Discussion	52
5.1.	Effect of heating rate on surface and bulk microstructures	52
5.1.1.	Phase transformation temperatures	52
5.1.2.	Microstructural characterisation of dilatometric samples	57
5.1.3.	Assessment of decarburization in the surface	60
5.2.	Model for the temperature field during laser heat treatment and validation	61
5.2.1.	General model results.....	61
5.2.2.	Temperature validation	64
5.2.3.	LAZ based validation	65
5.2.4.	Sensitivity analysis.....	66
5.3.	LAZ Microstructure Validation	68
5.3.1.	Low-Powered Laser Sample	68
5.3.2.	LAZ high-power microstructure and synthesis.....	72
5.3.3.	Hardness measurement of the high-power LAZ.....	76
5.4.	Microstructural Discussion Laser specimens.....	77
5.4.1.	Grain refinement phenomena	77
5.4.2.	Low hardness near specimen free surface.....	80
6.	Conclusions.....	82
7.	Recommendations	84
8.	Bibliography	85

Abstract

Laser surface treatments offer interesting prospects for the creation of architected microstructures formed by distinct phases in metastable austenitic steels. In the present study, a laser-based localised heat treatment was developed to locally create an austenitic region in a quenched Fe₂₅Ni_{0.2}C martensitic microstructure. The highly localised laser heat flux gives rise to high spatial gradients in peak temperature and heating rate. This results in strong variations in the microstructures observed over short distances, which are related to local changes in the martensite to austenite phase transformation temperatures and formation mechanisms, the occurrence of grain growth and recrystallization in the newly formed austenite, and the tempering of the initial martensite. Moreover, thermal stresses and surface effects influence the final microstructure. In this work, effects of heating rates and peak temperatures are studied by dilatometry whereas Electron Backscatter Diffraction (EBSD) and optical microscopy are used to assess austenite grain size and morphology. This information is linked to a Finite Element Model of the local thermal history to investigate the evolution of the local microstructure throughout the zone affected by the laser heat source. This research provides insight into localised microstructural control of steels with laser surface treatment and provides a thermal model for detailed understanding of the mechanisms controlling the microstructural changes taking place during these treatments.

1. Introduction

1.1. Motivation

Laser surface treatments are industrially applied to change the properties of the surface of a metal, without significantly altering properties of the bulk material. The localisation is one of its critical advantages and is applied when surface mechanical properties need to differ significantly from bulk properties, or when the objective of the treatment is to change a property intrinsic to surfaces, such as corrosion or wear resistance. Various treatments, such as laser surface hardening, laser remelting, and laser cladding, are applied widely in industry [5, 6]. Other laser heat treatments, such as laser heating-assisted incremental sheet forming and the creation of a variety of gradient structures are currently focal points for research [7-9].

Architected materials, also known as gradient materials, are materials in which, according to Andreev et al. [10], “specified distributions of macroscopic domains with different physical properties” are created¹. Metastable austenitic steels are suitable for this purpose, when cryogenically or mechanically formed martensite is reverted to austenite using a laser heat treatment [7, 10-12].

Architected materials have several advantages, including new combinations of strength and ductility [13]. Particular advantages of the metastable austenitic steels include the isolation of austenite, facilitating research into the effect of surrounding phases on austenite stability in TRIP steel [14, 15]. Additionally, the combination of paramagnetic austenite and ferromagnetic martensite in a single component allows for novel magnetic component design [12]. Using laser heat treatments to obtain these architected structures has several advantages in general, including high spatial control and high throughput [6]. In metastable austenitic steels, a specific advantage of laser heat treatment has been noted by Libman and Estrin [16], who note that high heating rates serve to stabilise the austenite in a wider temperature range.

Given these advantages, further research regarding microstructural development in laser surface treated metastable austenitic steels is warranted. The understanding of the creation of controlled architected microstructures using lasers is impeded by strong local variations in thermal history. Due to the localised nature of laser treatments, process control parameters affect microstructural control parameters such as heating rate and temperature. The localised heat flux causes high heating rates and temperatures in the direct vicinity of the focal spot, but the thermal path experienced by a region of the sample at a certain distance to the focal spot is changed due to heat dissipation into the bulk.

Temperature can only be measured on the component surface, with thermocouples or thermal imaging, which limits the available information. Modelling of the heat distribution for process control is also found in welding, and has resulted in various empirical, analytical, and numerical models [17-20]. Due to their respective drawbacks, none of these methods has gained universal acceptance, although numerical models based on the Finite Element Method are gaining popularity [21, 22]. The success of any thermal model, however, ultimately depends on several physical characteristics of laser-material interaction and material thermal properties. These are difficult to measure, and dependent on the thermal history.

¹ By this definition, any surface hardened component is an architected material, so it is helpful to include a distinction based on the degrees of freedom in creating these macroscopic domains. For example, in induction hardening, only the depth of the hardened layer can be controlled, and the entire surface is hardened up to this depth, the one degree of freedom for the treatment. Altering surface properties using a laser heat source moving over a steel work piece in multiple directions is more commonly described as architected.

Laser surface treatments which utilise the transformation from martensite to austenite are a novel development. Nevertheless, this transformation has been studied at homogenous heating rates of up to 100 K/s [11, 23-25], as well as high heating rates more representative of those experienced near the laser focus [4, 26, 27] in iron-nickel and iron-carbon-nickel systems. In the literature on this subject, the martensite to austenite 'reverse transformation', refers to the transformation taking place upon heating, generally known as austenitization. However, the transformation in these alloys distinguishes itself from conventional austenitization, in the sense that two mechanisms are reported: a diffusional mechanism, similar to conventional austenitization [28], and a displacive mechanism [23]. The selection of either mechanism, or a mixed mechanism, depends on chemical composition and heating rate [4, 23].

Comprehensive characterisation of laser austenitized zones (LAZ) in metastable austenite steels is scarce, despite its potential, and mainly based on magnetization behaviour [7, 10, 12, 16]. Furthermore, an interfacial zone between laser-formed austenite and parent martensite can be expected to experience lattice and thermal mismatch strain, which are likely to influence microstructure locally.

1.2. Research Question

Based on the motivation, the following research question was formulated to encapsulate the objective of this work:

Is it possible to apply localised laser heat treatments to create a distinct austenite region, from a cryogenically formed martensite, in metastable austenitic Fe-C-Ni steel? If so, to what extent do the process parameters affect the microstructural characteristics of the laser heat treated region?

This research question can be split up in the following sub-questions, leading to 4 distinct aspects of the research.

1. *What is the influence of heating rates on the martensite to austenite transformation in Fe-C-Ni metastable austenitic steel?*
2. *What are the microstructural characteristics of a work piece subjected to localised laser heat treatment?*
3. *Can a valid model be created to assess heating rates and peak temperatures throughout a work piece subjected to localised laser heat treatment, based on the treatment's process parameters?*
4. *Can the microstructural characteristics of a work piece subjected to localised laser heat treatment be rationalised based on such a model?*

1.3. Method

In this work, microstructures obtained by laser surface treatments, creating single austenite seams in cryogenically formed martensitic microstructures in the metastable austenitic Fe-0.2C-25Ni steel, are described. Various treatments were carried out using different process control settings, to investigate their effect on the microstructural development. The research question stated above requires three main aspects to be considered, corresponding to the various research sub-questions:

- Microstructure creation and characterisation, corresponding to sub-question 1 and 2. Sub-question 1 involves a dilatometric campaign assessing the effect of heating rate on the martensite to austenite transformation in the alloy. Sub-

question 2 is concerned with the laser heat treatments themselves. For both sub-questions, various characterisation methods, including optical and scanning electron microscopy, combustion infrared detection and hardness measurements, were carried out to obtain the required information.

- Model creation and validation, corresponding to sub-question 2. A thermal finite element model is created to estimate local heating rate and temperature, incorporating process and material parameters. This model is validated experimentally using thermocouple measurements, and the extent of the austenitized region.
- Microstructure and model synthesis, corresponding to sub-question 4. The relation between local thermal history and the microstructural characteristics within the laser heat treated region

1.3.1. Characterisation of the Material

An alloy, with a composition of Fe-0.2%C-25%Ni, was selected based on availability and martensite start temperature well below room temperature. Initial martensitic microstructure was formed by austenitizing in a liquid salt bath at 1200 K, followed by quenching in liquid nitrogen, to obtain martensite. This initial heat treatment was followed by martensite reversion in both dilatometric and laser surface treatment experiments, as follows:

- Dilatometry was carried out to assess phase transformation behaviour at controlled, uniform heating rates, range from 5 K/s to 1000 K/s. These dilatometric treatments were carried out to assess whether these comparisons could be drawn between the controlled heating rate samples, and points at increasing depth in the Laser Heat treated zone.
- The laser surface treatments consisted of passing an infrared Nd:YAG laser spot over the sample surface, varying laser power and velocity. These process control parameters varied within a range where surface melting could be prevented or limited to negligible depth.

Dilatometric and laser surface treatment samples were characterised with optical microscopy to characterise and compare the austenitic microstructures. A laser surface treated sample was also studied using Electron Backscatter Diffraction (EBSD) for detailed phase and orientation data.

1.3.2. Modelling of the Heat Response

The Finite Element Model is developed to obtain information on thermal history as a function of distance to the laser focal spot. This can be used, in combination with the observed microstructures from the laser surface treatment, to assess the microstructural mechanisms.

A thermal Finite Element Model (FEM) created in the commercial software COMSOL Multiphysics® [29] was used to assess the influence of laser parameters on the attained temperature, heating, and cooling rates. Three distinct sets of parameters play crucial roles in the thermal modelling of laser surface treatments:

- Thermal properties of the solid: namely heat conductivity (κ), specific heat capacity at constant pressure (C_p), and density (ρ), the three governing parameters of the heat equation. These parameters are temperature dependent, directly linked to phases present in the material, and phase transitions. These aspects are often glossed over in references, and detailed data is only available for select alloys [30]. Therefore,

combining sources and experimental data from e.g. dilatometry is used in this work for a proper assessment.

- Laser-surface interaction: radiation absorptivity is difficult to obtain by measurement or from theoretical assessment, and it strongly depends on local surface characteristics such as roughness [31]. Therefore, an estimate was made based on literature, but this parameter was subjected to a sensitivity analysis to assess the effect of a misestimate.
- Process control parameters: laser power and velocity were varied in the investigation.

1.4. Thesis Contents

This thesis presents, in Chapter 2, a general background of some essential concepts, as well as an overview of relevant literature. This literature review is concerned with the main topic of this thesis, the reversion of martensite to austenite in metastable austenitic steel and Fe-Ni alloys, and laser surface treatment modelling. In section 2.1, the microstructural mechanisms of the martensite to austenite transformation are presented, and the effect of heating rate is discussed. The prevailing laser surface treatment models are discussed in section 2.2, and assessed for applicability to the architected microstructures in metastable austenitic steels. In section 2.3, essential concepts which relate to phases in the steel under consideration are discussed, such as non-equilibrium phases, phase morphology, and transformation kinetics.

Chapter 3 describes the methodology of the experimental work: Dilatometry, Laser Heat Treatment, and characterisation methods including optical and electron microscopy, as well as Combustion Infrared detection.

In Chapter 4, the model is described. Section 4.1 and 4.2 discuss the mathematics of the Finite Element Method and the adaptive time-stepping algorithm employed by the software. Section 4.3 deals with the model set-up proper, containing details necessary for the practical operation of the model. This section contains subsections dealing with the physical parameters involved with the model, and the way in which these are implemented. This includes, in 4.3.1, the process parameters available for laser heat treatment, in 4.3.2, the heat fluxes which describe the way heat flows into, and out of, the modelled domain, and in 4.3.3, the transient properties of the metal, which govern the heat transport behaviour within the model.

Chapter 5 is divided into six sections, which are concerned with the main results of the research, and discussions of the result sections. In the first, the effect of heating rates as studied by dilatometry are presented. This contains subsections regarding the critical temperatures for phase transformation, and the effect of using hollow samples. This section also includes the results from combustion infrared measurements to measure the carbon content of select dilatometry samples, and the microstructures formed by dilatometry. Since these results present a self-contained part of the research, the preceding results will be discussed in section 5.2. In section 5.3, the model results are presented and the model is validated using measurements of the extent of the laser austenitized zone and thermocouple data obtained during treatment. In section 5.4, a discussion on the validation is given, considering the effect of a selection of parameters on model results. In section 5.5, laser treatment results are presented for two cases, a low-power, small spot sample, and a high power, large spot sample. The microstructure are shown, using optical and electron microscopy, as well as hardness testing. In section 5.6, this microstructural information is discussed and combined with model data and information obtained from dilatometry, and a microstructural development mechanism is posited based on the presented data.

In chapter 6, conclusions of the research project are presented. Some conclusions are given regarding the separate areas of research: dilatometry, model, and laser treatment, as well as overall conclusions on the project.

Finally, in chapter 7, recommendations are listed for further research in the field of laser austenitization and modelling thereof. This includes practical recommendations for the characterisation of laser treated Fe-C-Ni specimens, recommendations for the further substantiation of the conclusions reached in this work, and recommendations for the application of this work.

2. Literature and Key Concepts

In this chapter, a general background on laser surface treatments and the heat equation, describing heat conduction in solids, is provided. The heat equation forms the basis for analytical and numerical thermal models, which aim to provide thermal information. This thermal information can be used to understand the steel microstructures formed at increasing distances to the focal spot. The chapter continues with the microstructural characteristics of the steel, starting with a general introduction. Following that, a more detailed discussion of the phases and the reverse transformation phenomenon in Fe(-C)-Ni systems is discussed.

2.1. Laser Surface Treatment

The laser surface treatment of metals involves local using a source of coherent electromagnetic radiation, i.e. laser light, generally of infrared wavelength. These treatments are carried out to alter surface or microstructural properties, in order to provide beneficial effects to surface hardness, wear, and corrosion resistance [1, 2]. The use of a lasers with this purpose has been industrially viable since the introduction of reliable high-power CO₂ lasers in the 1970's [1]. The generally recognised advantages of laser surface treatments include spatial localisation, high processing speed, and limited process distortion [1, 3].

In Figure 1, a general overview is presented of laser surface treatments, adapted from Römer [4]. It shows a work piece and an impinging laser beam. Absorption of the laser radiation takes place at the surface, and in the work piece up to the optical penetration depth. Heat is conducted into the work piece bulk, creating a transient temperature field. The work piece and the laser are in relative movement, to subject a larger surface area of the work piece to the laser beam.

Although many types of laser surface treatments exist, two main classes can be distinguished based on the surface peak temperature in the laser focal spot.

Non-melting laser heat treatments

The first class of laser surface treatments occurs when the peak temperature does not exceed the melting temperature of the material, the resulting temperature field is governed only by heat conduction in the bulk, and the surface microstructure undergoes only solid state phase transformations, up to a limited depth. The laser surface treatments in this class include transformation hardening and annealing, post-weld heat treating, and local softening for improved formability [2, 5, 6].

Melting laser heat treatments

In the second class of laser surface treatments, peak temperatures exceed the melting temperature (T_m) of the work piece material. In this case, the molten material transports heat by convection as well as conduction, as shown schematically in Figure 1. Natural convective flow caused by the thermal gradient, as well as Marangoni flow, caused by surface tension gradients [7], play significant roles in convective heat transport. This additional mode of heat transport has a significant effect on the temperature field in the work piece. Laser remelting and laser cladding, where material is added to the melt pool to create a surface layer with a different chemical composition, are examples in this class.

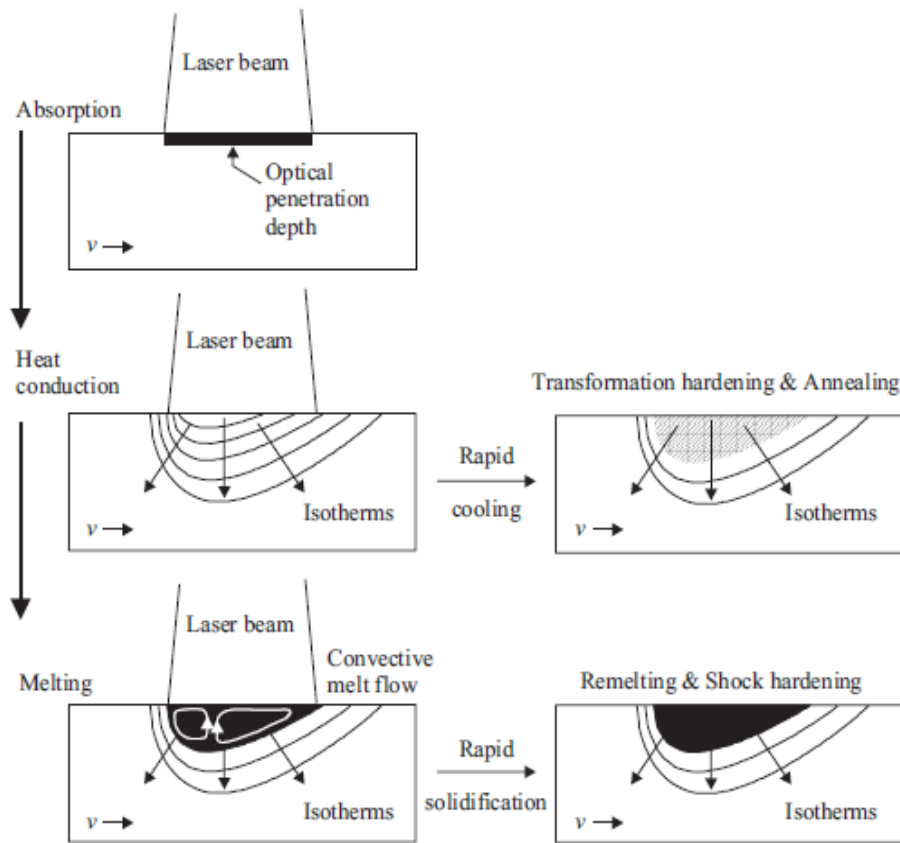


Figure 1: Laser surface treatment schematic adapted from Römer [4]. Of note here is that the workpiece is moving with velocity 'v' in the direction

The absorption mechanism at temperatures above T_m develops an effect known as *keyholing*, where local vaporisation and ionisation creates a depression in the work piece surface. This depression, and the plasma present at its surface, experience a significant increase in absorptivity due to inverse Bremsstrahlung and the internal reflection and reabsorption on the depression walls [6], which causes higher temperatures, an increase in the depression, and therefore, a significantly increased depth of laser penetration. This class, therefore, includes laser welding, laser cutting, and shock hardening, the latter not dependent on the keyhole, but on the shock wave generated by the plasma blow-off [8].

While the latter class of laser surface treatments is not applicable to the localised laser heat treatment proposed in this project, a substantial part of the literature on laser surface treatment relies on work in this field, in part due to the relative abundance of (laser) welding modelling, and useful parallels can be drawn [6]. Furthermore, the keyholing process can occur as a runaway reaction by a positive feedback loop between a small depression which increases the absorptivity, enlarging said depression. This should be taken into account for the processing window, i.e. the set of laser parameters controlling the surface treatment, available for treatments of the first class.

2.2. Laser Surface treatment and the Heat Equation

The thermal modelling of laser surface treatments relies on the understanding of the heat input and heat flow within the material, which is discussed in this section, starting with the heat input. Laser radiation is absorbed by the material by Fresnel Absorption [32], where the laser's electromagnetic radiation accelerates conduction band electrons in the surface of the metal. This process can only take place in a layer up to a few nanometres thick, which corresponds to the optical penetration depth of the material for light of the laser's wavelength [18, 33]. The accelerated electrons collide with other lattice components, such as the crystal ions and phonons, to generate heat [31, 33, 34]. This absorption mechanism results in high heating and cooling rates, but a low overall heat input, when compared to flame or plasma spraying [18], which facilitates highly localised heat treatments, both in terms of the surface area that is affected, as in the penetration depth of the surface treatment.

Due to the limited volume where the Fresnel Absorption takes place, heat conduction into the solid determines the heating and cooling rates, as well as peak temperatures, in most of the laser-affected zone [32]. The parameters heating rate V_h , cooling rate V_c , and peak temperature T_p , collectively referred to as the thermal history, vary with increasing distance to the laser focal spot. The transport phenomena controlling this spread of heat are governed by the Heat Equation.

The governing equation for Heat Transfer problems, the Heat Equation, is a parabolic partial differential equation, and can be stated as follows [35] in equation 1, the elementary heat equation:

$$\rho C_p \frac{dT}{dt} - \nabla (\kappa \nabla T) = q \quad (1)$$

Where κ [W/(m K)] is the thermal conductivity, a material property quantifying a materials ability to conduct heat. C_p [J/(kg K)] is the specific heat at constant pressure, and ρ [kg/m³] is the density of the material. These three parameters are the thermal properties of the solid. q denotes the heat fluxes in the work piece.

With algebraic rearrangement, the following equation is obtained:

$$\frac{\partial T}{\partial t} = \frac{\kappa}{\rho C_p} \left(\frac{\partial^2 T}{\partial x^2} + \frac{\partial^2 T}{\partial y^2} + \frac{\partial^2 T}{\partial z^2} \right) + \frac{q}{\rho C_p} \quad (2)$$

Equation 2 shows the change of temperature with time is proportionally to the second derivative of temperature with respect to the position, and the constant of proportionality is given by equation:

$$\alpha = \frac{\kappa}{\rho C_p} \quad (3)$$

Where α [m²/s] is referred to as the thermal diffusivity, i.e. the rate at which spatial temperature variations smooth out over time. It can be noted that this represents the ratio of a transport term, κ , and a storage term, ρC_p . The heat flux term is divided by ρC_p , also known as the volumetric heat capacity [J/(m³K)], a material property which relates the heat flux [J/(m³s)] to a temperature change.

The transient heat equation results in a rapid change in temperature at a given point where large spatial thermal gradients exist. This has two important consequences:

1. The rapid heating rates induced in the Fresnel absorption region are rapidly spread throughout the work piece, resulting in high heating rates at depth [18].
2. The heat spreads from the laser focal spot evenly in all directions in an isotropic solid. This causes high cooling rates, and a decrease in heating and cooling rates, as well as peak temperature, with increasing depth [36].

The second consequence is often referred to as the process of self-quenching [6, 18, 32], and is the main mechanism responsible for laser transformation hardening.

2.3. Modelling of laser surface treatment

In localised treatments, where temperature gradients exist, information on the thermal history data with spatial continuity into the sample bulk would aid the understanding of microstructural development taking place in the material. However, no temperature measurement methods exist to measure internal temperature distributions. High-resolution, high speed thermal cameras have been used to provide spatially continuous data on surface temperatures [5], but more commonly, point measurements such as thermocouples, or average measurements such as radiation pyrometers are used [4]. Modelling the thermal response during laser surface treatment is therefore required, whether it is to avoid 'costly trial-and-error experiments' designing the laser heat treatment [1], on-line process control [4], or to assess microstructural development [13, 14]. The necessity of physical models, according to Steen and Mazumder [15], prominent early researchers in the field of heat transfer models for laser material processing, is related to the fact that *"the experimenter is faced with a multiparameter problem which is difficult to solve without extensive factorial experimentation"*, whereas *"A model capable of predicting experimental results means that previously unmeasurable parameters can be estimated"*. The preceding notes describe the need for modelling from an operational point of view, but also mention explicitly that in these models are concerned with estimation of unmeasurable parameters, such as temperature development at a given depth in a non-uniformly heated specimen. This estimated thermal data throughout a specimen can, given a model of acceptable accuracy, be used to consider how local microstructural development has taken place based on local heating and cooling rates, and peak temperatures.

2.3.1. Analytical Models

The first models regarding laser surface treatments were attempts at an analytical solution to the problem of a moving point source of heat, notably by Rosenthal [37], which was later expanded upon by Nunes [38]. Although various assumptions have to be made in order to obtain an analytical solution, they lend themselves to efficient and accurate calculation in regions where these assumptions are valid [19]. A variety of these analytical models are excellently compared by Mackwood and Crafer [32]. This work shows the progress from Rosenthal's initial model, which assumed a dimensionless point source and infinite thickness of the work piece, to models where infinite temperatures and dimensions are eliminated. Early significant advances towards transformation hardening, i.e. laser surface treatments without a melt pool, were made by Shercliff, Ashby, Easterling *et al.* [36, 39-41]. The use of two dimensionless process parameters, representing the beam power and beam traverse rate, are defined by these authors as presented in equation 4:

$$q^* = \frac{Aq}{r_B \kappa (T_m - T_0)} \quad (4)$$

Where the dimensionless beam power (q^*) is a function of absorptivity (A), laser power (q), the spot size (r_B), thermal conductivity (κ) and the temperature difference between initial

temperature T_0 and melting temperature T_m . The dimensionless beam power is the critical parameter for the peak temperature, due to the relatively low heat conduction fluxes when compared to the beam power [36]. The case depth, however, depends strongly on the dimensionless travel rate, which basically gives an inverse measure of the interaction time, and is given by equation 5:

$$v^* = \frac{r_B v}{\alpha} \quad (5)$$

The dimensionless travel rate v^* is determined by the spot size, beam velocity (v), and the thermal diffusivity. These parameters are sufficient to describe peak temperatures and heating rates, i.e. the thermal cycle, at an arbitrary depth in semi-infinite work pieces. This representation of the main parameters in the process modelling of laser surface treatments is ubiquitous in the literature, where they are often simplified to beam power density and beam interaction time [33, 42].

However, analytical solutions like these developed have been limited to assumptions of steady-state, constant (average or room temperature) thermal properties, and faced significant problems implementing latent heat, called the Stefan problem, named after an early assessment of solutions to the heat equation when accounting for phase change published by Stefan [32]. Although these models have now been succeeded by numerical models, many validated assumptions from these analytical models are components of the numerical models, for the sake of model simplicity, model convergence, and computational efficiency [21].

2.3.2. Numerical Models

Due to the advent of increased computational power, the predominant models for heat transport in laser surface treatment is now based on numerical simulations, mostly using the Finite Element Method [32]. Initial numerical models, appearing in the 19760's and 1970's, were severely limited by computational performance at that time [20]. Due to progress in computational capacity, increasingly advanced models for laser surface treatments have been proposed in recent decades [32].

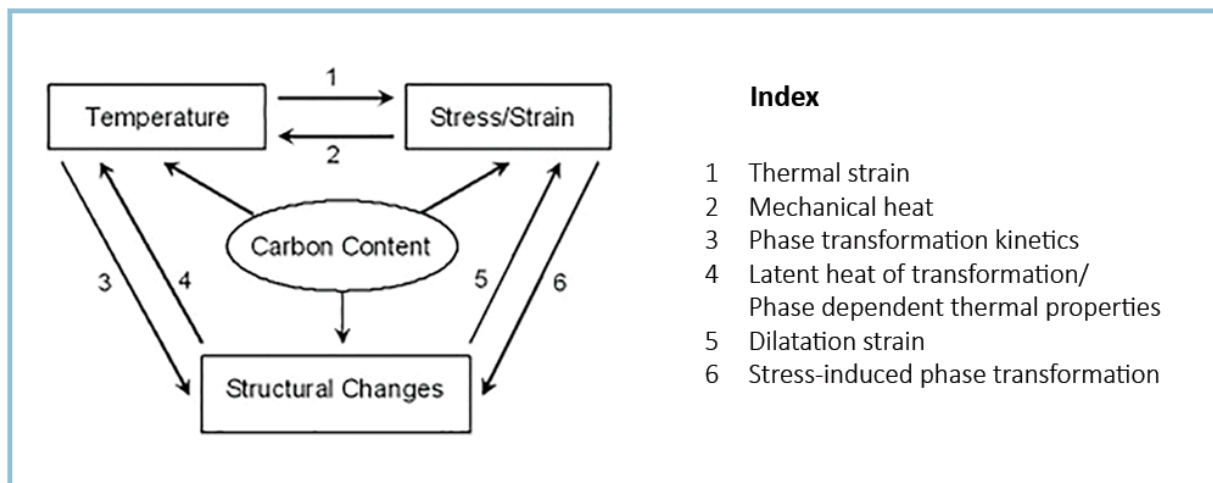


Figure 2: Metallo-thermo-mechanical coupling diagram [24] with reading key on the left

A complete description of laser surface treatments using a Finite Element Model requires the consideration of thermal gradients, the mechanical state in the material, and its microstructure, which are linked by 'metallo-thermo-mechanical coupling' [43], referring to several important interactions between the three main phenomena in laser surface heating, Temperature Field, Stress and Strain State, and Microstructure and Microstructural Changes. These phenomena interact through coupling effects, which include thermal strain (temperature and stress state),

strain-induced phase transformations (stress state and microstructure) and the latent heat of phase transformation (microstructure and temperature), create difficulties in numerical modelling of laser surface treatment due to their complexity. This complexity is compounded in steels due to the presence of carbon and its strong influence on both thermal properties and phase behaviour. Therefore, laser surface treatment models usually do not consider all three processes, and neglect a portion of the coupling effects.

A non-exhaustive but representative overview of thermal models relating to laser surface treatments is presented in Table 1. These models mostly relate to the laser surface hardening of steels, except Pariona et al. [21], who consider laser surface remelting, and Telrandhe et al. [22], who do consider laser surface hardening, but of a common aerospace alloy, Ti6Al4V. These have been included based on their merits in the modelling of laser-surface interactions (Telrandhe) and modelling description (Pariona).

Table 1 shows the following aspects for each of the models:

- 'Model type' shows the computational method(s), the sample geometry, and the laser surface treatment type
- 'Process Parameters' are listed in the next column, and show whether actual laser parameters were part of the modelled approach, and if so, whether models were compared for various laser parameters.
- 'Material parameters' shows in which manner the thermal material parameters were included in the discussed models. Notably, most authors either implement simplified thermal parameters, or neglect to state how the thermal parameters were implemented.
- 'Heat Fluxes' is a summary of the ways heat transport into, and out of, the model domain is modelled, as well as the transport phenomena within.
- 'Modelled Phenomena' describes, based on the Metallo-thermo-mechanical coupling diagram (Figure 2), which phenomena are modelled, adding some notes on the specific nature of the coupling effects. None of the models described in these publications account for the entire metallo-thermo-mechanical coupling diagram, although Miokovic et al. [44] account for more coupling effects than the other models, except for Bailey et al. These two models are discussed here separately in following paragraphs.
- 'Laser Surface Interactions' gives an overview of how the laser-material interaction is modelled in terms of aspects such as beam distribution and absorptivity.
- 'Main outputs' provides the overall results authors aim to achieve with their model. Comparisons are made between the model and resultant microstructure or hardness profiles, since most of these models are concerned with laser surface hardening. In these respects some models, notably Patwa et al. [45], perform quite well, with close correspondence between the phase transformation isotherm and case depth. However, the only authors reporting on estimated heating rates, Orazi et al. [46], report values in the order of 10^5 K/s, which they note to be unrealistically high.
- 'Notes' gives some additional information on model specifics not represented by the other categories.

The comparatively large amount of the metallo-thermo-mechanical phenomena and coupling effects accounted for by Miokovic et al. [44] are facilitated by an exceptional model geometry, which lends itself to a 2D approach with an effectively uniaxial heat conduction problem. Furthermore, they are able to disregard laser-surface interactions and process parameters, due to a sophisticated pyrometry-based control mechanism for their experimental set-up, which allows for the treatment of the model laser heat flux as a set time-temperature cycle. Based upon dilatometric experiments at high heating rates, a mathematical model for phase transformations during rapid heating is proposed by the same authors in an earlier paper, based on the Avrami-function [47]. Overall, their main results are the development of phase

fractions over time and depth, alongside a resultant hardness prediction based on these phases.

Bailey, Tan, and Shin [43] also present an interesting solution scheme, where a finite volume thermal-kinetic model is used to generate both thermal history and phase history. The thermal and phase history are implemented in a FEM Residual Stress Model which uses these inputs to calculate thermal strain, dilatation strain, and transformation-induced plasticity strain. This results in a rather complex solution scheme, due to the various numerical models involved. This model has some merits which set it apart from the other models, due to the inclusion of all phenomena from the metallo-thermo-mechanical diagram, and several coupling effects.

Table 1: (Next Page) Comparison of numerical models for laser surface treatments. Reading key for the column on modelled phenomena based on the Metallo-thermo-mechanical coupling diagram presented in Figure 2. Here, Temperature, Stress, and microstructure denote the modelled domains, and the numbers denoted the included coupling effects, e.g. 1,3 denotes the inclusion of coupling effects Thermal Strain (1) and Phase Transformation Kinetics (3).

	Model type	Process Parameters	Material Parameters K, ρ, c_p	Heat Fluxes	Modelled phenomena	Laser-Surface Interactions	Main Outputs	Notes
Pariona et al (2016) [21]	3D Transient FEM Flat work piece Laser Surface Remelting	Single set of values, Constant	T-dependent Data from Thermocalc and Comsol	Laser surface (Gaussian beam) Convective (melt pool) Convective (external) Conductive Radiative	Temperature 4: Latent heat of melting only	Constant emissivity, absorptivity. Gaussian Beam	Thermal Field Comparison between computational efficiency of single- and multigrid.	Multigrid methods
Orazi et al (2010) [46]	3D Transient FDM Flat work piece Laser Surface Hardening	Constant spot size, variable laser power and velocity	Stated to be T-dependent, no data given.	Laser surface Conductive	Temperature 3: Pearlite to Austenite transformation time. Microstructure Extent of pearlite dissolution T and t dependent.	None described	Thermal model overestimates heating rates by a few orders of magnitude. Useful process design model of hardness profile.	Bases hardness profile on linear distribution of pearlite to austenite transformation times.
Patwa et al (2007) [45]	3D Transient FVM Rotating cylindrical work piece Laser movement along cylinder main axis Laser Surface Hardening	Variable power intensity and laser velocity	Linearly T-dependent between 300 and 1100 K ($\approx A_3$), constant elsewhere. Includes microstructural parameters for hardness prediction	Laser surface Conductive Advective (stationary mesh – rotating geometry) Stored heat (enthalpy) Radiative Convective (external)	Temperature 3: Pearlite dissolution, carbon diffusion, martensite fraction CCT + %C. Carbon Content Microstructure	Coating for increased absorptivity	Model A ₁ isotherm (≈ 1000 K) corresponds closely to micrograph case depth profile	Kinetic model for pearlite and ferrite dissolution for hardness prediction
Miokovic et al (2006) [44]	2D Transient FEM Symmetric cross section of work piece on heat sink Laser surface hardening	None, directly applied T(t) profile as flux	T- and phase dependent Phase transitions based on experimentally validated Avrami-approach.	Convective (external) Radiative Conductive (approx. uniaxial)	Temperature 1, 3, 4 Carbon Content Microstructure (extensive discussion in text)	None	Detailed kinetic data on phase volume fraction as a function of depth. Hardness profiles and phase contributions to hardness.	Due to 2D geometry and simplified laser heat flux, detailed kinetic model could be implemented.
Telrandhe et al (2018) [22]	3D Transient FEM Rotating cylindrical work piece Laser movement along cylinder main axis Laser surface hardening	Constant beam radius Variable laser velocity Adaptive laser power model for constant case depth	K, c_p T-dependent	Laser Volume (Spherical Gaussian based on Goldak, [48]) Convective (external) Conductive Radiative	Temperature 3: CCT Microstructure	Volume flux Extensive analysis of absorptivity, dependence on laser velocity.	Accurate case depth prediction from thermal model, case depth equivalent to phase transition isotherm. Absorptivity equation. Variable laser power model.	Full surface hardening of the cylinder, so variable power adaption proposed to account for heat accumulation.
Bailey et al. (2009) [43]	3D Transient FVM/FEM hybrid model Flat work piece	Rectangular beam profile, one set of process parameters	K, c_p T-dependent	Laser Surface Convective (external) Radiation	Temperature 1,3, 5 Carbon Content Microstructure Stress	Absorptivity Constant (0.68)	3D Thermal, Microstructural and hardness outputs, residual stress state.	FVM for thermal-kinetic model, FEM for stress analysis

An important aspect to note from the overview given in Table 1, aside from the discussion of Miokovic et al. [44] and Bailey et al. [43], is that the effect of structural changes on the temperature field is rarely considered. When temperature-dependent thermal parameters are used, they tend to be considered linear functions of temperature [22, 45], or only considered to change significantly upon transition to the liquid phase [21].

The exclusion of phase-dependent parameters has the advantage of a simpler solution scheme for coupled models. When coupling effects between two phenomena, e.g. temperature and microstructure, are only considered in a single direction, the model approach is sequential. Considering only phase transformation kinetics in this case, a thermal model can be employed without microstructural input, instead requiring only bulk thermal properties which are implemented over the entire model domain. This scenario, represented in Figure 3 (left), leads to a sequential modelling scheme, where thermal history can be obtained as an output, and used to assess the microstructural development separately from the microstructures influence on the thermal history. This sequential scheme is more computationally efficient, since there is no input required from the microstructural model at every time step. The more iterative approach needed for bidirectional coupling is denoted by the input-output loop represented in Figure 3 (right), for the example case of the coupling effects between temperature and microstructure. A feedback loop between temperature and microstructure is run at every time step in such a model, increasing computational time, for the sake of including microstructural information in the temperature estimation.

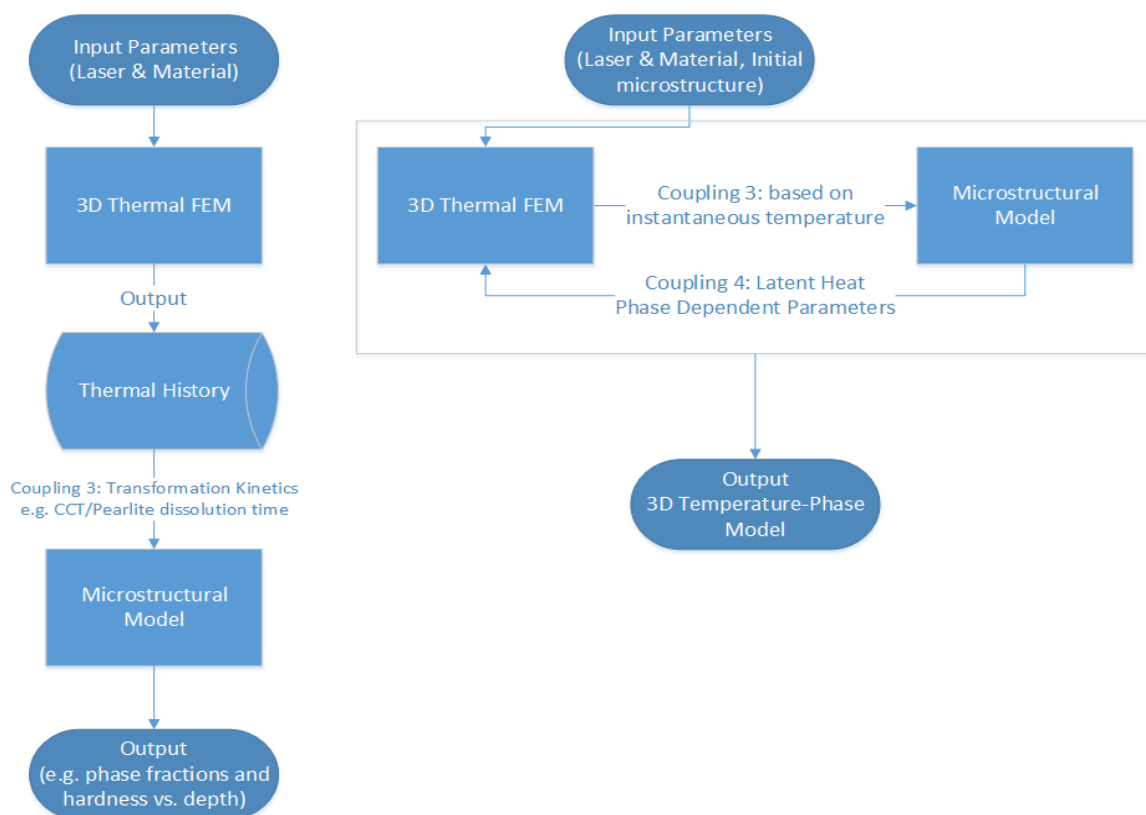


Figure 3: Unidirectional coupling solution scheme (left) and bidirectional coupling solution scheme (right)

However, the unidirectional coupling approach neglects the solid state phase transformations in steel, which are associated with:

1. Significant changes in density and specific heat capacity, and therefore, the heat conduction behaviour.
2. The effect of latent heats of transformation, which are also neglected in these approaches, may constitute a significant heat sink during heating, i.e. energy used in the transformation is not available for further heating of the material.
3. Phase transformations and thermal properties taken to be only dependent on temperature, rather than on temperature and phase, which results in the significant changes in microstructure, inherent to laser surface treatments, being ignored.

2.4. Phases in Fe-C-Ni

The material used in this work is an austenitic steel with the chemical composition Fe-0.2%C-25%Ni. The austenitic nature refers to room temperature (meta)stability of the austenite phase. In this work, the microstructure of this steel must first be converted to a different bulk microstructure, known as martensite. Following this, the austenite is created by the localised laser heat treatments. For this steel, the martensite can be obtained either at cryogenic temperatures, or as a response to the application of strain [49]. Martensite, austenite, and the martensite to austenite reverse transformation that takes place upon heating are the subject of the following sections.

2.4.1. Austenite in Fe-C-Ni

Austenite, or γ -phase, is a Face Centred Cubic (FCC) phase of steel, and an equilibrium phase at temperatures above 727°C in the Iron-Carbon binary system [2]. However, addition of various alloying components serve to stabilize austenite at temperatures well below this temperature, and several classes of steel, such as TRIP and Austenitic Stainless Steels depend for their particular mechanical characteristics on metastable austenite at room temperature [2, 50, 51]. The equilibrium phase diagram of the Fe-Ni system, presented in Figure 4, shows the extensive stable phase region for γ Fe.Ni.

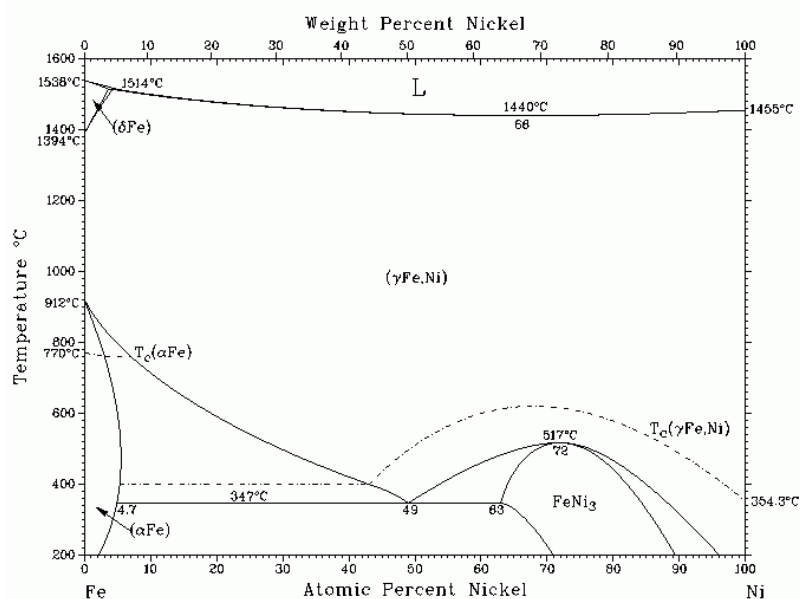


Figure 4: The Fe-Ni phase diagram [3]

2.4.2. Martensite

Martensite is a term used in physical metallurgy for any product of a diffusionless phase transformation. However, in steel, martensite is a distinct microstructural constituent with a specific crystal structure and morphology, formed by a diffusionless transformation from a parent austenite phase. This diffusionless transformation can take place by either cryogenic treatment or application of strain [49]. In this work, martensite is formed as an initial microstructure by cryogenic treatment, but in the next section, Austenite stability, the strain-induced transformation is also considered, which serves to elucidate the austenite behaviour in the interface between the LAZ and the initial microstructure.

Martensite is usually denoted with the symbol α' , which shows its connection to α -Fe, the Body Centred Cubic (BCC) equilibrium phase of Iron below A_1 . The diffusionless nature of the phase transformation is only maintained when the cooling rate is sufficiently high to completely suppress the effect of diffusion, including diffusion of carbon. Therefore, the majority of carbon contained in equilibrium solid solution in austenite should remain in solid solution in the martensitic lattice [52]. The room temperature BCC phase is characterised by a low solubility for carbon, and the BCC interstices available are too small to accommodate a carbon atom. Therefore, the martensitic lattice is distorted into a Body Centred Tetragonal (BCT) structure, with lattice parameters a and c which vary with increasing carbon content [52].

Martensite formation can lead to several distinct morphologies in Fe-Ni-based systems, as shown in

Figure 5 [53]. The different morphologies are linked to alloying content and formation temperature, and exhibit differences in the crystallography of the transformation, denoted in the figure as follows: Greninger-Troiano (G-T), Nishiyama-Wassermann (N-W), and Kurdjumov-Sachs (K-S). These are Orientation Relationships (OR), which describe the relation between crystallographic planes in the parent austenite and the martensite. These orientation relations have been shown to influence transformation kinetics during the $\alpha' \rightarrow \gamma$ transformation [CITATION: SHIRAZI].

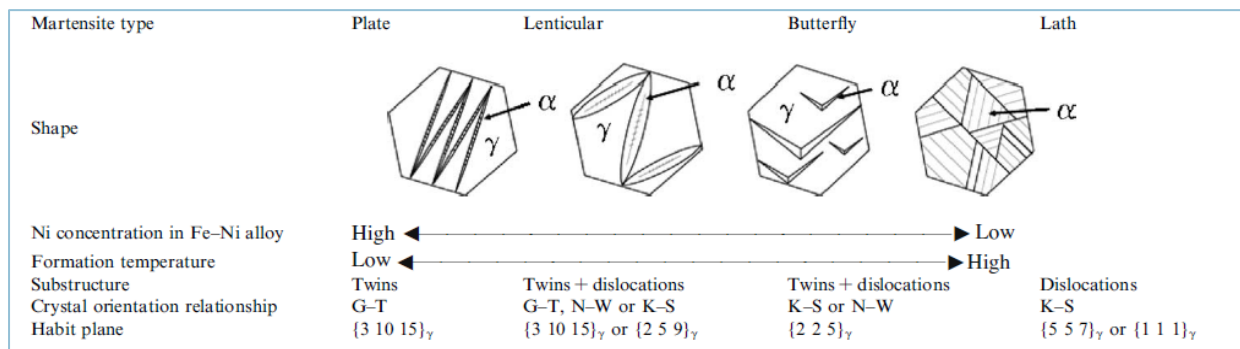


Figure 5: Various martensite morphologies and associated orientation relations in Fe-C-Ni steel [53]

2.4.3. Austenite stability

The austenite present in Fe-C-Ni at room temperature is considered a metastable phase due to its tendency to form martensite when strain is applied [54]. This strain-induced transformation has implications for the mechanical properties of the austenitic steel [55], but also for the laser austenitized zones which are the subject of this thesis, notably upon the formation of the LAZ, at the interface. Therefore, a short overview of austenite stability is

required, and the differences between cryogenically formed and strain-induced martensite in Fe-C-Ni are discussed.

Austenite is liable to transformation to martensite by mechanical deformation, but it can also thermally decompose into more thermodynamically stable phases, notably by precipitation of cementite [55]. The mechanical stability of austenite is described by the T_0 concept, shown in Figure 6. T_0 is a trace of all the temperatures and carbon concentrations for which the free energy of austenite and ferrite are equal.

Therefore, T_0 describes a thermodynamic limit for diffusionless transformation from austenite into a lower temperature phase, since only at these temperatures does the α -iron have a lower

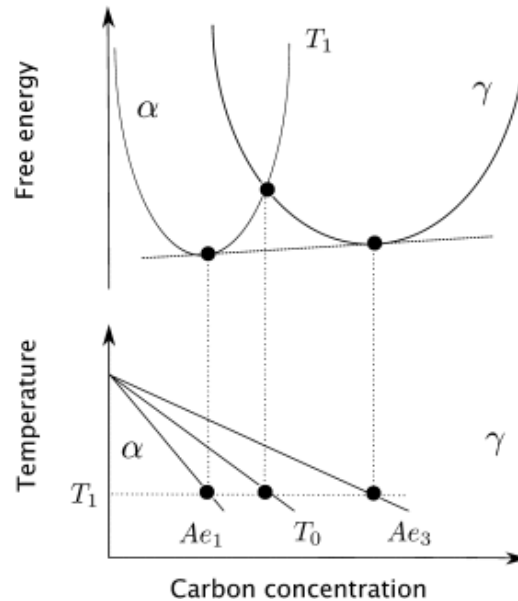


Figure 6: The relation between T_0 and Gibbs Free Energy Curves of α -iron and γ -iron [2]

free energy for the given composition than the austenite. Diffusional transformation can take place, by partitioning of carbon into austenite.

Room temperature austenite in Fe-Ni alloys [56] and Fe-C-Ni systems [54] have been shown to have T_0 temperatures well above room temperature, and therefore, diffusionless transformation can take place. However, although thermodynamic transformation may be possible, insufficient driving force is available for it to occur during cooling to room temperature, hence the metastable nature of the austenite. In the case of martensite formation, this driving force can be applied mechanically, since the martensitic transformation is associated with a shear mechanism, and the application of shear during deformation can accommodate this process [51]. A variety of parameters has been identified which serve to stabilize austenite at room temperature. From the T_0 curve, carbon content can be identified as a prominent contribution, and other austenite-stabilizing elements, like nickel and manganese, also play a significant role [2, 55]. The morphology, orientation, and grain size also have been reported to have a strong influence [55, 57], and recently, the effect of surrounding phases on the austenite stability have become a focus for research [55].

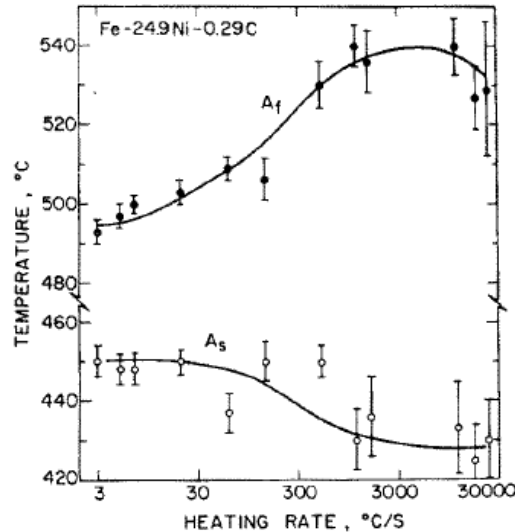


Figure 7: The dependence of A_s and A_f on heating rate for a particular Fe-C-Ni steel [4]

2.5. Fe-C-Ni Steels and the Reverse Transformation

The localised laser heat treatment of cryogenically treated martensitic Fe-C-Ni, the subject of this thesis, results laser-formed austenite zone by a phase transformation that takes place during heating to the reverse transformation start temperature, A_s , and finishes at A_f . These temperatures are comparable to A_{c1} and A_{c3} respectively [27], but in the literature on this subject, A_s and A_f are the more common nomenclature. A_s and A_f depend strongly on heating rate in Fe-C-Ni steels, as shown in Figure 4 for a representative alloy. Literature regarding characteristics of these two microstructural components and the $\alpha' \rightarrow \gamma$ transformation is discussed in this section. Since this transformation takes place upon heating, it is often referred to as the 'reverse transformation', since phase transformations typically considered in heat treatment take place upon cooling.

The reverse transformation of austenite from martensite can take place by two mechanisms: diffusional or displacive [23]. The governing parameters for the transformation to take place by either of the mechanisms are heating rate [4], and carbon concentration [27]. In absence of carbon, Fe-Ni alloys shown reverse displacive transformation over a wide range of heating rates (1-1000 K/s), and at constant austenite start (A_s) and austenite finish (A_f) temperature [27]. In the presence of carbon, the transformation from austenite to martensite is diffusional except in the case of extremely high heating rates (above 1500 K/s) and very low carbon content (0.004 wt-%) [4].

The displacive transformation upon reversion of martensite with high heating rates is characterised by surface relief and high dislocation density, similar to direct martensitic transformation. Although reversion is often used for grain refinement purposes [11], an effect known as structural inheritance, or austenite memory, is also observed. This effect manifests during the $\gamma \rightarrow \alpha' \rightarrow \gamma$ transformation, by restricting the amount of possible orientation variants of the OR to one, the orientation of the initial austenite grain, which restores the previous austenite grain [23, 27]. The mechanism behind the austenite memory effect is not well known, but hypotheses include the dislocation substructure in the martensite [26, 27] or retained austenite acting as a substrate for growth of the reverted austenite grain [24, 27], as well as martensite or interphase boundaries, or a combination of all these factors [27]. However, due to the reversion temperatures A_s and A_f coinciding with the recrystallization temperature, and

the high dislocation density of the reverted austenite providing significant driving force for recrystallization, grain refinement can be achieved if the alloy is held at higher temperature [23, 58].

Table 2: Overview of characteristics of diffusional and displacive phase transformations in Fe-C-Ni

Diffusional	Displacive
Carbon content > 0.004%, or low heating rates (<0.15 K/s)	Carbon content < 0.004%, or extremely high heating rates (> 1500 K/s)
As and Af show pronounced dependence on heating rate due to time-dependent nucleation and growth rate [27]	As and Af independent from heating rate due to fast nucleation and growth
Formation of new grain structure	Potential for reconstruction of grain structure due to structural inheritance
Carbide growth	No carbides during reversion
Limited partitioning	No partitioning
Orientation relations influence kinetics	Orientation relations influence grain reconstruction

In diffusive transformations, observed in Fe-Ni-C and other alloy systems where carbon diffusion controls the reversion mechanism, the heating rate and the peak temperature are the parameters which control the final microstructure [4, 24]. Due to the high mobility of interstitial carbon, tempering is observed even at very high heating rates (60000 K/s in a 0.8% C hardened steel) [26], and carbide precipitation influences the reversion process. Slower heating rates give the carbides more time to grow, which also reduces the carbon concentration of the martensite matrix, leading to higher A_s temperatures [4]. Lower heating rates may also give substitutional alloying elements time to partition during reversion, although long range redistribution is unlikely [4]. In an Mn-Si-C alloy, it has also been established that the austenite morphology depends on the incoherent interfaces. When martensite is reverted, the formed austenite which holds non K-S orientation relations with the surrounding grains will grow faster, and assume a globular, rather than acicular, appearance [24]. At the higher heating rates, the diffusional transformation is limited to the diffusion of carbon [44], and it is suggested that locally, martensite decomposition may be inhibited in micro-volumes, maintaining dislocation substructure, and the associated carbon atmosphere of the dislocations increasing local carbon concentration.

3. Materials & Methodology

This chapter addresses the methodology followed in the experimental work. The experimental work done in this project serves two major purposes. Firstly, to provide information for the model, and secondly, to describe the microstructures created by the laser heat treatment. The model is supported by data from a dilatometry campaign, which provides information on the phase transformation kinetics under conditions of high heating rate, and by thermocouple measurements, during laser heat treatment, which validate the assumptions on the heat conduction relating to the model. The microstructures are described by optical and scanning electron microscopy, and with an EBSD profile of a laser treated specimen. To further assess the effects of the laser surface treatment, the effect of high heating rates on carbon content in the surface was measured using combustion infrared detection, and hardness profiles measurements were taken in the laser heat treated zones.

3.1. Material

The composition of the steel investigated is stated in Table 3. All samples come from the same, hot forged, billet.

Table 3: Alloy Composition

	Fe	Ni	C	Mn	S	P
Wt-%	Bal.	24.9	0.2	2.0	Trace	Trace

The equilibrium phase diagram of the Fe-25Ni system is shown for various carbon contents in Figure 8, and the normalised phase fractions in equilibrium are shown in Figure 9, generated with ThermoCalc [59]. These figures suggest a mixed microstructure at room temperature when formed under equilibrium conditions, containing cementite, the FCC phase (austenite), and the BCC phase (ferrite). An important non-equilibrium parameter, the Martensite start temperature M_s , was calculated using JMatPro 4.0 [60], for a range of carbon contents, as stated in Table 4. This table shows the stabilising influence of carbon on the austenite, and the necessity for cryogenic treatment for the formation of martensitic microstructures. Furthermore, diminishing carbon contents are shown to bring the M_s temperature to ambient temperatures. This shows how (local) decarburisation of the steel, which might take place during high temperature heat treatments, can lead to martensite formation.

Table 4: Martensite start temperature for various carbon contents

	0.2% C	0.15% C	0.1% C	0.05% C	0.025% C	0.0% C
M_s (K)	198	220	242	264	275	286

The material is also characterised by significant microstructural banding, as can be seen in Figure 10. Here, a distinct colour difference caused by the tint etchant, Beraha's 10/3, is visible within an austenitic sample, in alternating bands of a width in the order of 100 micron. Instances of butterfly martensite can be discerned, predominantly in the darker bands, which is mostly likely due to the difference in nickel content. This was substantiated by Electron Dispersive Spectroscopy in the same steel, showing nickel segregation between austenite grains in the order of 1%, where the grains at the lower end of this range, containing some 24% nickel showed substantial amounts of butterfly martensite, whereas the high-nickel grains contained no martensite.

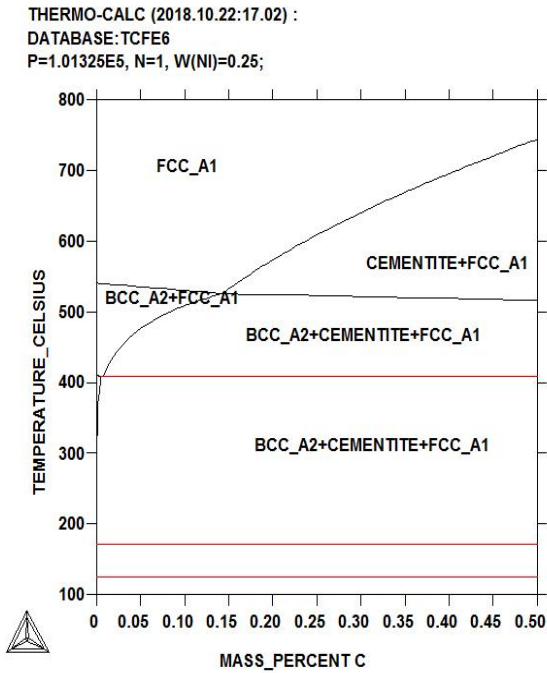


Figure 8: Equilibrium Phase Diagram of Fe-25Ni for a range of carbon contents

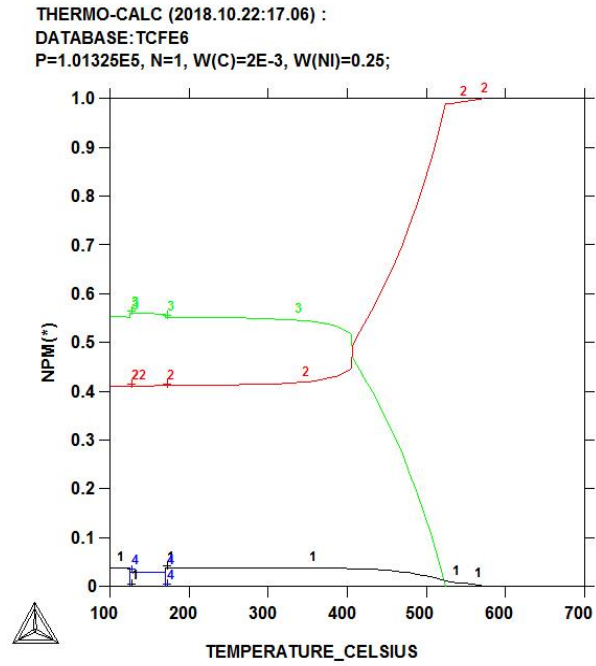


Figure 9: Normalized Phase Fraction in equilibrium. Line 1 and 4 denotes Carbides, while 2 (red) and 3 (green) are respectively the FCC and BCC equilibrium phases.

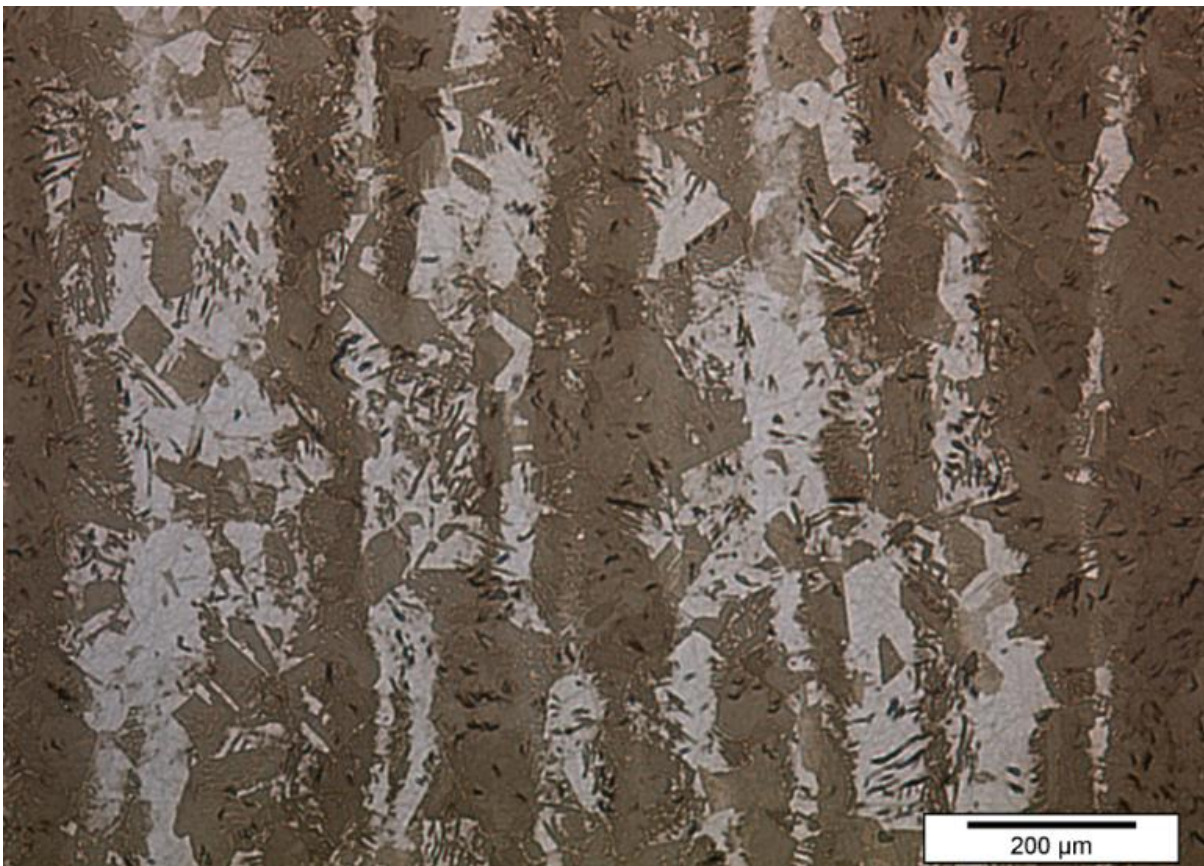


Figure 10: Microstructural Banding revealed with Beraha's 10/3 etchant. Alternating light-etched and darker-etched bands of austenite can be seen, the bands varying in width between 100 and 200 micron. Small, dark grains, like the ones indicated by the circles, are martensite, with distinguishable butterfly morphology.

3.2. Sample Preparation

Samples were prepared for dilatometry and laser heat treatment, according to the following specifications. For dilatometry, cylinders with a length of 10 mm and a diameter of 4 mm were created using Electrical Discharge Machining (EDM). In order to assess the influence of high heating rates, hollow tube samples were also created. With the same outer dimensions, and a wall thickness of 250 micrometres. These samples have a significantly smaller mass than solid samples, facilitating faster heating. Sketches of either sample type are presented in Figure 11.

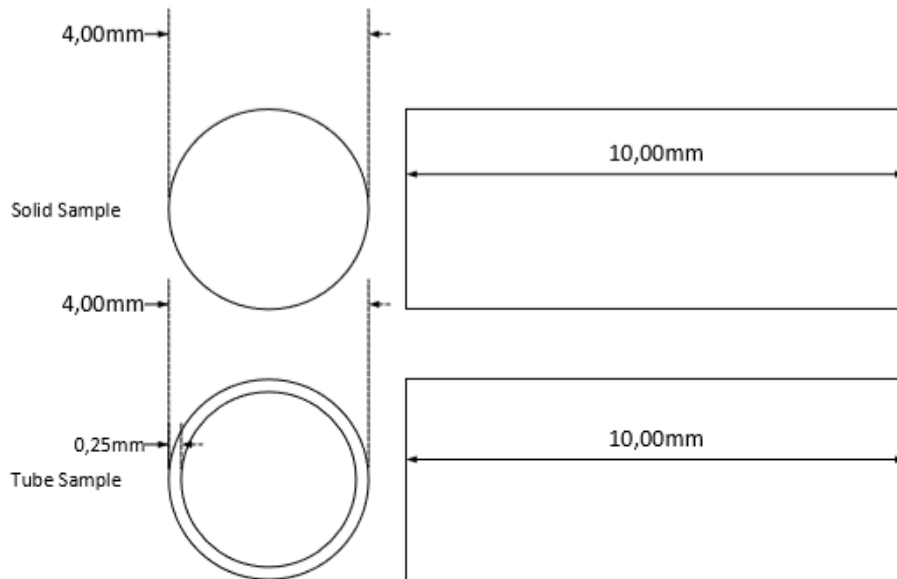


Figure 11: Sample Sketches dilatometry

For the laser heat treatments, bar-shaped samples were created with a length of 60 mm, a width of 15 mm, and a height of 4 mm. These samples were made to facilitate multiple laser seams across the width of the sample, and the placement of multiple thermocouples near the laser seams. A sample sketch is presented in Figure 12.

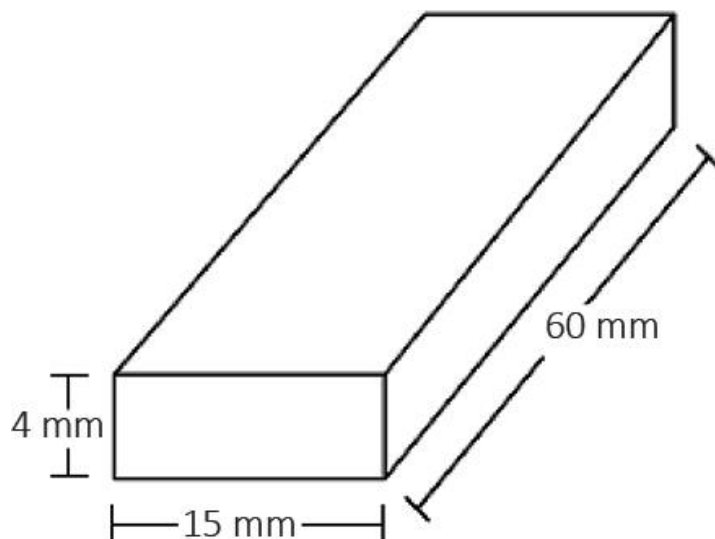


Figure 12: Sample Sketch laser heat treatment

3.3. Initial Heat Treatment

For the localised laser heat treatment, an initial microstructure of cryogenically formed martensite was selected. In order to make this initial microstructure consistent across the various sample types, for comparable initial conditions, the same initial heat treatment was used for the dilatometric samples. This heat treatment involved full austenitization for 5 minutes in an alkali chloride salt bath at 1173 K. Subsequently, the samples were quenched in liquid nitrogen at its boiling temperature, 77 K. Solidified salt adhering to sample surfaces was washed off with water, after which samples were rinsed with isopropanol and dried with hot air.

3.4. Initial microstructures

The austenite, as formed during the salt bath treatment, and subsequently cooled to room temperature, can be seen in Figure 13(a). From this figure, an average austenite grain size could be determined, using a manual tracing method of the grain boundaries. The initial grain size was determined to be 37 microns, with a relative dispersion of 4.15.

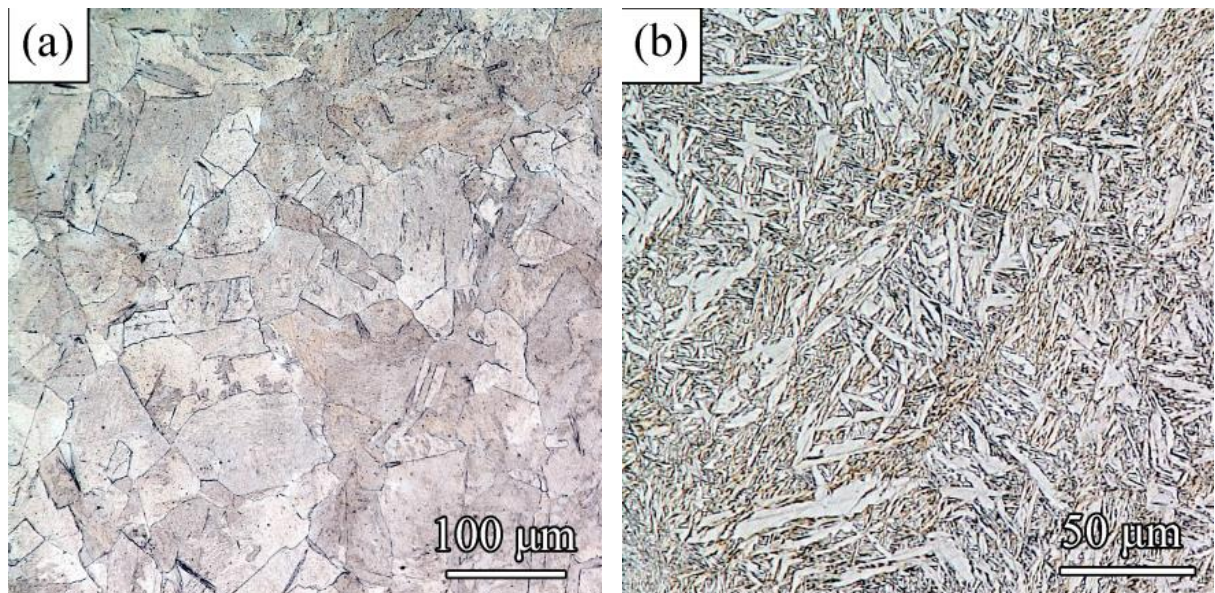


Figure 13: Initial/Bulk Microstructures. (a) Austenite as formed during salt bath, etchant: Kalling's No. 2. (b) Cryogenically formed martensite, etchant: Nital 2%.

The initial microstructure of cryogenically formed martensite is shown in Figure 13 (b). The microstructure shows the characteristic butterfly martensite. Notably, the butterfly wings, which constitute a single twin pair of martensite with a relative misorientation angle of 16° , form massive, white-etched butterflies in the initial microstructure.

3.5. Dilatometry

Dilatometry was carried out using a Bähr Dilatometer 805 A. The dilatometer measures sample dilatation upon heating, using a fused silica push rod connected to a strain gauge. Additionally, a second fused silica rod is present in the machine, so the length changes of the push rod and sample can be compared to this second rod, to obtain the sample dilatation only.

The heating was supplied by an induction coil, and controlled cooling rates were applied on all samples using this coil and quenching gas (helium). The temperature is controlled by attaching a thermocouple to the sample using a resistance spot welder. For optimal temperature control, this thermocouple should be placed near the centre of the sample. Additionally, another thermocouple can be placed nearer to the sample extremities, to obtain extra information. These thermocouples are denoted as T1, centre, and T2, which can be placed further down the major axis of the sample, near the pushrod contact. For the dilatometry, a comparative campaign for various heating rates was designed using heating rates listed in. Hollow samples were tested for all heating rates, to investigate whether this substantial change in geometry had any effect on phase transformation behaviour. Samples were brought to a temperature of 1073 K, using the heating rates specified in Table 5, and subsequently cooled at a controlled heating rate of 20 K/s.

Table 5: Dilatometry Campaign Heating Rates

K/s	5	10	20	50	75	100	200	500	1000
Solid	x	x	x	x	x				
Hollow	x	x	x	x	x	x	x	x	x

A typical dilatometry signal is presented in Figure 14, where a heating cycle was started at room temperature, and the thermal expansion causes a length change over the course of heating, with a discontinuity in the linear expansion seen just above 400 °C. Here, the material no longer expands by its linear coefficient of expansion, due to a phase transformation. This phase transformation constitutes a reordering of the atomic lattice, which corresponds to a change in density. This density change causes a contraction or dilatation of the sample, which is measured by the push rod as a change in sample length. In the case of Figure 14, a contraction takes place, denoting an increase in sample density. The onset of phase transformation can be designated to be the moment where the signal slope is no longer linear

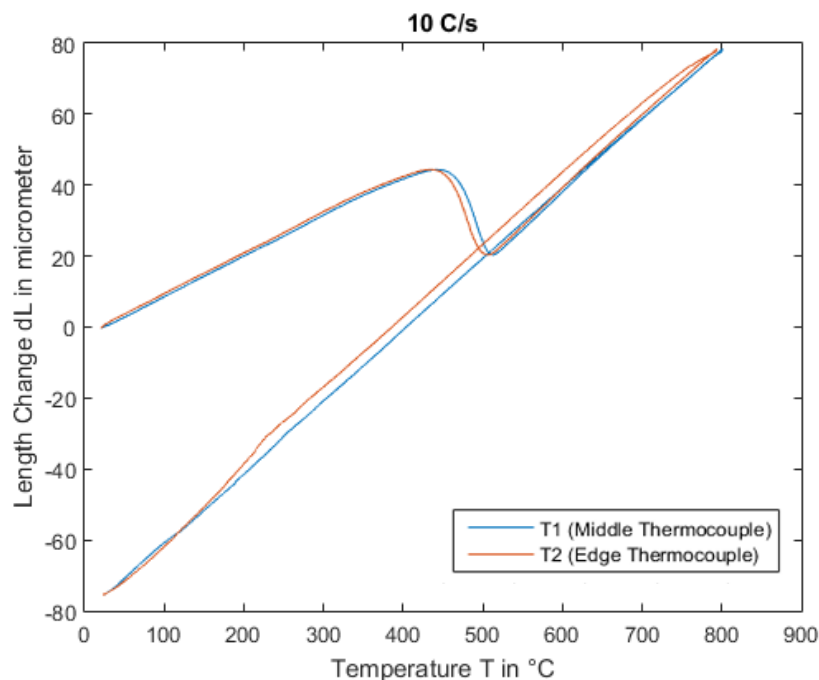


Figure 14: a typical dilatometry signal. Blue is the control thermocouple and orange the additional thermocouple measurement

an constant, and the end of phase transformation is, by analogy, the moment were the signal is monotonously increasing with a constant slope, denoting the linear expansion coefficient of the new phase [61].

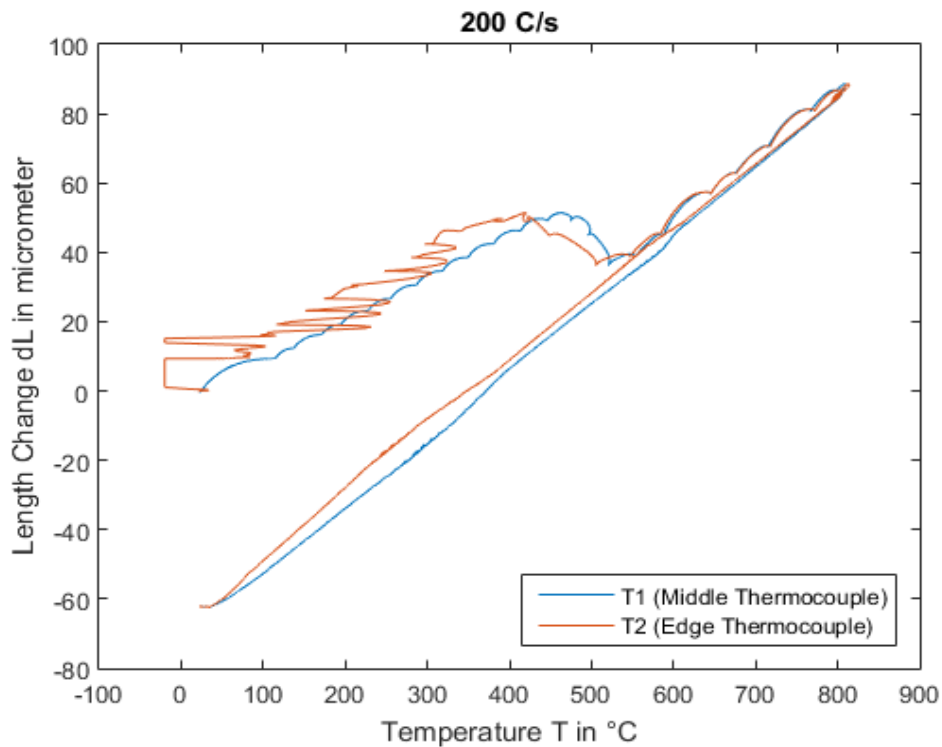


Figure 15: A typical high heating rate dilatometry signal.

The dilatometry measurements contain well-behaved signals from the measurements carried out at conventional heating rates. Phase transformation onset and finish, which is the desired result for this dilatometric measurements, can easily be extracted from these signals, either manually by graphical methods, or by a mathematical approach relying on the onset of non-linear behaviour. This second approach was chosen, mainly due to the necessity for post-processing of the unstable signals of high heating rate dilatometry. A typical high heating rate signal is presented in Figure 15. Pronounced oscillations in the temperature are visible, especially in the secondary thermocouple, due to the low thermal inertia of the system. Although adjustments in PID control of the system were made, this effect could not be mitigated completely by apparatus control alone, and therefore, a prescriptive shape-language model [62] based on piecewise regression splines [63] was used to obtain reasonable representations of the data. This method was carried out using Matlab [64], and a shape language modelling (SLM) tool created for this software [62].

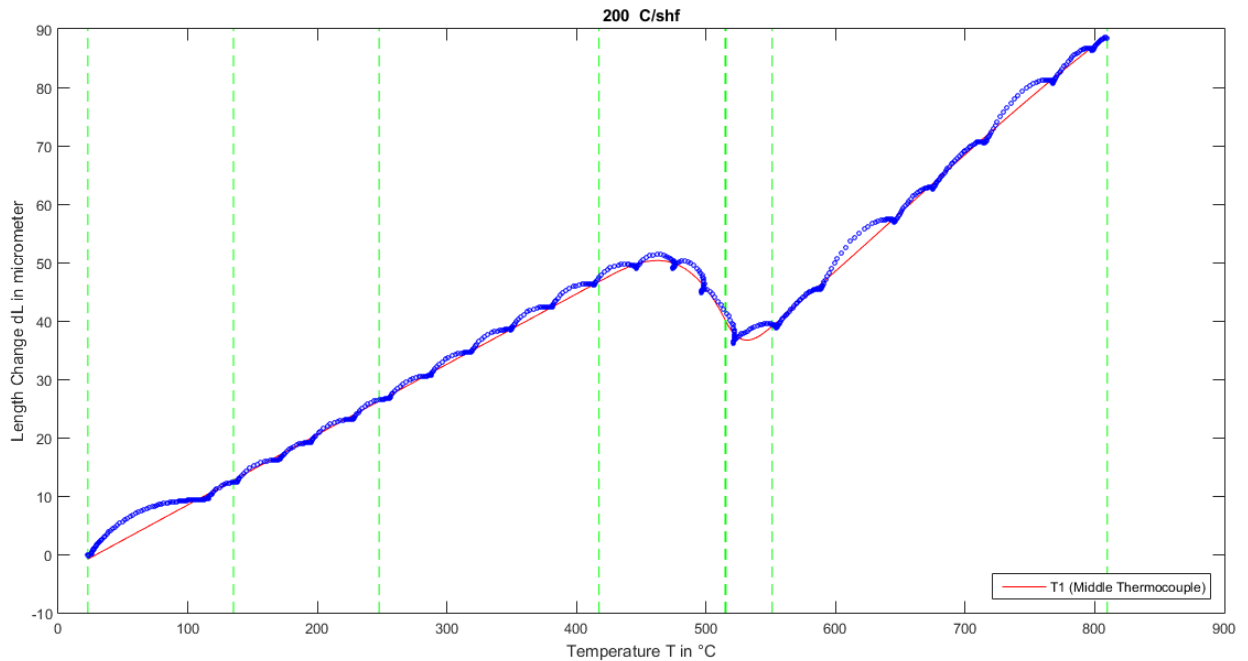


Figure 16: The 200 K/s example of the post-processing of dilatometry data. Blue dots denote measured temperatures and length changes, the green dashed lines the knots for the SLM fit, and the red line the resulting function fit for the dL-T signal

The need for post-processing, shown in Figure 15, and its results, shown in Figure 16. Here, a heating curve is shown from a 200 K/s sample, where the blue dots denote the measured signal, i.e. the data points described by temperature and length change pairs. From this plot, a graphical determination of the phase transformation temperature would not be accurate within an acceptable margin of error, in this example especially clear for the A_f , due to strong oscillations caused by the low thermal inertia of the hollow sample. The red line is a piecewise regression spline fit created using the SLM model. The shape language model allows for prescriptive behaviour, where within two ‘knots’ (dashed green lines), a certain model behaviour, e.g. linear, can be proscribed. The result of the SLM model is a smooth, continuously differentiable line amenable to the calculation of A_s and A_f .

3.6. Laser Heat Treatment

Sample preparation for laser heat treatment was carried out in two steps. The first step, initial heat treatment using a salt bath and liquid nitrogen quenching, was carried out according to the description given in section 3.3. Subsequently, the sample surface condition was brought up to a consistent quality, using a Struers hand-grinding machine and P80 grid grinding paper. This rough surface finish was required mostly to mitigate the risk of specular reflection of laser radiation, which can damage the equipment and is generally hazardous to the operation. In Figure 17, a schematic of the laser heat treatment set-up is presented.

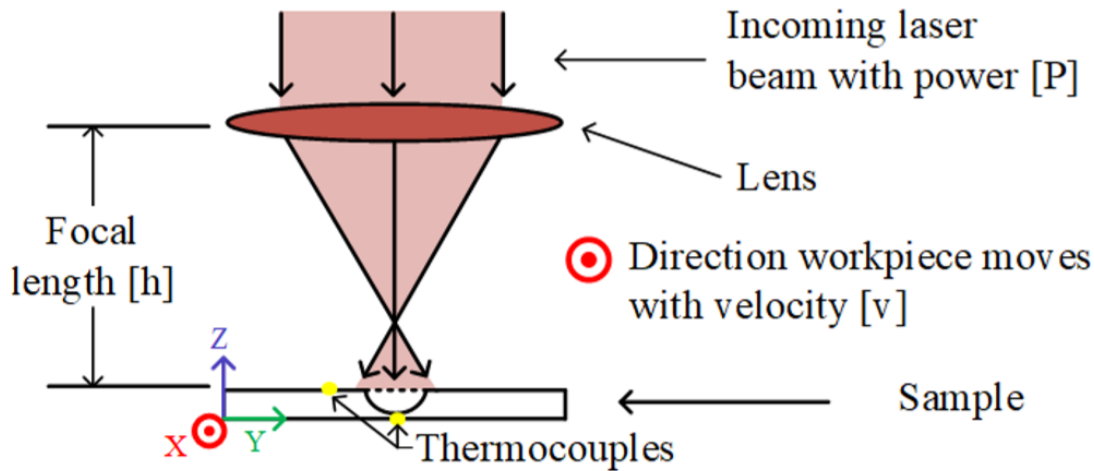


Figure 17: Laser Heat Treatment scheme, figure adapted from [1]. A specimen is shown in side-view, and the process parameters are schematically represented: laser power $[P]$, laser velocity $[v]$, and focal length $[h]$, the laser setting representing spot size.

Laser heat treatment data was gathered from two sources. The first was processing of samples created using a Trumpf HL3006D Nd:YAG laser, using a continuous wave pulse at a wavelength of 1064 nanometre. These first samples were created by following a factorial design campaign, and data from the runs with parameters resulting in feasible LAZ's was gathered to be compared to the model. This comparison was based on the depth and width of the LAZ's, and the laser settings for these experiments are summarized in Table 6. The samples used in these experiments were of the dimensions described in Figure 12, and the width and depth of the LAZ formed by these heat treatments were used for validation of the model. The parameter h denotes the distance between the laser surface and the work piece, and relates to the laser spot size, since the optical parameters of the laser are not adjusted. For modelling purposes, this focal distance was estimated to correspond to a spot size of 0.8 mm at $h = 180$ mm.

Table 6: Parameters from successful laser treatment from factorial design

	P (W)	v (mm/s)	h (mm)
5	400	25	180
6	400	20	180
7	200	5	180
8	200	2.5	180

Using the extent of the laser austinitized zone (LAZ) for the validation of a laser heat model, for which these samples were used is insufficient, when aspects such as the heating rate are required as a validated model output [46]. One of the main criteria for the use of the model posited in this work, is that it yield a decent estimate for the heating rate, due to its importance to the martensite to austenite transformations in this steel. The deficiencies of a model which is only validated by comparing predicted microstructural change to observed microstructural change stems from two main discrepancies between model behaviour and physical behaviour:

1. The microstructural changes, measurable as the width and depth of the LAZ in the case of this work, and as case depth of surface hardening in most other works, are subject to other effects which are explicitly not modelled, such as strain-induced transformation.
2. The modelled LAZ size or case depth are usually predicted based on the isotherm of A_f , i.e. peak temperature alone is taken as the parameter controlling this microstructural change. This may lead to validated case depth models, but no validation is given at all for heating rate.

The second aspect is illustrated by Orazi et al. [46], who present a validated hardening case depth model, with heating rates in the orders of 10^5 K/s, which they assume to be a distinct overestimation. Therefore, thermal measurements were required for further model validation. These measurements took place at TATA Steel's Product Application Centre, due to equipment availability issues with the Trumpf HL3006D and its successor at the TU Delft. These laser heat treatments were carried out using a 4.5kW Trumpf HLD 4506 Nd:YAG laser. This constituted a shift to a significantly more powerful set-up, with a higher threshold for stable operation power. This was accounted for by operating the system at similar speeds, but significantly larger laser spot sizes, in order to keep power intensity in a similar range. Thermocouple measurements were taken in a grid pattern using 4 alomega-chromega thermocouple wires were attached using a resistance spot welder, and measurements were logged using a DL750 Yokogawa 4-channel datalogger.

Table 7: Power and laser velocity per sample

	P (W)	v (mm/s)
Sample 1.1	1500	41.67
Sample 1.2	1500	33.33
Sample 1.3	1000	25
Sample 1.4	1000	16.66
Sample 2.1 & 2.2	1500	33.33
Sample 3.1	1000	33.33
Sample 3.2 & 3.3	1250	33.33
Sample 3.4,3.5,3.6	1000	16.66
Sample 4.1, 4.2, 4.3	1750	33.33

Thermocouple placement was carried out using a table top resistance spot welder, and was carried out in a square grid pattern near the sample centre (. Initially, several combinations of settings were attempted to assess whether melting limits would be reached, and what could be assessed from visual inspection of the work piece in terms of material and laser behaviour. Subsequently, when some satisfactory initial results were obtained, three laser lines using identical parameters were measured, one to either side of the thermocouple grid, and one on the bottom of the sample, to obtain thermal data at various positions relative to the laser lines. Subsequently, distances between laser line centre and thermocouple position were measured and logged.

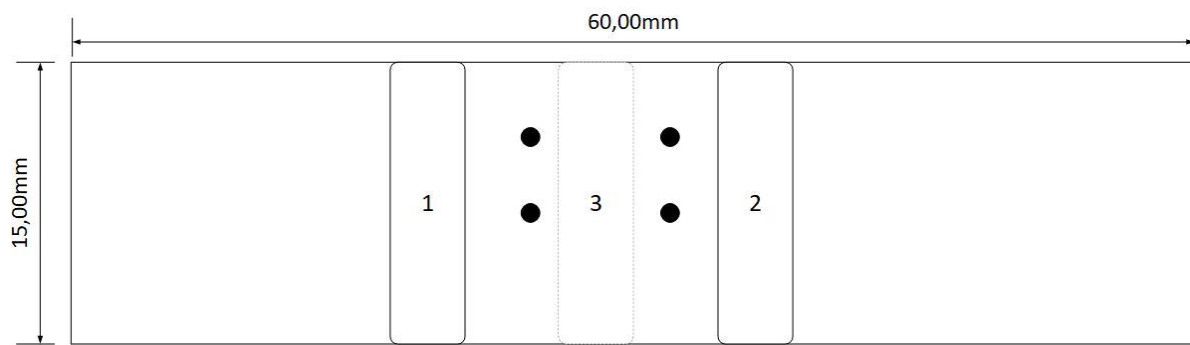


Figure 18: Sample thermocouple placement during laser heat treatments. The black dots denote four thermocouples, and the numbered lines approximate positions of laser treated regions.

3.7. Light Optical Microscopy

Light Optical Microscopy was performed using a Leica DMLM optical microscope and a Keyence VHX-100 Digital microscope. The microscope are versatile tools for the characterisation of morphological features on the micrometre scale, such as the LAZ. In order to reveal microstructural features, the samples were grounded to a P2000 finish on a Struers rotary grinder, and polished to a 1 micron finish on a Struers Labopol polishing machine.

The information obtained in metallography relies on the choice of etchant, since microstructural components, such as phases or grain boundaries, responds differently to the chemical reagents in the etchant [65]. For this work, several etchants were used, to obtain a reasonably complete optical characterisation.

Table 8: Etchants

Name	Composition	Reveals (in this alloy)	Notes
Nital 2%	2 g HNO ₃ 100 mL ethanol	Martensite	
Kalling's No. 2 (Waterless)	5g CuCl ₂ 100 mL HCl 100 mL ethanol	Martensite Austenite grain boundaries (partially)	Dilution with 2 parts alcohol prevents over-etching in sensitive samples.
Beraha's 10/3	10 g sodium metabisulfite 3 g potassium metabisulfite 100 mL distilled water	Martensite Chemical inhomogeneity of austenite grains. Banding. Prior Austenite Grain Boundaries (PAGB).	
Nital 2% + Sodium Metabisulfite	Nital 2% pre-etch 20 g sodium metabisulfite 100 mL distilled water	Martensite Banding PAGB	Some further information using crossed polarizers and sensitive tint.
Beraha's Sulfamic Reagent	2 g sulfamic acid 3 g potassium metabisulfite 100 ml distilled water	Austenite grains/orientations. Austenite twinning.	Crossed polarizers. Optimal colour contrast at 89° analyser angle.

3.7.1. Grain Boundary Etching

Grain morphology and size are important microstructural characteristics and can be described well if proper grain boundary etching is achieved. For the martensitic structure, Nital 2% was selected, based on its versatility [65]. Austenite grain boundaries were etched using a dilute (1 part stock solution, 2 parts ethanol) Kalling's No.2 solution.

Images obtained by reasonably complete grain boundary etching can be used for a determination of grain sizes of phases in steel, as described by Lehto et al [66], using a combination of manual boundary tracing, image contrast enhancement, and the publicly available tool described in their publication. This tool uses the guidelines set out in ASTM E1382 for the linear intercept method.

3.7.2. Tint Etching

In addition to grain boundary etching, tint etching was used. Full revelation of the grain structure is reportedly achievable with this method [67], and a variety of colour etchants were tested. Colour etching relies on the deposition of a surface layer on the sample. The composition of this layer depends on the substrate and the used reagent, but it is the sample. The composition of this layer depends on the substrate and the used reagent, but it is commonly a sulphide layer [67]. This interference layer grows as a function of crystallographic parameters, including grain phase, grain orientation, and grain chemical composition. Phase discrimination and full revelation of grain structure, obtained from the differences in colour caused by grain orientation, are desirable. However, as reported in section 3.1, chemical heterogeneities are present, and tend to dominate the desired effect of discriminating austenite grains fully by the orientation effect. This effect can be seen clearly in Figure 19. Two distinct etching behaviours can be discerned in this image, which results in different Austenite (A) and Martensite (M) characteristics. One austenite phase, labelled A_1 , is the white etched phase, with pronounced, multi-directional scratches. Practically no difference is observed between the different grains of austenite displaying these etching characteristics. The massive, brownish-beige etched features are labelled A_2 . In both phases, butterfly martensite colonies can be observed (M_1 and M_2), but sharp delineation is observed in M_2 only.

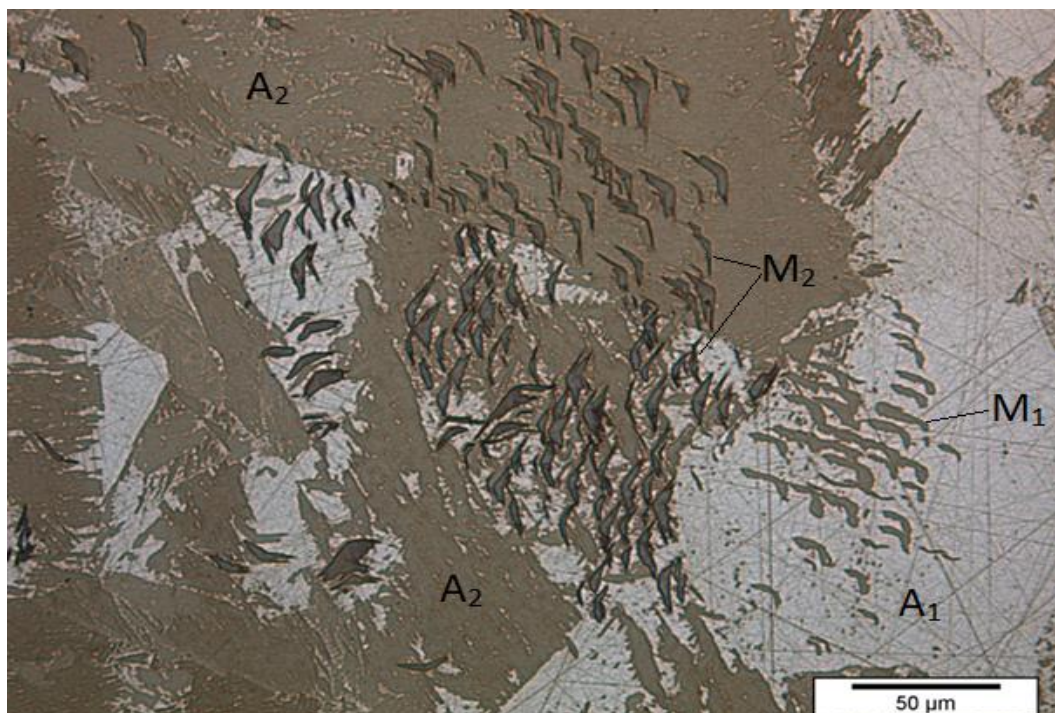


Figure 19: Beraha 10/3 Colour Etch of an austenitic microstructure with butterfly martensite colonies.

3.8. Scanning Electron Microscopy and Electron Backscatter Diffraction

For higher magnifications than possible with optical microscopy, scanning electron microscopy was performed with a JEOL JSM 6500F. Specimen preparation for micrographs was carried out using the same scheme as for optical microscopy, and the use of Nital 2% as the etchant for the martensitic microstructure in the interface.

For the EBSD measurements, minimal surface distortion is a stringent requirement. Therefore, after following the same grinding and polishing procedure as the optical samples, the EBSD sample was further polished using Struers OP-S colloidal silica liquid, for a total of 15 minutes, with gentle rotation on a Struers Labopol machine. The specimens selected for EBSD from the low-power laser treated samples showed very light etching of austenite after this procedure, which resulted in an overall indexing during EBSD of about 60%, due to the surface relief caused by this etching. EBSD was also attempted for the high-power laser treated specimens, but the same etching effect was already dominantly present at very short polishing times, rendering these samples inadequate for EBSD.

3.9. Combustion Infrared Detection

Carbon content of selected dilatometry samples was measured using a LECO 744 Series Carbon and Sulfur Combustion Infrared Detection apparatus. This apparatus rapidly melts inorganic samples, and combusts the carbon and sulphur contained in these samples. The gasses produced during this combustion are purified and infrared absorption spectroscopy is used to obtain a quantitative measure of the carbon and sulphur content of the combusted sample. The quantitative quality of this measurement relies on accurate weighing of the samples, calibration using carefully controlled reference samples, and complete combustion, which can be visually ascertained based on the residue in the crucible.

For these measurements, due to weight limits for detection and operation of the machine, whole dilatometry samples were used. The weight limit was such, that three hollow samples had to be combined into an aggregate sample representing the average decarburisation of these specimens.

3.10. Hardness Measurements

An EMCO G5 DuraScan apparatus was used to obtain hardness profile to characterise differences in hardness within the LAZ, and between the LAZ and parent material. To this end, a diamond indentation was made with a 0.2 kilograms of force, and measured on the Vickers Hardness scale HV0.2. Hardness profiles along depth lines with a spacing of 75 micron were made across the depth and along the surface of the LAZ, to see the effects on the hardness in the LAZ and its interface, near the surface and in the depth of the sample.

4. Thermal Model

This work includes the design of a thermal model to describe the response of a work piece to laser heat treatment and subsequent self-cooling, in terms of a 3D temperature field which changes over time. Thereby, local information relevant to the thermodynamic and kinetic conditions during heat treatment can be obtained.

The thermal modelling of the laser surface treatment was carried out in a commercial software package, COMSOL Multiphysics® version 5.3a [29]. This software facilitates the creation of 3D geometrical work pieces, and the implementation of several physical and equation-based models. These models and their coupling effects are solved by the numerical Finite Element Method (FEM), in order to obtain, in the case of this work, a transient thermal model.

4.1. Finite Element Methods for Time-Dependent Heat Modelling in COMSOL Multiphysics

As discussed in Chapter 2, analytical models exist for phenomena related to metal-heat source interactions based on the Heat Equation. These are formulated for specific cases, notably for welding, based on Rosenthal's approach [19, 32, 38], and subject to restrictive assumptions, including (quasi-)steady state, infinite work piece dimensions, and simple sample geometries. Therefore, analytical models are of limited use [19]. This has been the main cause for the implementation of numerical models for the simulation of heat transport in metal surface treatments [19], notably by the Finite Element Method, but also by the Finite Difference Method (FDM) and the Finite Volume Method (FVM) [32]. Finite Element methods have several advantages, especially when considering multi-physics analysis [68]. Therefore, a short overview of the Finite Element Method is given here, illustrated in terms of its handling of the Heat Equation.

A solution to the heat equation can be found using the Finite Element Method as follows. Firstly, the geometry of the system is considered, and subdivided by a process called 'meshing'. Meshing is a discretization procedure, creating discrete points called nodes. These nodes, when connected, form the elements that the method is named for [69]. This discretization is used to obtain simpler equations which locally, at the nodes, approximate the Partial Differential Equation (PDE) which formally describes the original problem.

When modelling transient behaviour, as is done in time-dependent heat models, the Heat Equation is approximated with a set of local Ordinary Differential Equations (ODE) at each of these nodes. This step reduces the number of partial derivatives of independent variables from the four found in the Heat Equation, to one, time. This substitution relies on the Galerkin Method, where the heat conduction equation is formulated by multiplying by trial functions and integrating it over the entire domain. This leads to the following formulation, equation 6:

$$\int_{\Omega} \rho c_p \frac{\partial T}{\partial t} \phi dV - \int_{\Omega} k \nabla T(x, y, z) * \nabla \phi dV = \int_{\Omega} q \phi dV \quad (6)$$

Where Ω denotes the domain over which to integrate, dV the domain volume variable, and ϕ a test function. The terms appearing in the elementary heat equation can be recognised. The test function is a mathematical construct assumed to belong to the same Hilbert Space. Although its precise definition is beyond the scope of this treatment, the Hilbert space has certain valuable properties. It is analogous to a vector space in that it allows for the measurement of lengths and angles, such that functions can be treated as vectors within a

vector space, including linear combinations. Assuming that the solution T belongs to the same finite-dimensional Hilbert sub-space as the test function is referred to as the Galerkin Method, which is routinely used in the Finite Element Method when solving Partial Differential Equations. This assumption states that an approximate solution T_h is given by a linear combination of basis functions of this subspace, as stated in equation 7:

$$T_h(x, y, z) = \sum_i a_i \psi_i(x, y, z) \quad (7)$$

Where a_i denotes an unknown set of coefficients which provides weighing coefficients to the basis functions ψ_i . This practice is the discretisation of the mathematical model, and leads to a solvable system of equations consisting of the stiffness matrix A , the solution vector in each model node T_h , and the source function vector b . This system of equations is given, in matrix notation, in equation 8

$$AT_h = b \quad (8)$$

The stiffness matrix contains all coefficients T_i given by equation 9 for the time dependent Heat Equation:

$$\rho C_p \frac{\partial T}{\partial t} \sum_i \int_{\Omega} \psi_i \psi_j dV + \sum_i T_i \int_{\Omega} k \nabla \psi_i \cdot \nabla \psi_j dV = \int_{\Omega} q (\sum_i T_i \psi_i) \psi_j dV \quad (9)$$

The resulting ODE can then be solved by a straightforward numerical integration using backwards differentiation formula's, where the T_i coefficients are solved for. This requires a separate numerical approximation to solve for the last remaining differential, of temperature with respect to time. This is done by a finite difference method based on the backward Euler method, that can be stated as the following finite difference:

$$\frac{\partial T_i}{\partial t} \approx \frac{T_{i,t+\Delta t} - T_{i,t}}{\Delta t} \quad (10)$$

The substitution of this term in the formula above requires the substitution of T_i with $T_{i,t+\Delta t}$. This substitution requires a system of equations to be solved at each time step. Since $T_{i,t+\Delta t}$, the unknown that the system is solved for, is present in all terms of the equation which makes up the stiffness matrix, this is known as an implicit method, and in the first-order approximation, it is equal to the backward Euler method [29, 69-71].

The use of the backward differentiation functions, of which the backward Euler method is the first-order form, leads to unconditionally stable solutions, i.e. small perturbations in the solution lead to small deviations in the result [72]. However, COMSOL Multiphysics® employs an additional adaptive time stepping algorithm in time dependent FEM which is summarized in Figure 20, resulting in the enforcement of an absolute tolerance criterion for the simulation error [73]. This algorithm compares solutions (model state U) obtained from a tentative time step h_i and a smaller time step h_{i+1} . If the difference between the model states is within a certain tolerance, the solution for that point in model time $t + h_i$ is accepted. This algorithm prevents pitfalls usually associated with time dependent modelling with fixed time steps, such as overdamping or underdamping [74].

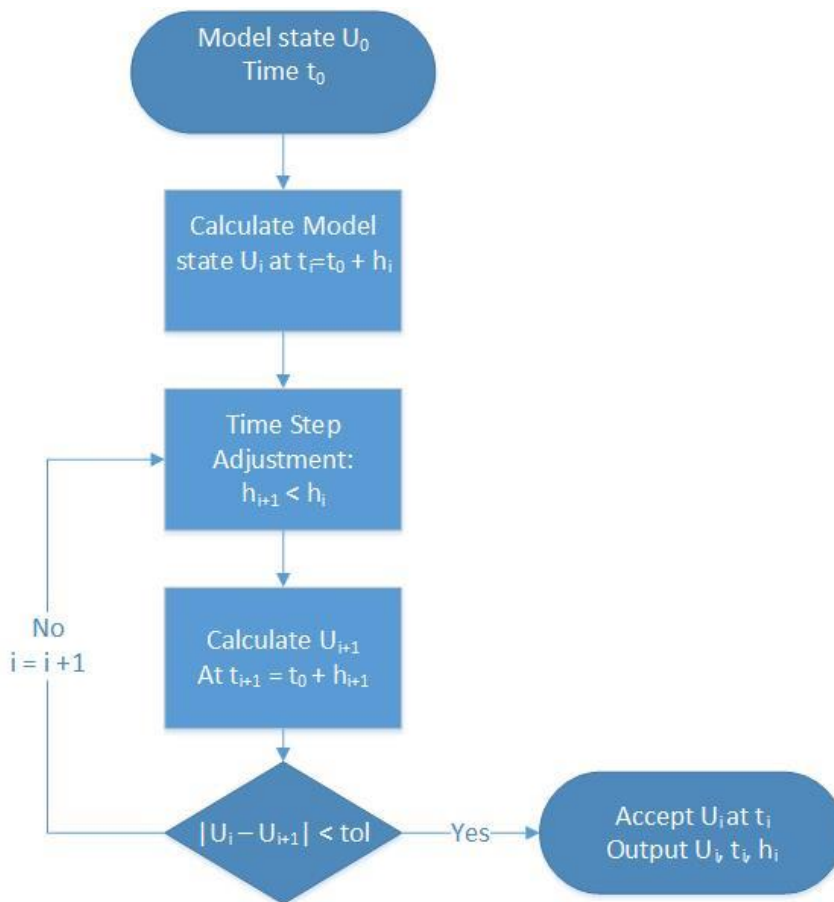


Figure 20: Adaptive Time Stepping Algorithm

4.2. Model Set-up

The process parameters and physical phenomena related to laser surface treatment must be considered for a fully descriptive thermal model. Isolating process parameters from the rest of the physical behaviour of the model facilitates the use of the model as a predictive tool for related surface treatments. Boundary conditions describing the interaction of the modelled domain and its surroundings must also be properly modelled, to describe the ways in which heat enters and leaves the model domain. Lastly, in time dependent thermal modelling, material parameters are not necessarily constant in time, but rather, depend on the thermal history which is being modelled. These coupling effects, referred to in section 2.3.2, need to be accounted for in the model, and their behaviour is described in the section Transient Properties.

4.3. Process Parameters

The effect of the process parameters on the general behaviour of laser surface treatment in terms of case depth and peak temperature, has been discussed in section 2.3.1. Three process parameters were chosen for the model, corresponding to machine settings commonly found in laser surface treatment: laser velocity, laser power, and laser spot size.

- Laser velocity denotes the relative movement of the laser and the work piece in meters per second. This parameter controls which part of the work piece undergoes laser surface treatment, and describes either laser movement on one or more free axes, work piece movement, or a combination of both [22]. Furthermore, the velocity

contributes strongly to the dimensionless travel rate, as defined in section 2.3.1, which is, in analytical treatment of laser surface treatment, taken to be the determining factor for the case depth.

- Laser power is the energy per unit time generated by the laser apparatus. Given that the energy carriers are photons of a single wavelength and have the velocity of light in the medium in which they are propagating, the energy of a single photon is given by the elementary Planck-Einstein Relation, equation 11:

$$E = h \cdot f \quad (11)$$

Where h is Planck's constant and f the frequency of the emitted radiation. This results, for a laser of fixed wavelength, in a constant energy per photon, and the laser power is then determined by the amount of generated photons per unit time. Laser power is one of the two governing factors for the peak temperatures experienced in laser treatment, and hence, of critical importance to limit within certain bounds, in order to prevent melting [45].

- Laser spot size relates to the area of the work piece which is irradiated by the laser beam. This measure, usually given as spot radius r_{spot} . This parameter contributes to the peak temperature, and relates to it via the beam power density, Φ [W/m²], the heat input per unit area. The beam power density can be treated in various ways, and the respective contributions of laser power and laser spot size relates to the so-called Beam Power Density, via the distribution function used.

4.3.1. Beam Power Density and Distribution

The laser power and laser spot size parameter control the heat flux of the laser into the model. In laser surface treatment modelling, the heat flux that represents the laser beam also requires the description of the distribution of the energy over the surface, or in the case of deeper penetration of laser heat, as a volume distribution [48]. For solid state laser heat treatment, surface heat sources are generally used, due to the limited depth of Fresnel Absorption [32]. Surface heat sources come in two main forms, discussed in this section: the Top Hat profile and the Gaussian Beam Profile.

In a simple treatment of the heat flux, known as the Top Hat profile, the power density (in units of $\frac{W}{m^2}$) is given by the equation 12:

$$\Phi\left(\frac{W}{m^2}\right) = \frac{P}{\pi r_{\text{spot}}^2} \begin{cases} \text{if } r < r_s \\ \text{if } r > r_s, \Phi = 0 \end{cases} \quad (12)$$

Where P is the laser power in Watt, and r_{spot} the spot size in meter. This power density is constant within the spot, and zero elsewhere, as shown in Figure 21. This straightforward treatment is easily adjusted to other spot geometries using apertures of arbitrary dimensions, since it assumes the average power density is equal to the power density throughout the spot.

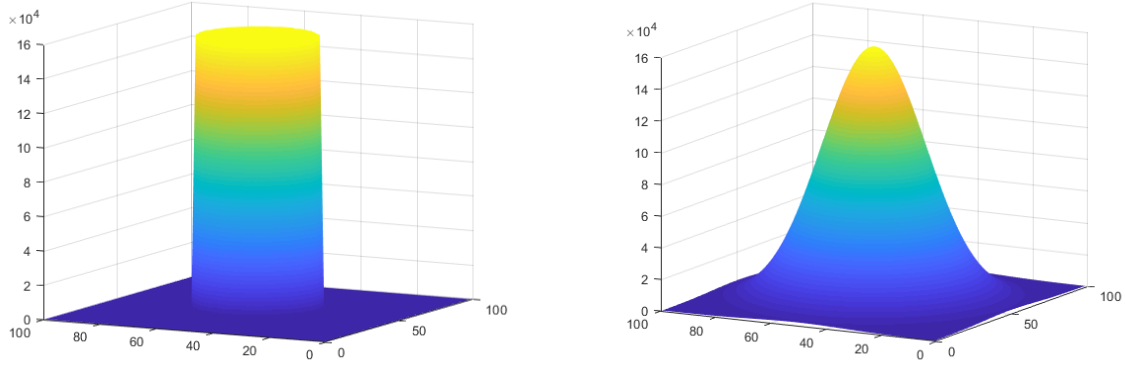


Figure 21: Power Density Profiles modelled using $P = 400 \text{ W}$ and $R_{spot} = 40 \text{ mm}$. Left: Top Hat Profile, Right: Gaussian Profile

Although this is a straightforward treatment, physical characteristics of the laser beam are modelled more adequately using Gaussian distributions [48], the simplest of which can be described with the equation 13:

$$\Phi \left(\left[\frac{W}{m^2} \right] \right) = \frac{8P}{4\pi r_{spot}^2} \exp \left(- \left(\frac{\sqrt{2}}{r_{spot}} \right)^2 (x^2 + y^2) \right) \quad (13)$$

This intensity distribution contains spatial coordinates x and y , with denote the distance from the beam centre. The presence of these coordinates in the negative exponent results in a gradual decay of the intensity when the distance increases. This is more representative for the laser heat sources used in this work, and is therefore selected as the appropriate beam power distribution.

4.3.2. Heat fluxes in Laser Surface Treatment

The heat flux (q) in the heat equation for laser heat treatment modelling denotes an aggregate term for all the heat fluxes in and out of the work piece at all boundaries, and contains various terms, including the laser heat flux, radiative heat loss to the environment and external convection. In the numerical model, these fluxes are defined for specific boundaries, using the appropriate equations.

Table 9: Heat fluxes modelled in the thermal model of the laser heat treatment

Heat Flux	Equation
Laser Heat Flux q_L , equivalent to beam power distribution Φ	$q_L \left(\left[\frac{W}{m^2} \right] \right) = \frac{A * 8P}{4\pi r_{spot}^2} \exp \left(- \left(\frac{\sqrt{2}}{r_{spot}} \right)^2 (x^2 + y^2) \right)$
Radiative Heat Flux	$q_r = \varepsilon \sigma (T_{ambient}^4 - T^4)$
Natural Convection	$q_c = h(T_{external} - T)$ $h = \frac{k}{l} 0.15 Ra_L^{1/3}$
Thermal Contact	$-n_d \cdot q_d = -h(T_u - T_d) + rQ_b$ $h = h_g + h_c$

The heat fluxes presented in Table 9 are explained below:

- Laser heat flux: The interaction of the laser radiation with the metallic surface is modulated by this parameter, known as absorptivity (A). This property can be expressed simply as the ratio of absorbed power P_A over laser power P_L :

$$A = \frac{P_A}{P_L} \quad (14)$$

The absorbed power is not easily measured, nor is there agreement on the validity of theoretical models for the calculation of absorptivity [75]. Several factors contribute to absorptivity, including local temperature, the surface finish of metal considered, and alloying elements, and it can vary as much as 30% [31]. Telrandhe et al. [22] use a model for the absorptivity which is linearly dependent on the laser velocity, reflecting the interaction of the absorptivity with the local temperature. They state that this is related to the relatively high temperature build-up in the laser-irradiated area of their work piece, due to the low thermal conductivity of the titanium alloy they consider. In steel, the surface conditions and microstructure tend to dominate over this effect to the extent that it can be modelled as a constant if the surface is reasonably homogeneous [31].

- Radiative heat flux: in this expression, the black body emissivity of the material, ϵ , and the Stefan-Boltzmann constant σ , appear. This heat flux describes the net blackbody radiation from the work piece to the environment [76].
- Natural convection and thermal contact are both based on Newton's Law of Cooling [35], and depend on the temperature difference between the work piece and environment, and the heat transfer coefficient, h . For the convection case, this is based on the Raleigh number, Ra_L , which describes the ratio between conductive and convective forces in the fluid in contact with the work piece. The other heat transfer coefficient, which relates to the thermal contact heat flux, is made up from a contribution h_c representing the direct contact between the work piece and the resting block, and h_g representing the gaps caused by the surface roughness of the resting block and the work piece.

In Figure 22, a schematic of the heat fluxes in the laser heat treatment is shown. This figure shows the bisection of a work piece and a laser heat flux, q_L , irradiating this work piece, while moving with a velocity v_L . This movement causes an asymmetric temperature field, shown in the specimen cross-section. The isotherms are closely spaced in the front of the laser spot. This is due to the heat conduction in the sample being slower than the laser movement, while the laser almost instantaneously heats the surface it irradiates. The wider spacing of isotherms in the wake of the laser spot show the cooling of the sample, which is relatively gradual, compared to the heating, giving rise to the droplet-shaped isotherms, which results from the heat conduction in the solid. Various heat fluxes are shown in this figure, as described in Table 9. Since the work piece represent the modelled domain, these heat fluxes are applied as boundary conditions on the applicable surfaces. The radiative heat flux operates on all boundary surfaces, the thermal contact on the boundary surface between the specimen and its resting surface, and the convective heat flux on the top of the specimen.

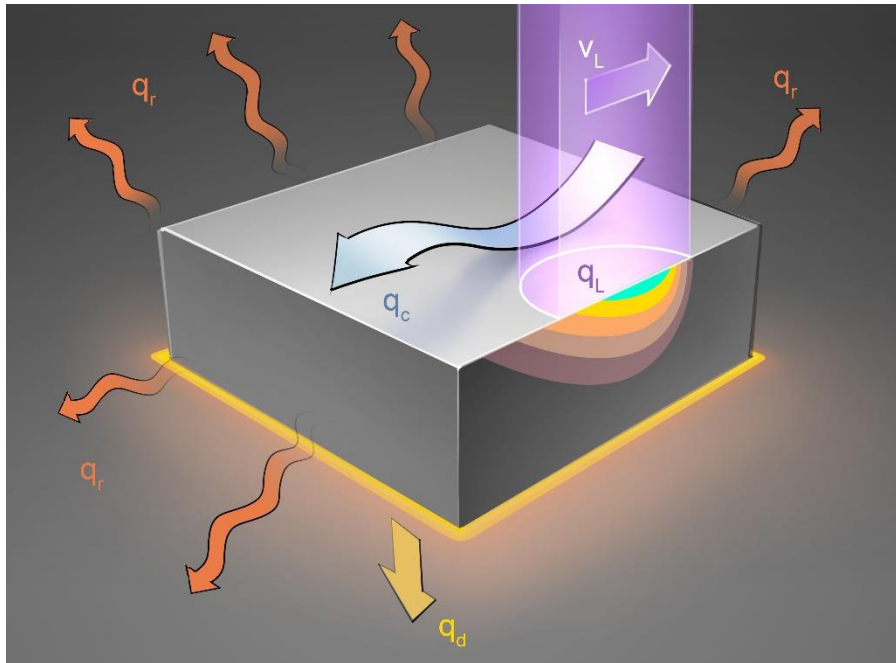


Figure 22: A schematic of the laser heat treatment. The laser heat flux, denoted by q_L , is shown to be moving across a specimen at velocity v_L . This causes a temperature field, schematically shown by the isotherms. Radiative (q_r), convective (q_c) and contact (q_d) heat fluxes are also schematically represented.

4.4. Transient Properties

As described in Section 2.3.2, several physical phenomena and the metallo-thermo-mechanical coupling effects which describe their relations, are considered in the literature regarding this subject. For the purpose of this work, the phenomena Temperature and Microstructural Change were considered, along with the two coupling effects describing their interaction: Phase Transformation Kinetics, and Phase Dependent Thermal Properties, as shown in Figure 2. This ambition requires some notes on the nature of these thermal properties, and a description of their implementation, which is given here.

The three thermal properties which are contained in the heat equation are Heat Conductivity (κ), Specific Heat Capacity at constant pressure (C_p), and Density (ρ). These properties govern the heat conduction behaviour in solid materials, but are themselves temperature and phase dependent [30, 35]. Various sources exist, including reference books for a wide variety of alloys [77-79], but these have limited applicability due to a lack of accuracy [30]. As noted by Wilthan, Schützenhöfer, and Pottlacher [30], lack of accurate data on thermophysical properties is one of the major weaknesses of numerical simulation of various processes in the steel-working industry, including heat transfer and solidification. In this work, these deficiencies have been addressed by:

- Implementing a density-temperature curve based on dilatometric measurements.
- The use of Physical-Model assisted software, JMatPro, for C_p and κ .
- Adjustments to JMatPro data on C_p based on the phase transformation temperatures observed from dilatometry.

The thermal history, when considering the temperature field at a depth beyond the optical penetration depth during laser surface treatments, depends on the combined effect of these parameters.

Detailed thermophysical properties of the specific steel under consideration in this model could not be obtained from any literature source, and many sources, including Wilthan et al, only seriously consider high-nickel steels also containing significant amounts ($> 10\%$) of chromium, which form the family of austenitic stainless steels [51]. Extrapolating from tabulated data into different compositional or temperature ranges offers limited applications, given non-linear effects between alloying elements, and phase transition behaviour [80]. Alternatively, thermal properties can be obtained by physical model-assisted statistical software, which in the case of this project was JMatPro [60, 81], while Thermocalc and COMSOL Multiphysics® are also reported as data sources [21]. Generally, however, thermophysical data are accounted for in a simplified manner due to the lack of data, as can be seen in the overview in section 2.3.2. The thermal properties obtained from JMatPro are shown in Figure 23, Figure 24, and Figure 25.

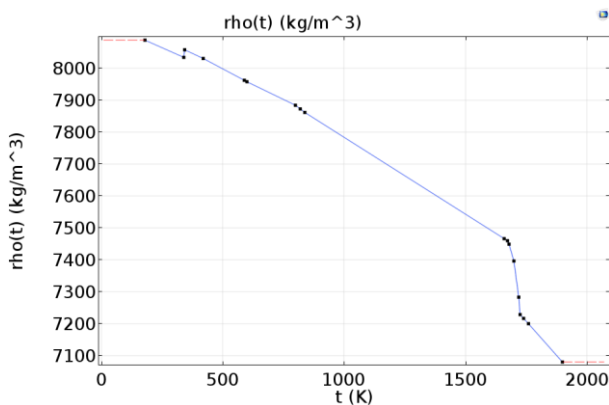


Figure 23: Density-temperature according to JMatPro

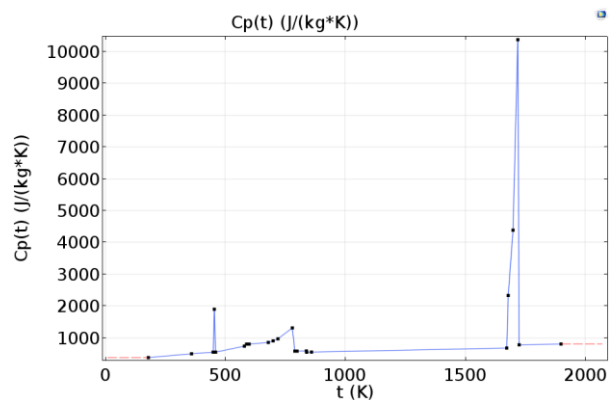


Figure 24: Specific heat-temperature according to JMatPro

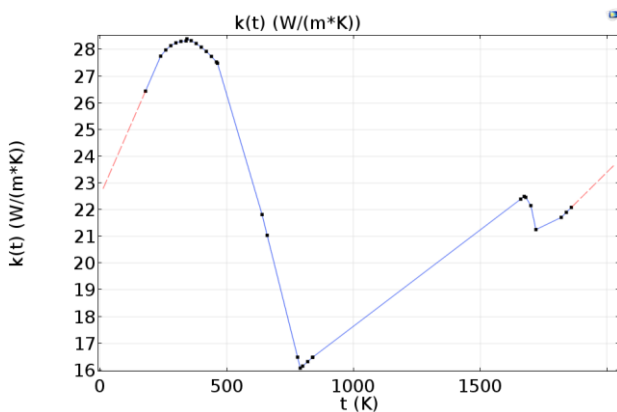


Figure 25: Thermal Conductivity-temperature according to JMatPro

Although these data are continuous over the full range of temperature that is of interest to the project, certain effects that are experimentally observed in this alloy are not captured by this software. Firstly, its phase transition from the initial cryogenic martensite, observed by

dilatometry at temperatures between 713 K and 803 K [4], is not reflected in this data. The density should change pronouncedly, reflecting the contraction measured in dilatometry for the martensite to austenite transformation. The phase transformation itself is also has a pronounced effect on the total model heat, since the latent heat of phase transformation constitutes the consumption of a significant amount of thermal energy, which is expected to influence the temperature field. The latent heat can be implemented through the heat capacity, which is given by equation 15 [82, 83]:

$$\Delta c_{p,\alpha\rightarrow\gamma} = \frac{\delta\Delta H_{\alpha\rightarrow\gamma}}{\delta T_{\alpha\rightarrow\gamma}} \quad (15)$$

Where the heat capacity is the temperature derivative of the enthalpy. Through this approach, and based on data for a comparable alloy [84], a latent heat of transformation was estimated for the steel.

Furthermore, a phase change hysteresis should be reflected in the model, where the nodes that have experienced transformation to austenite by heating to temperatures higher than A_f , should be assigned the thermal properties appropriate to that phase. An approach was set out based on a domain Ordinary Differential Equation, a mathematical modelling tool present in COMSOL Multiphysics®. To this end, a phase parameter $\Theta \in [0,1]$ was defined, where the 1 denotes the initial martensitic microstructure, 0 a fully austenitic microstructure, and any ratio a mixture of these two. The nodal property Θ was assigned based on conditional statements, relating the phase nature to the highest attained temperature at that node, ensuring that once a temperature above A_f is reached in a node, that the part of the model it represents will be treated as austenite, even when the temperature falls below A_s subsequently. The thermophysical properties of either phase were assigned to a node based on this phase parameter.

5. Results and Discussion

In this chapter, the dilatometric results are presented first, as they constitute a substantial part of the information required in the model of the laser heat treatment. Additionally, the first part of the chapter includes a characterisation of the bulk microstructures formed by the initial and dilatometric heat treatments, to fully describe the material characteristics, as well as the carbon content obtained from combustion Infrared Detection. These results will be discussed separately from the laser heat treatment related results after they are presented, since they do not depend on either the model or the laser heat treatment's results.

Following this, the obtained model results are presented, and compared with thermocouple and LAZ size measurements, in order to validate the model. Lastly, microstructural characterisation by optical microscopy and EBSD, and hardness profiles of the laser heat treated samples, are presented. The model validation is discussed independently, and the microstructural characterisation of the LAZ microstructure is discussed based on both model results, and the insights obtained from the dilatometry, bulk microstructure, and carbon content.

5.1. Effect of heating rate on surface and bulk microstructures

5.1.1. Phase transformation temperatures

The onset temperature, denoted by A_s , and the finish temperature A_f , of the austenite reversion phase transformation, are of interest because their behaviour relative to heating rate hold information on the mechanism of phase transformation [26, 27]. Furthermore, strong variations of A_s and A_f with heating rate would need to be accounted for in the model, since strong heating rate gradients exist in laser surface treatments. Note that the nomenclature A_s and A_f is used by authors in this field to specifically denote the reverse transformation from martensite to austenite [23, 26, 27], but that they are basically equivalent to A_{c1} and A_{c3} respectively [25].

Dilatometry was carried out over a wide course of heating rates to obtain the transformation temperatures. They are obtained from the dilatometric data by obtaining the temperature at the point where the signal deviates from the linear coefficient of expansion of martensite (A_s) and when the signal starts conforming to the linear expansion coefficient of austenite (A_f), denoting the end of transformation. A graphical representation of this is seen in Figure 26, which shows the dilatometry response of a 10 K/s heated solid specimen. Starting at zero length change and room temperature, a linear increase in length is observed upon increasing temperature, up until the A_s temperature. Here, the phase transformation starts, reflected by the non-linear region between A_s and A_f . The phase transformation is measured as a contraction in the length, since the density of austenite is higher than the density of martensite. When the phase transformation is complete, at A_f , the length increases linearly with temperature, similarly to the initial heating. The slope of the linear expansion is different, corresponding to the different thermal expansion coefficients of martensite and austenite. Heating continues up to 800 °C. During cooling, the edge thermocouple signal is at a consistently lower temperature than the central (temperature control) thermocouple. Therefore, controlled cooling at 20 K/s is concluded to occur without complete temperature homogenisation along the sample length direction. This is due to heat conduction limitations, and higher cooling rates at the pushrod contact, likely due to differences in the flow of quenching gasses between sample centre and edge.

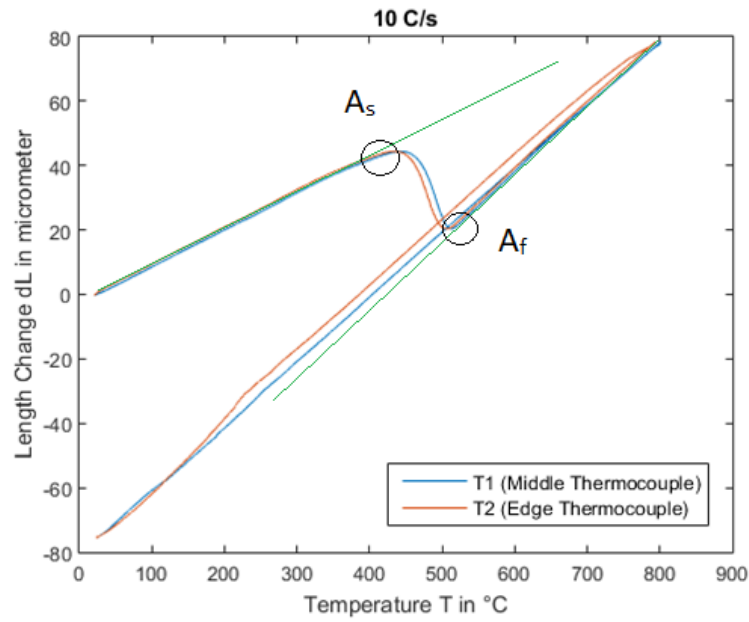


Figure 26: Schematic for determination of phase transformation start and finish temperature from dilatometric data. The green lines show the linear regions.

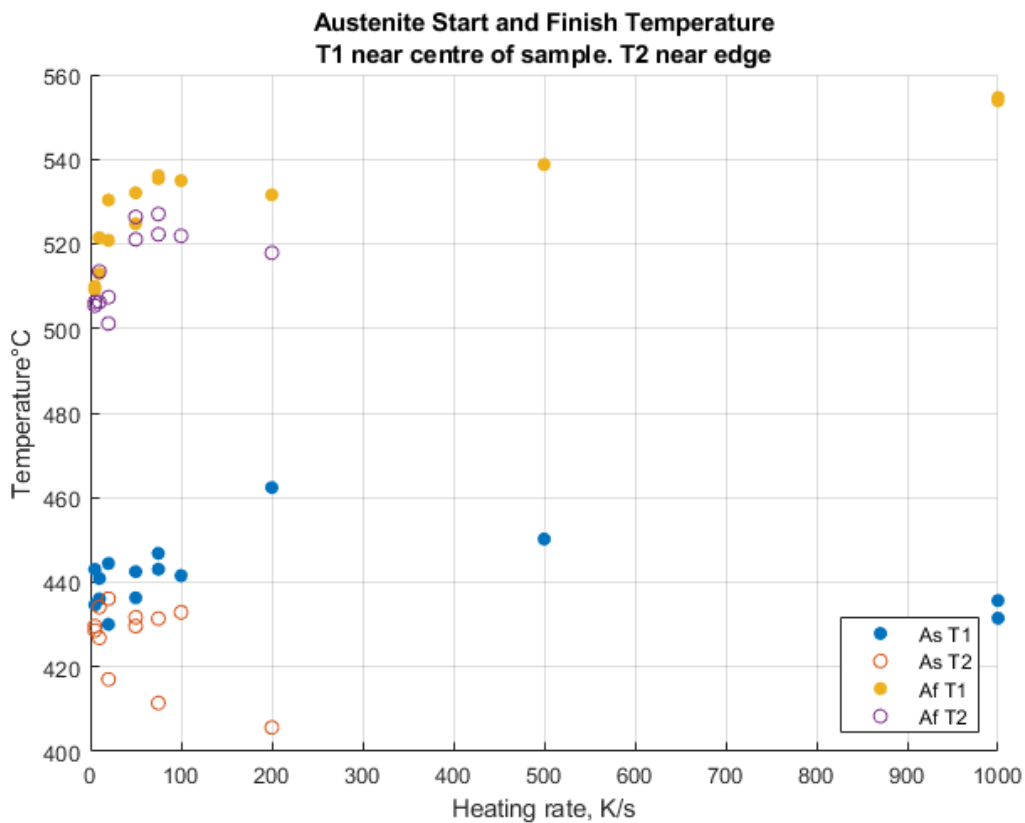


Figure 27: A_s and A_f as a function of heating rate

After the post-processing, A_s and A_f could be determined from the data, and the results of which is shown in Figure 27. This figure shows the A_s and A_f temperatures as a function of heating rate for both thermocouples, T1 and T2, denoting sample centre and sample edge,

respectively. For the 500 K/s and 1000 K/s samples, only T1 was measured, since the heating coil making the high heating rates possible restricted the available space to attach the thermocouple. The temperature at the sample end, T2, gives a consistently lower value than T1, denoting some delay in temperature homogenisation across the sample. This is likely due to non-uniform heating and thermal conductivity limitations at this timescale. It should also be noted that the T2 data for 200 K/s as obtained from the post-processing method seems to show the limitations of the shape language model for obtaining usable data, since the range between T1 and T2 is unusually large, and the signal quality for this T2, as can be seen in Chapter 3, is very low.

The behaviour of A_s and A_f is in accordance with data obtained on a similar alloy by Apple and Krauss [4], as shown in Figure 28. According to these authors, as well as several others [26, 27], the fact that A_s and A_f are dependent on heating rate shows that the phase transformation mechanism is not purely displacive.

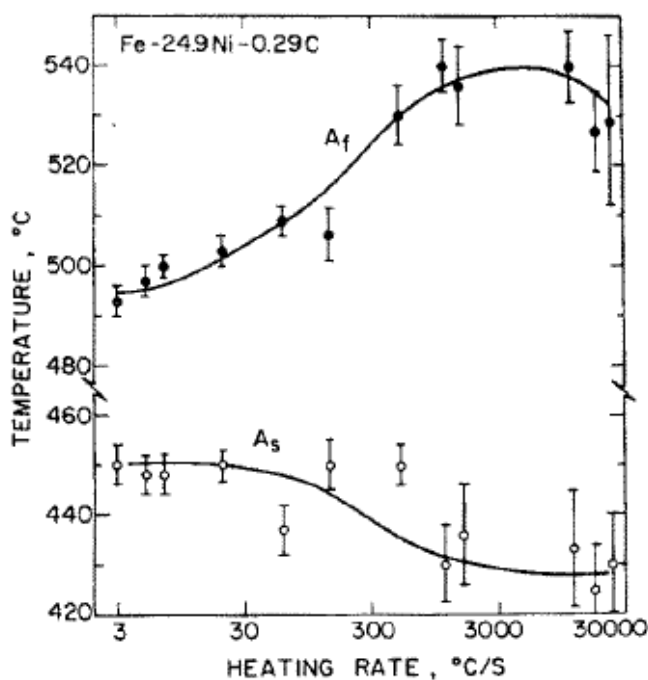


Figure 28: Dilatometric behaviour of a similar steel, as reported by Apple and Krauss, for a wide range of heating rates [1]

Behaviour of A_s

Figure 27 shows, for the low heating rates up to 100 K/s, a constant A_s at $440^\circ\text{C} \pm 4^\circ\text{C}$. This is somewhat lower than the values reported by Apple and Krauss, likely due to lower carbon content in this steel. At lower heating rates, sufficient time for significant carbon diffusion and carbide precipitation is available, which serves to stabilize the martensite during heating. At higher heating rates, the reduction in A_s observed by Apple and Krauss is not reflected strongly in the data shown in Figure 27, for the 200, 500, and 1000 K/s cases. Lower A_s temperatures at higher heating rates, above 300 K/s, are attributed to a higher carbon content in the martensitic matrix by Apple and Krauss. Therefore, the overall lower carbon content in the steel investigated might explain why the destabilisation of the martensite at these high heating rates is less pronounced.

Behaviour of A_f

The behaviour of A_f at heating rates up to 100 K/s is not discussed in detail by Apple and Krauss, although a similar trend is visible. However, the reverse transformation can be assumed to be diffusion-controlled at these heating rates, due to the gradual increase in A_f , which indicates that time is needed for the transformation to reach completion. At intermediate heating rates, 200-1000 K/s, the diffusion kinetics are not substantially increased by the higher temperature, resulting in a higher A_f due to the time required for the transformation to reach completion, rather than the temperature. Although this is the limit of the data obtained in this research, Apple and Krauss report on even higher heating rates. At these rates, from 3000-30000 K/s, a reduction in A_f is observed, which is interpreted as the transition to a partially displacive mechanism for phase transformation. Therefore, the dilatometry results for the steel provide a lower limit for transition to displacive behaviour at 1000 K/s, and the microstructures formed in the dilatometry can unambiguously be regarded as formed by a diffusional mechanism.

Behaviour of M_s

The dilatometry samples were all cooled at a controlled cooling rate of 20 K/s, which is a sufficiently high cooling rate to avoid the formation of any phase other than martensite, until M_s is reached. The data from the cooling curves was processed using the same process as the heating curves, to assess whether this transformation takes place. Here, two distinct behaviours are observed comparing hollow and solid samples. A very slight change in slope near room temperature was found in selected solid samples, whereas the hollow dilatometry samples were found to undergo clear transformation upon cooling, with a detectable M_s temperature. The M_s temperatures obtained from these hollow samples are shown in Figure 29.

A significant spread is present in these samples between T1 and T2 measurements, as well as consecutive measurements at the same heating rate (5 K/s and 1000 K/s), representing a measurement uncertainty of about 5 K. However, at heating rates between 5 and 200 K/s, a general downward trend is observed in the M_s temperature, where low heating rate austenite seems to be less stable. However, the M_s at 1000 K/s seems to deviate from this trend, although the spread between the two measurements at this heating rate is significant.

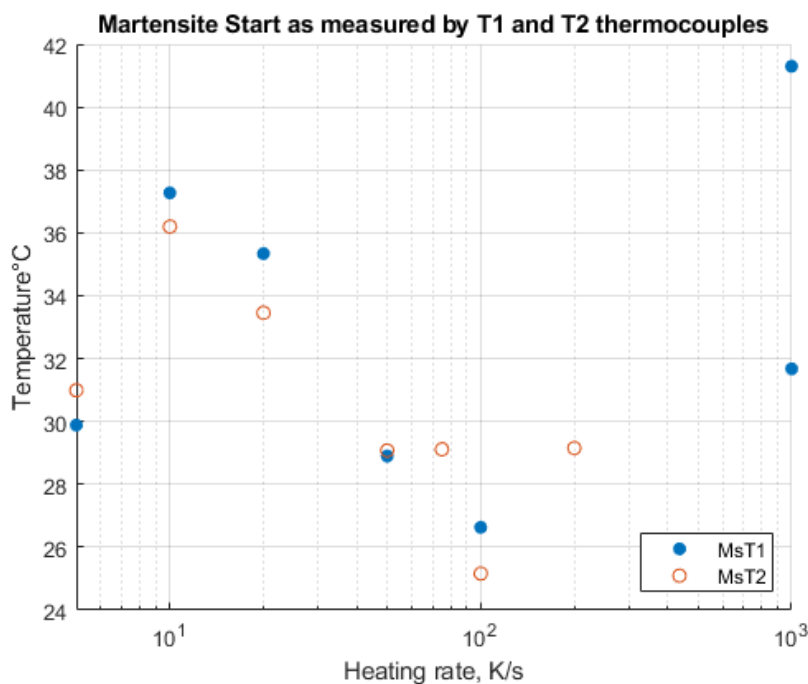


Figure 29: Martensite start temperatures as a function of heating rate

Effect of hollow samples

To ascertain whether hollow and solid sample behave comparably in dilatometry, low heating rate experiments were carried out for both hollow and solid samples, as shown in Table 5. The measured A_s and A_f for solid and hollow samples for this comparison campaign are shown in Figure 30. The transformation temperatures are comparable for hollow and solid samples, with the difference between the transformation temperatures of a hollow and a solid sample are less than 5 °C.

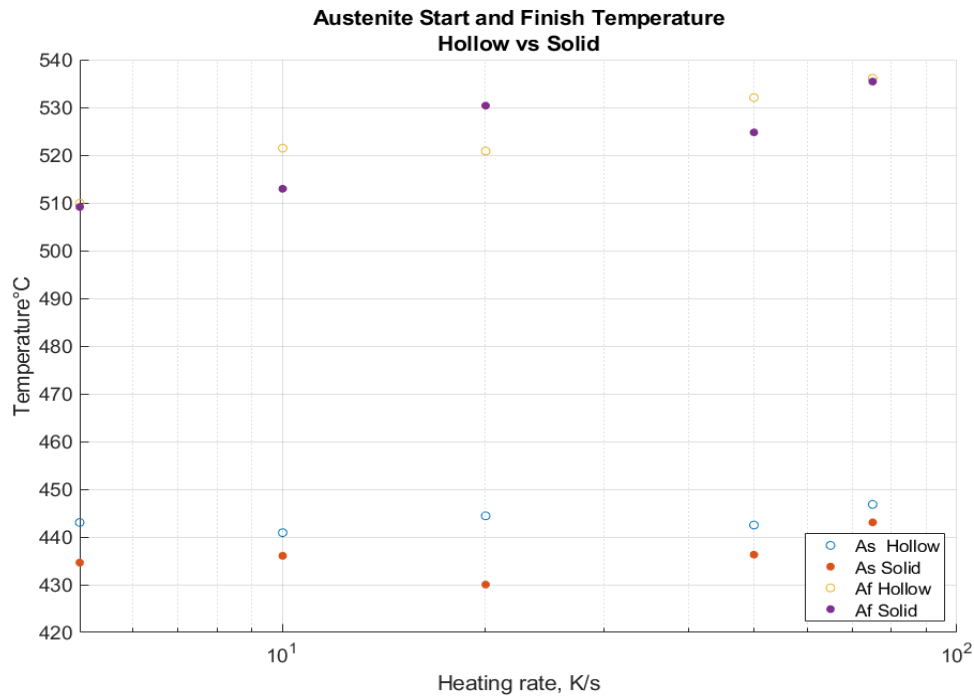


Figure 30: Comparison campaign for hollow and solid samples in terms of their A_s and A_f temperature as a function of heating rate.

5.1.2. Microstructural characterisation of dilatometric samples

The microstructures obtained after application of controlled heating rates by dilatometry were studied using optical microscopy, in order to compare these microstructures to the microstructures formed in the LAZ, at estimated heating rates.

Hollow and Solid

In Figure 32, a hollow dilatometric sample is shown, as revealed with Kalling's No.2 etchant. Several notes can be made on this microstructure. Firstly, a strongly over-etching outer layer is visible, which gradually transitions into a layer with a significant fraction of martensite, which in this case is considerably more dark-etching than the initial, cryogenically formed martensite, and shows no clear butterfly morphology. The surface layer is in the order of 100 microns wide across the sample. The sample bulk is predominantly austenitic. Some martensite is present in the sample centre, in small butterfly colonies. Lastly, it can be noted that although the sample edges show this strong over-etching behaviour, the austenite grain boundaries in the sample interior are not etched satisfactorily, since only a portion of the grain boundaries are etched.

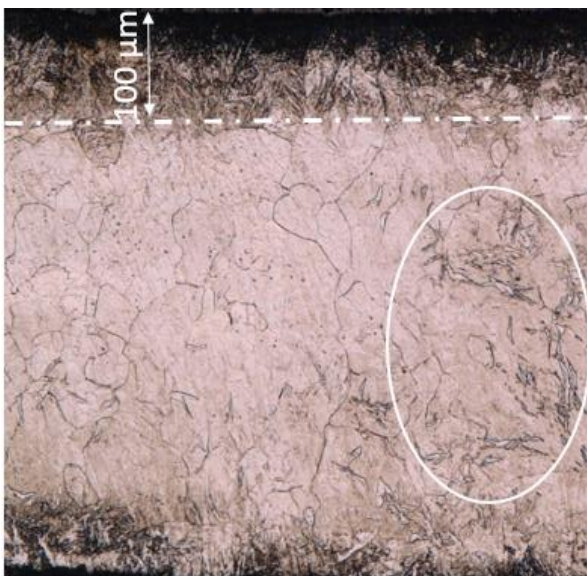


Figure 32: 5 K/s hollow sample. At the right, the sample edge is seen as a distinctly dark-etched region, along with a 100 micron transition zone. In the circle, a representative, white-etching butterfly martensite colony can be seen.



Figure 31: Solid dilatometric sample 5 K/s. The sample edge is at the right.

For a solid sample of the same heating rate, as shown in Figure 31, no martensite is observed, butterfly or otherwise. This suggests a pronounced influence of the bulk of the sample on the behaviour at the interface, as well as internally, when considering the formation of martensite, even at low heating rates. It can also be noted that the austenite grain boundaries are not distinctly etched, although the same etchant and procedure was used for both samples.

From the optical characterization here, and the observation of M_s as discussed in section 5.1.1, martensite forms upon cooling, notably in hollow specimens. As described in section

2.4.2, the austenite is metastable at room temperature and therefore, susceptible to transformation by a strain-induced mechanism. Strain during dilatometer treatments could be caused by three mechanisms: Contact forces between the sample and the pushrod, which keeps it in place, dilatation strain, and thermal mismatch strain. Dilatation strain is caused by the martensitic transformation rather than vice versa, and is reported to further stabilize the austenite, so this can be excluded. Thermal mismatch strains are also an effect, rather than a cause, of martensitic transformation, and the low temperatures differences between the observed phase transformation temperature and the end of treatment would not generate a sufficient amount of thermal mismatch strain. Therefore, this is also an unlikely mechanism. Lastly, the pushrod generates a compressive stress to keep the sample in place. This stress should be experienced by the sample predominantly at the contact points between the sample and the pushrod, and this should be reflected by a higher martensite fraction there, which, as shown in Figure 33, is not the case.

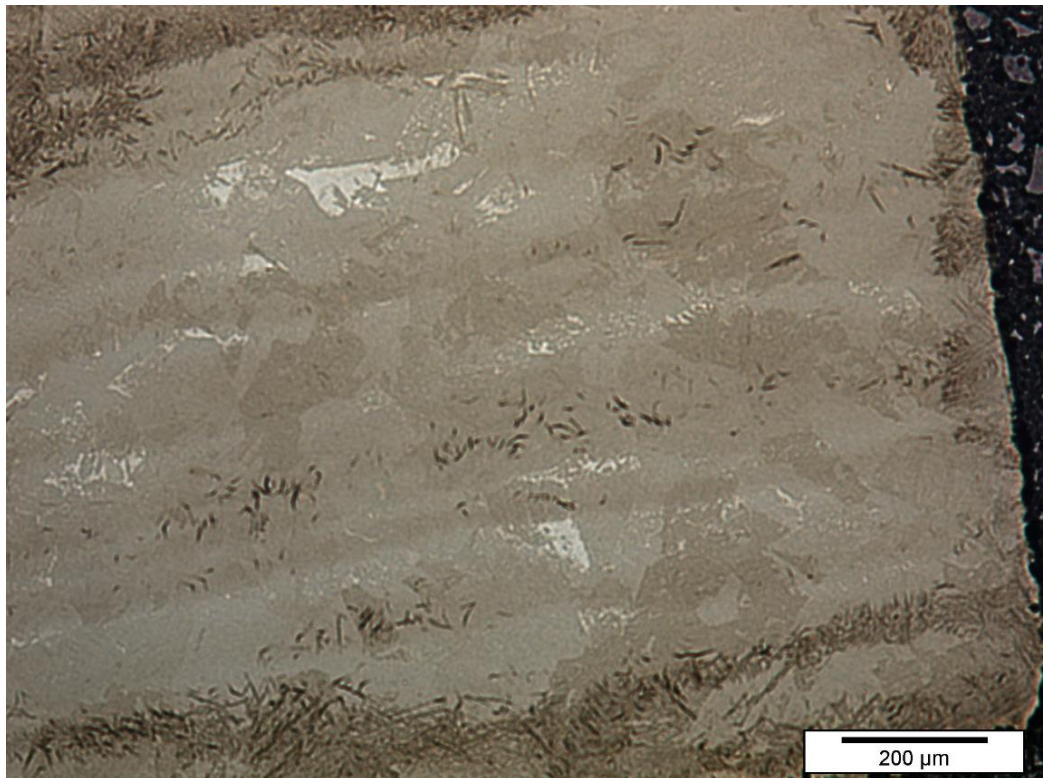


Figure 33: 5 K/s hollow dilatometric sample at its contact point (right) with the dilatometer pushrod.

The majority of martensite is present at the sample interface, as shown in the dilatometry microstructure samples. The sample interface is special in the sense that it constitutes a free surface, which significantly effects the micro-elastic stress state, and thereby, the potential for martensitic transformation, according to Wang, Jin, and Khachaturyan based on a Phase Field Model [85]. They state that at the surface, a higher volume fraction of martensite is formed, when compared to that observed in the bulk, which can be attributed to surface relaxation of the internal stresses that resist transformation. They specifically find that FeNi systems are relatively susceptible to this due to the amount of available orientation variants, which can achieve better stress accommodation than systems with lower symmetry. The absence of a significant martensitic layer in the solid samples, however, leads to the consideration that this is not the exclusive cause of the martensite formed in the hollow samples.

High heating rates

The higher heating rate samples, of which the 500 K/s sample is shown in Figure 34, show strong similarities to the low heating rates samples. A dark-etching sample edge which gradually transitioning into a modest amount of recognisable martensite, and white-etching martensite presenting in butterfly colonies at distances from the sample edge above 100 microns. Additionally, austenite grain boundaries seem to reveal more readily near the interface, similarly to the 5 K/s solid sample. In this region, extending, at maximum, 400 micron into the sample, a large number of small grains is observed, whereas there are not observed in the 5 K/s sample. The overall poor etching of austenite grain boundaries in these samples make a more quantitative determination inadvisable, and they are not observed in samples of intermediate heating rates.



Figure 34: Hollow dilatometry sample, 500 K/s. The sample edges is at the right.

These samples were also studied using various colour etchants, of which results are shown in Figure 35 for Beraha's 10/3 reagent, on the hollow 5K/s sample shown in Figure 35. This etchant does not damage the interface, which is now shown to consist of finely dispersed, small martensite grains in a somewhat darker-etched matrix, although this dark etching is predominantly observed at the upper edge, which corresponds to the outer diameter of the sample. A similar region is observed within the samples, which can be attributed to chemical heterogeneity, as described in chapter 3.1.

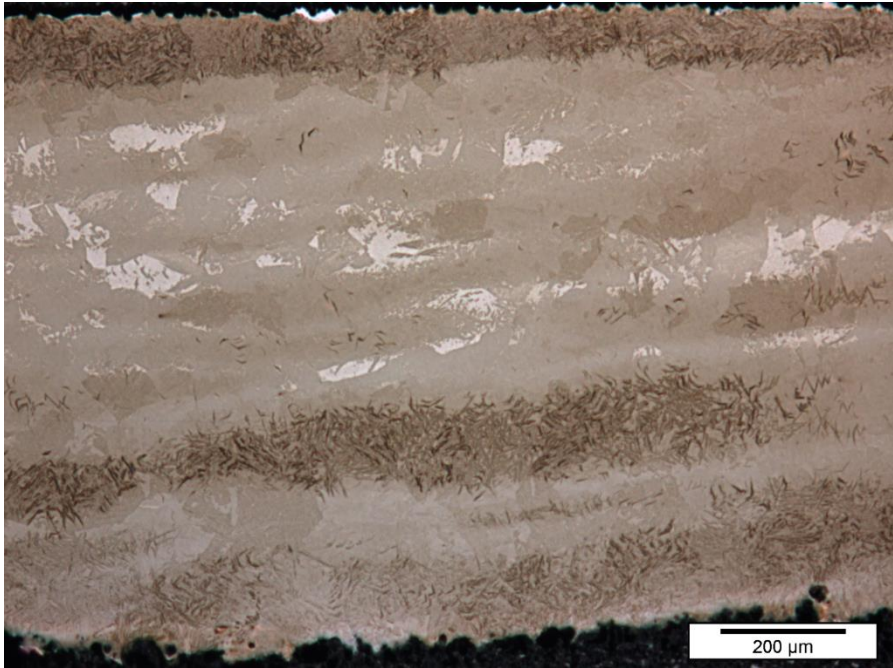


Figure 35: Hollow dilatometric sample, 5K/s, etched with Beraha's 10/3 reagent.

5.1.3. Assessment of decarburization in the surface

The effect of decarburization on the presence of martensite in the outer layer was investigated for solid and hollow specimens, based on the alloy data presented in Table 4, section 3.1. In this table, a clear increase in M_s is observed in this alloy for a decrease in carbon content, due to the stabilizing effect of carbon on the austenite. At the interface, carbon can be liberated from the sample, and if so, lower its concentration, either locally or throughout the sample, depending on the extent of diffusion. This is the main reason Combustion Infrared measurements were carried out. The data show that no significant bulk decarburisation takes place in the solid samples, whereas the lower total carbon content for the hollow samples reflects a significant loss of carbon. While the solid samples can be expected to decarburise at the surface to a similar extent, the amount of carbon available in the bulk for diffusion to the decarburised layer will be significantly larger, limiting the austenite destabilization. By contrast, the hollow samples also have an internal interface at which there is potential for decarburisation, thus increasing the rate of decarburisation with significantly less bulk carbon available to compensate.

To assess to what extent the outer layer, which was shown in optical microscopy, was due to a decarburisation effect, a selection of samples was analysed by Combustion Infrared Detection. Seven samples of dilatometry proportions were selected for combustion infrared detection. All of these samples were dilatometry samples as sketched in Figure 11, four of them solid, and three of them hollow. All had undergone initial salt bath and cryogenic heat treatment. Two solid samples were tested in as-heat treated conditions, two solid samples were tested after dilatometry at 10 K/s and 20 K/s heating rates, and the three remaining, hollow samples underwent dilatometry at 10, 20, and 50 K/s respectively. Due to apparatus minimum weight limits for operation and carbon detection, these three hollow samples were combined and tested as one aggregate sample.

The results from the various samples are presented in Table 10. The measurements show a good correspondence between the untreated samples and the reported carbon content of the steel, and a negligible bulk decarburisation for the solid dilatometric samples, however, the

hollow dilatometric samples have been decarburised to a significant extent. Considering the calibration data and the results for similarly-treated samples, the confidence interval for these measurements is in the order of $\pm 0.005\%$.

Table 10: Carbon Content of various samples from Combustion Infrared Detection

	Dilatometry (Heating Rates)	Sample Carbon Content
Solid 1 & 2	None	0.197% 0.195%
Solid 3	10 K/s	0.199%
Solid 4	20 K/s	0.202%
Hollow 1, 2,3	10/20/50 K/s	0.145%

5.2. Model for the temperature field during laser heat treatment and validation

The results obtained from thermal model created in COMSOL Multiphysics® to describe the effect of the temperature field on the microstructural development in the work piece are presented here. A general overview of the main outputs is given, followed by a validation based on the thermocouple measurements.

5.2.1. General model results

The two model outputs, temperature and phase parameter, are presented here for an overview of the laser heat treatment effects on the work piece. Figure 36 shows the temperature field obtained in the system, details of this figure are as follows. Firstly, the considered geometry consisting of two blocks is shown, where the upper block represents the work piece, and the lower block the plate the material rests on during heat treatment. The inclusion of this lower block is due to its contribution to the heat flow, through the thermal contact boundary condition, described in section 4.4.2. Secondly, the model is truncated by a section through the ZX-plane, which corresponds to the middle of the work piece and resting block. This truncation is necessary to reduce model size and computation time, and is implemented through the symmetry boundary condition, also discussed in section 4.4.2.

At the top of the work piece in Figure 36, a hot spot can be discerned, corresponding to the current position of the laser heat flux. The transient nature of the thermal field is exemplified in Figure 36, given the low temperatures, ca. 600 K, in the negative x-direction along the same line. This area was subject to the laser heat flux, tenths of seconds earlier, and experienced similar temperatures to those observed within the spot centre, in the order of 1100 K.

The temperature field affecting the work piece is to a large extent dependent on the spot size employed in the model. Temperatures in excess of A_r , which is at about 813K, are mostly experienced within the laser spot, and heat propagates into the sample, up to a depth in the order of 500 micron. The reason for this predominantly downward propagation of heat is the smaller thermal gradient along the work piece's upper surface during the laser heat treatment. A further contribution to this is the concentration of intensity in the centre of the laser spot, due to the Gaussian power distribution, which contributes strongly to the concentration of heat in the centre of the laser spot. An effect on temperature in the work piece is experienced at much further distances, however, since the sample bulk is not sufficient to mitigate the heat effects completely.

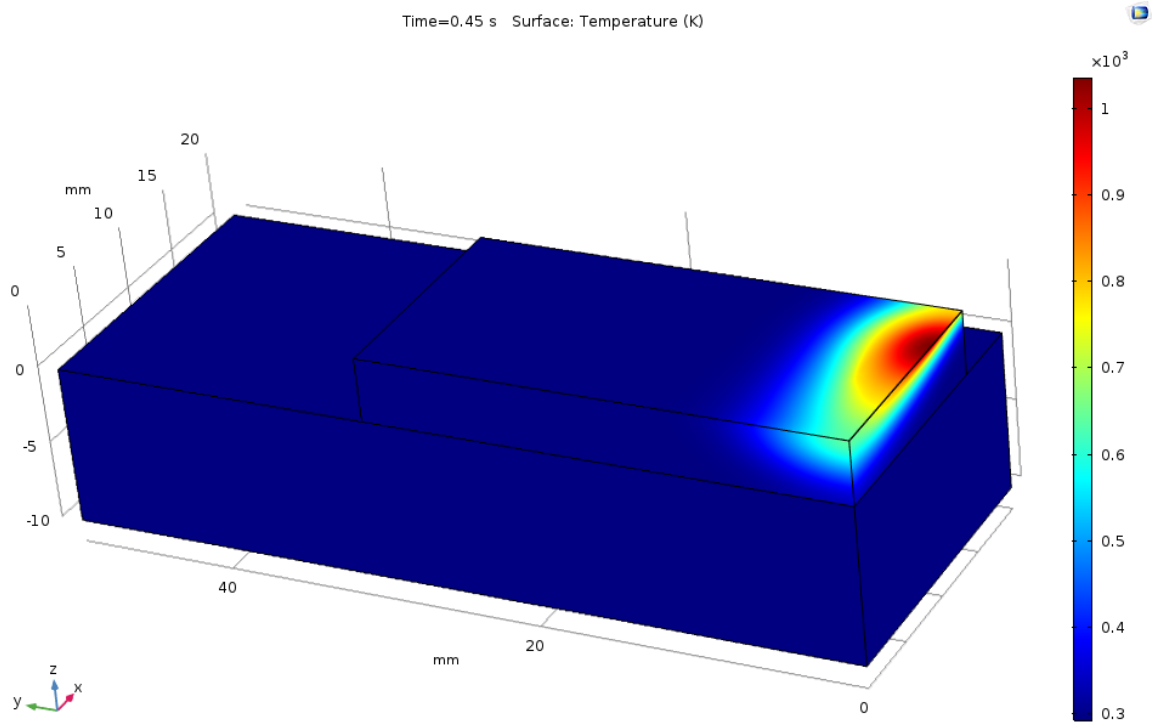


Figure 36: Overview of the thermal model, temperature scale in K.

The side view and cross section view, represented in Figure 37 and Figure 38, respectively, show the limited penetration of the heat. The laser spot in these figures has a radius of 2.87 mm, while the penetration depth of temperatures high enough for austenite reversion is in the order of around 600 μm .

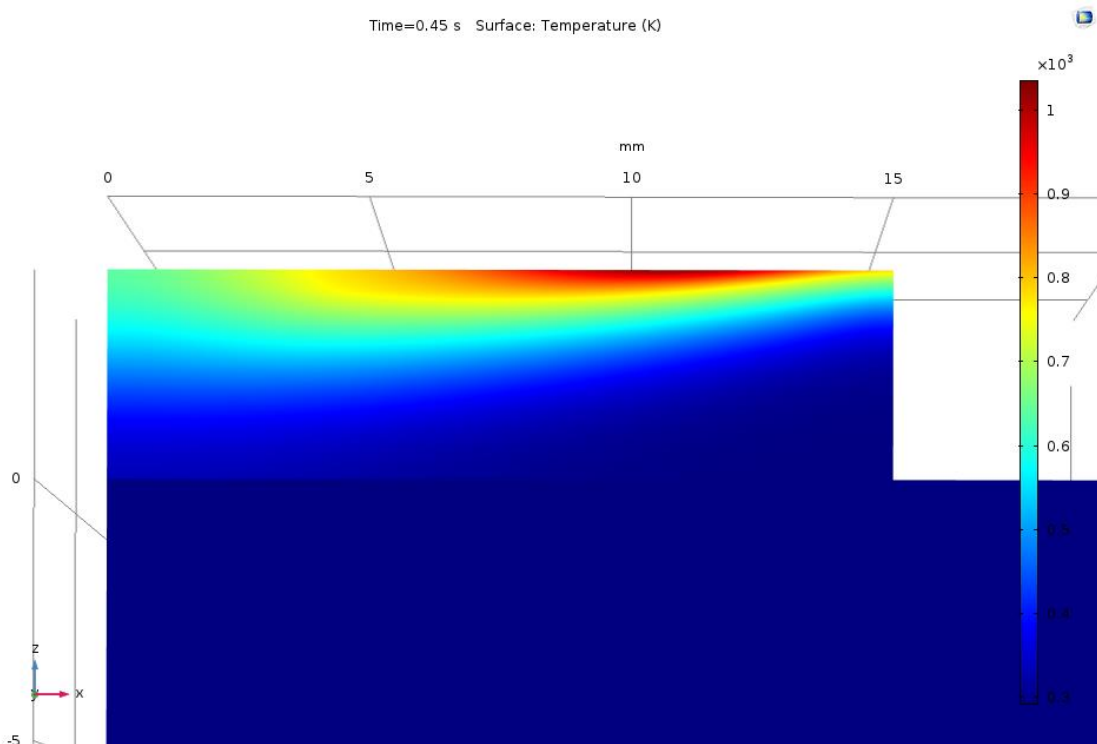


Figure 37: Side view (zx-plane) of the thermal model

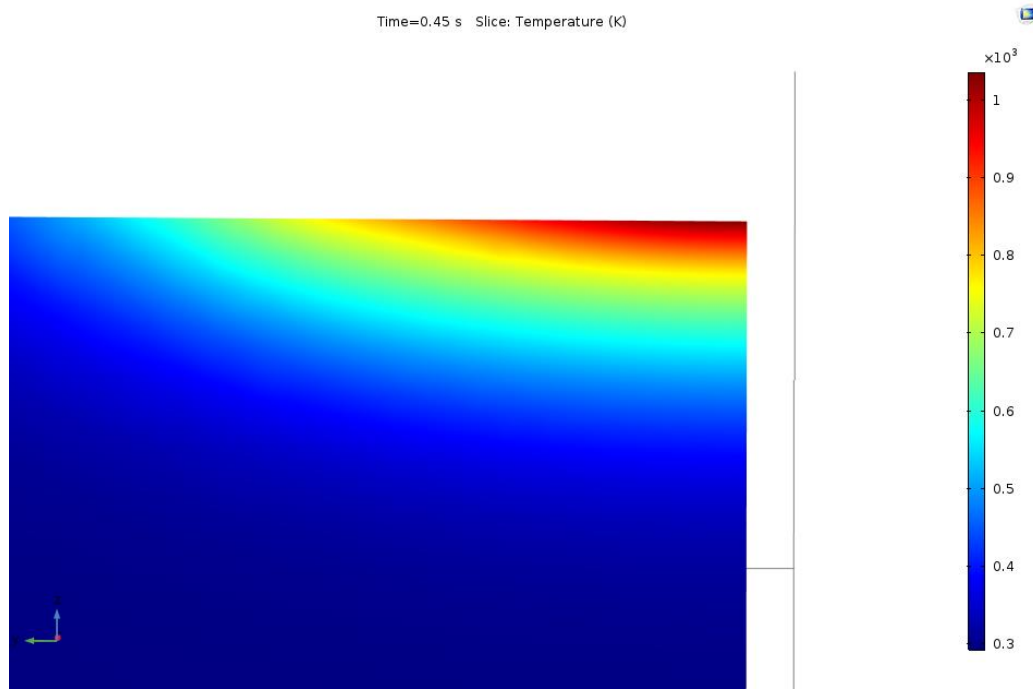


Figure 38: zy-plane slice through the centre of the laser spot.

The phase parameter, due to its intimate connection with the peak temperature experienced at an arbitrary point within the work piece, shows a similar distribution. However, due to the explicit modelling of hysteresis, the results do not change further upon cooling, as shown in Figure 39. This overview shows the modelled extent of the austenite zone after the sample has cooled to room temperature. Some variations in width along the sample length are observed and correspond to visual observations made during laser surface treatment.

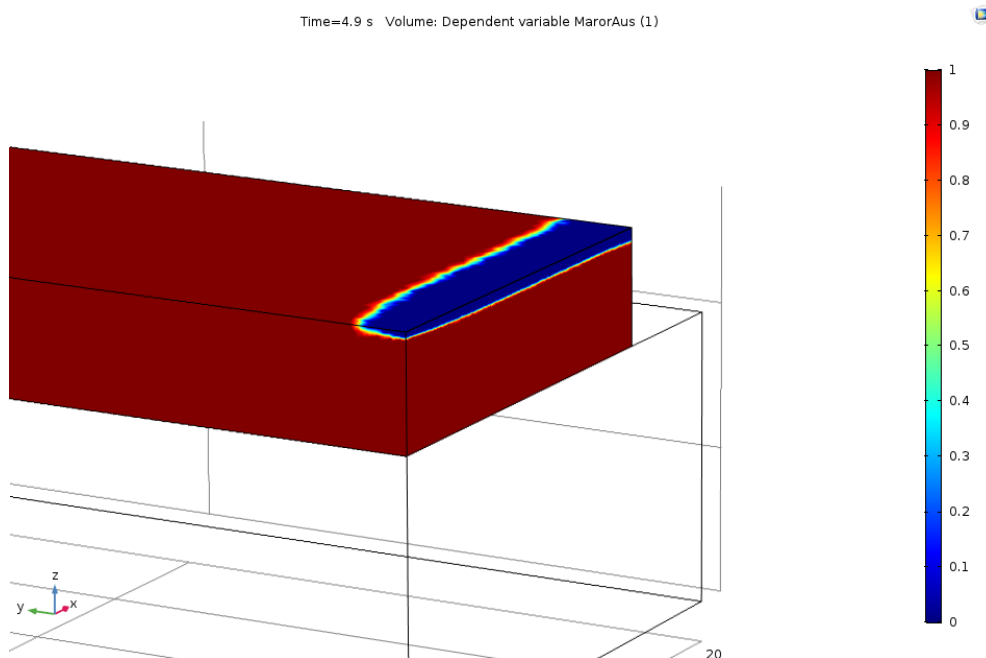


Figure 39: Overview of phase parameter at the end of laser heat treatment. The phase parameter of as-quenched martensite is 1, and fully austinitized regions are denoted by 0.

5.2.2. Temperature validation

The extent of the zone that experiences heating according to the model is sufficiently large to justify the use of thermocouple measurements, as shown in Figure 18, to validate this model. Due to the intensity of the heat flux, these thermocouples need some separation from the laser heat treated location, since the laser power is such that thermocouples can be severed from the sample if placed too close.

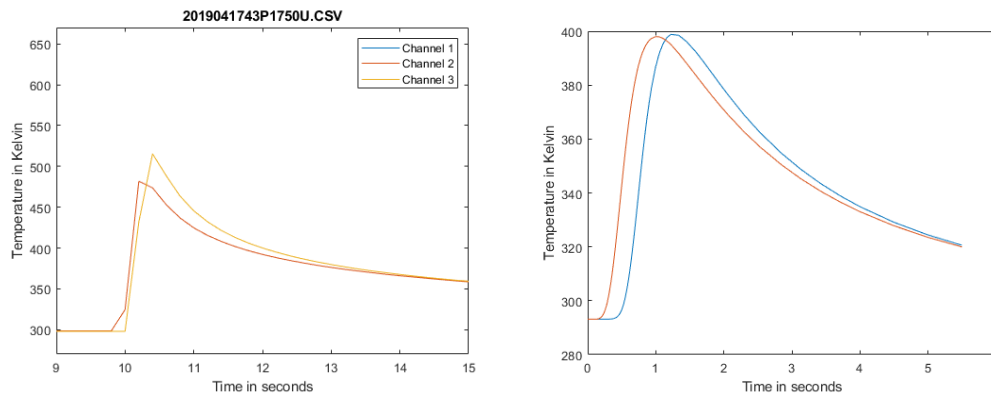


Figure 40: Thermocouple measurements (left) and model estimations at the same location (right) of two locations on the underside of the work piece

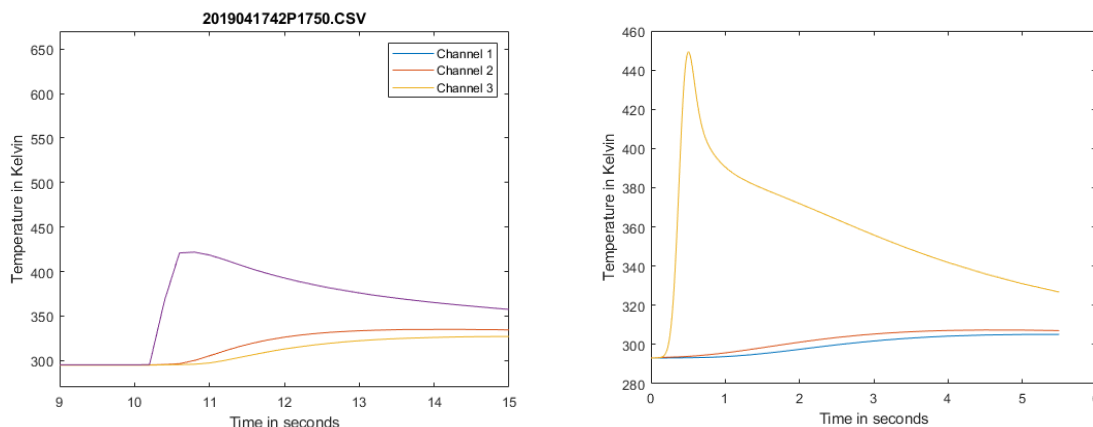


Figure 41: Thermocouple measurements (left) and model estimations (right) of three locations at the top of the work piece.

Figure 40 shows the thermal history at two points at the underside of the sample relative to the laser heat flux. Here, a significant difference, in the order of 100 K, on a total measured, temperature difference of 200 K, can be observed. This difference, apparently caused by a distinct influence on the temperature field in the bulk, is most likely due to the latent heat of transformation, which is why this is identified as a critical parameter for the sensitivity analysis.

The data shows a very close correspondence of peak temperature and heating rates at the top of the work piece for the thermocouples placed on top of the sample, as seen in Figure 41. The heating rate and peak temperature are even somewhat overestimated, but this may be an artefact of limited sampling rate of the thermocouple measurement, which does not perfectly capture the narrow peak associated with the heat transport at this location.

5.2.3. LAZ based validation

The LAZ-based validation using the factorial design campaign was carried out to assess how well the model predicts the LAZ. Important to note in this case is that the thermocouple measurements are the most significant validation method, for the following reasons:

1. No observer judgement required to decide where a region, e.g. the interface, starts and ends.
2. Even if a consistent and model-compliant choice was made, the observed microstructure may very well be subject to effects that are explicitly not considered in the model, such as thermal (mismatch) strains.

Nevertheless, this validation serves an important purpose. If the thermocouples are accurate within an acceptable margin in terms of heating rates and peak temperatures, the heat transport model is validated. However, the modelled extents of this microstructural zones may be completely different to the observed measurements. If so, this would clearly demonstrate the need for the inclusion of more metallo-thermo-mechanical couplings, most likely those prevalent at the interface, like dilatation strain and thermal mismatch strain, which may cause martensitic transformation.

Table 11: Low-powered laser models compared to measured results

Run	A _r Depth Model (μm)	Measured depth (μm)	A _r Width Model (μm)	Measured width (μm)
5	520	484	1140	922
6	615	611	1165	1113
7	620	586	1142	1097
8	960	1072	1366	1578

In Table 11, the measured extent of the laser austenitized zone and the model prediction of this zone are presented for 4 runs. These represent the experimental conditions of the low-power samples, as presented in Table 6, and show a relatively good match between modelled results and the measured extent of the laser affected zone. The measured depth and width were based on the extent of fully austenitic microstructure, and therefore, are compared to the depth at which A_r is reached by the model, i.e. the model-predicted fully austenitic microstructure. The depth of the LAZ is slightly overestimated, by up to 30 μm, in all cases except run 8, where it is underestimated by a large margin of 110 μm. Run 8 represents a very low laser velocity of 2.5 mm/s. Comparing the model results to measured width, the LAZ is also overestimated by the model, by a margin of 40 – 220 μm. A similar discrepancy is seen for Run 8.

The general overestimation suggests that either the austenite formation is restricted by a non-modelled phenomenon, such as strain stabilization. The anomaly of the model results underestimating the measured extent of run 8 might be due to the absorptivity increasing with temperature [31], thereby increasing the heat input. The low laser velocity represents a longer interaction time with a high-temperature sample surface, leading to the pronounced effect of this absorptivity increase.

5.2.4. Sensitivity analysis

The model contains two parameters, absorptivity and the latent heat of the $\alpha' \rightarrow \gamma$ phase transformation, for which an estimation had to be made, due to a lack of appropriate data. The absorptivity, which controls the amount of laser power absorbed for the steel, varies strongly with specimen surface condition, and generally deviates substantially from tabulated data for polished surfaces [18, 31]. The latent heat could not be ascertained based on literature, and an estimation had to be made based on similar alloys [56, 84]. To investigate the effect of these estimates, a sensitivity analysis was carried out.

A sensitivity analysis consists of the incremental change of a model parameter from an arbitrary reference point. The altered value of the model parameter causes a change in model outputs, which is proportional to the model's sensitivity to the altered parameter. In this approach, all other parameters are kept constant. The model parameters selected for sensitivity analysis were those of the high-powered laser treatment sample 4: $P = 1750$, $v = 2$ m/min, $r_s = 2.87$ mm. For the absorptivity sensitivity, the latent heat was kept constant at 33 KJ/kg, and for the latent heat sensitivity, absorptivity was kept constant at 0.6.

The model outputs that were subjected to the sensitivity analysis were the heating rate and peak temperature, as measured by a thermocouple. Two thermocouples were selected for this purpose. The first was located on the same side of the specimen, placed 6 mm from the laser's focal point. This is referred to as the 'Top location' thermocouple. The other thermocouple was located at the underside of the specimen, 1.5 mm from the laser focal spot, and is referred to as the 'Bottom location' thermocouple. While the sensitivity analysis is purely applied to different model instances, the thermocouple locations do correspond to thermocouple locations used in the thermal measurements, in order to investigate which estimation most closely resembled the measured results.

Sensitivity to absorptivity

In Figure 42, the model sensitivity to absorptivity is shown. The absorptivity was varied in the range 0.6-0.8, based on the range of values reported by Bergstrom, for a variety of surface conditions [31]. The middle of this range, with an absorptivity of 0.7, was taken as the reference point. As can be seen, the heating rate at the top and bottom of the modelled specimen are strongly influenced by variations in absorptivity. An increase of 14% in absorptivity shows a proportional linear increase of 15-17% in modelled heating rate. Peak temperatures also increase linearly with absorptivity, although not proportionally. A 14% increase in absorptivity causes a 3-5% increase in peak temperature.

The differences between the top thermocouple and bottom thermocouple are modest, with a 1-4% higher effect on both peak temperature and heating rate for the top location. The heat conduction along the surface is sharper, since heat is not spreading radially into the depth, but linearly along the surface. This causes a faster propagation of a sharper heat pulse along the surface, and therefore, a slightly larger effect of increased heat input.

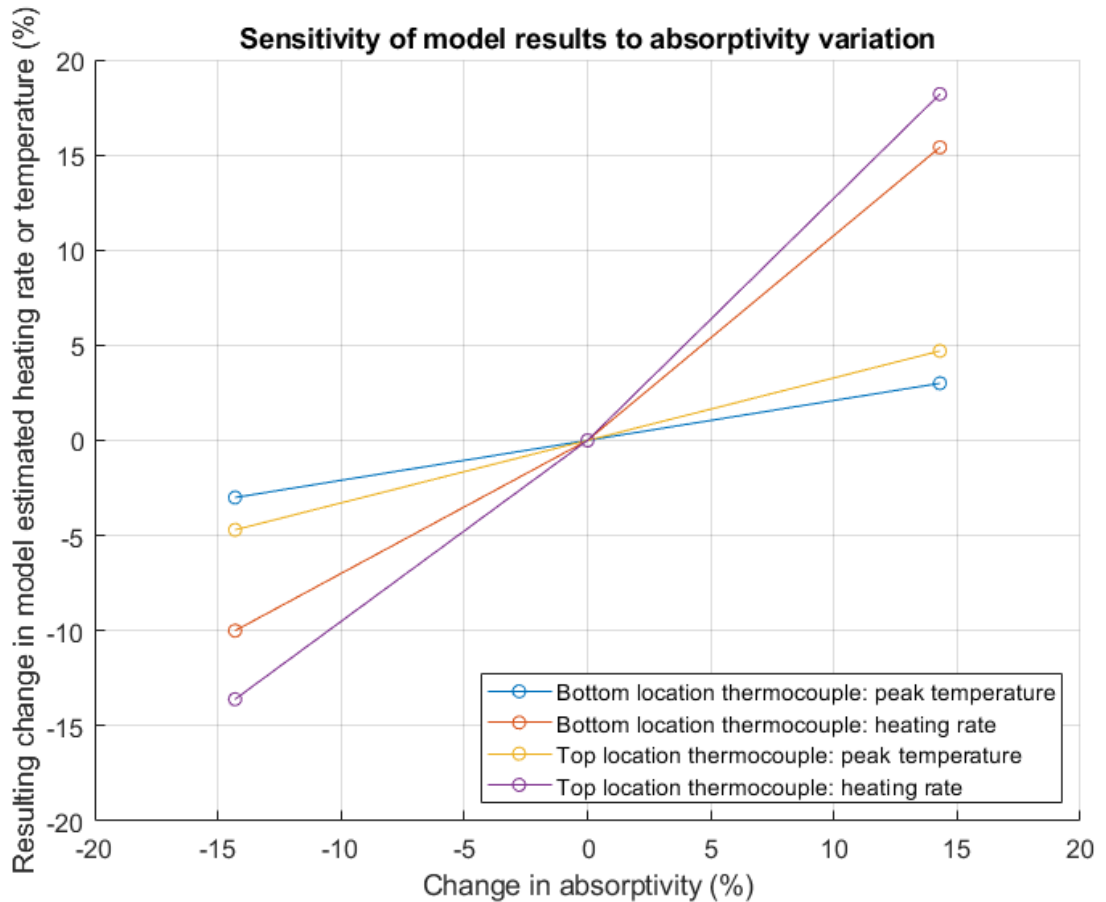


Figure 42: Model sensitivity to absorptivity. Heating rates at either location are more sensitive to variation in absorptivity, showing a proportional increase with increasing absorptivity. Peak temperatures follow the same trend but are less sensitive to the same increase.

Sensitivity to latent heat

The latent heat of phase transformation, and its contribution to the heat transfer through the hysteresis of this transformation, was deemed an important parameter to create a fully descriptive physical model. However, data on the latent heat of transformation was absent in the reviewed literature, and an estimation was made based on carbon-free [56] and chrome-containing [84] samples. Furthermore, this sensitivity analysis was carried out to account for the effect of retained austenite on the latent heat.

Figure 43 shows the effect of varying the latent heat substantially in the range 8-33 KJ/kg. The reference case was taken at 19.7 KJ/kg. The effect of latent heat on the model outputs is shown to be very limited, with changes in the bottom location temperature and heating rate of at most a few percent, for a variation in 60% in the latent heat. The clear exception is the top heating rate, which shows an increase of about 4% when increasing the latent heat from the lower limit, 8 KJ/kg, to the reference case, 19.7 KJ/kg. This is unexpected when considering the phase change hysteresis. The latent heat of phase transformation represents a heat sink, requiring thermal energy which would otherwise contribute to a temperature rise. Therefore, an increase in latent heat should constitute a larger heat sink, which reduces the thermal gradient, and consequently, the heating rate.

The sensitivity analysis showing the contrary situation may be a modelling artefact, related to the handling of the phase parameter and the effect of mesh coarsening with increased distance to the laser focal spot.

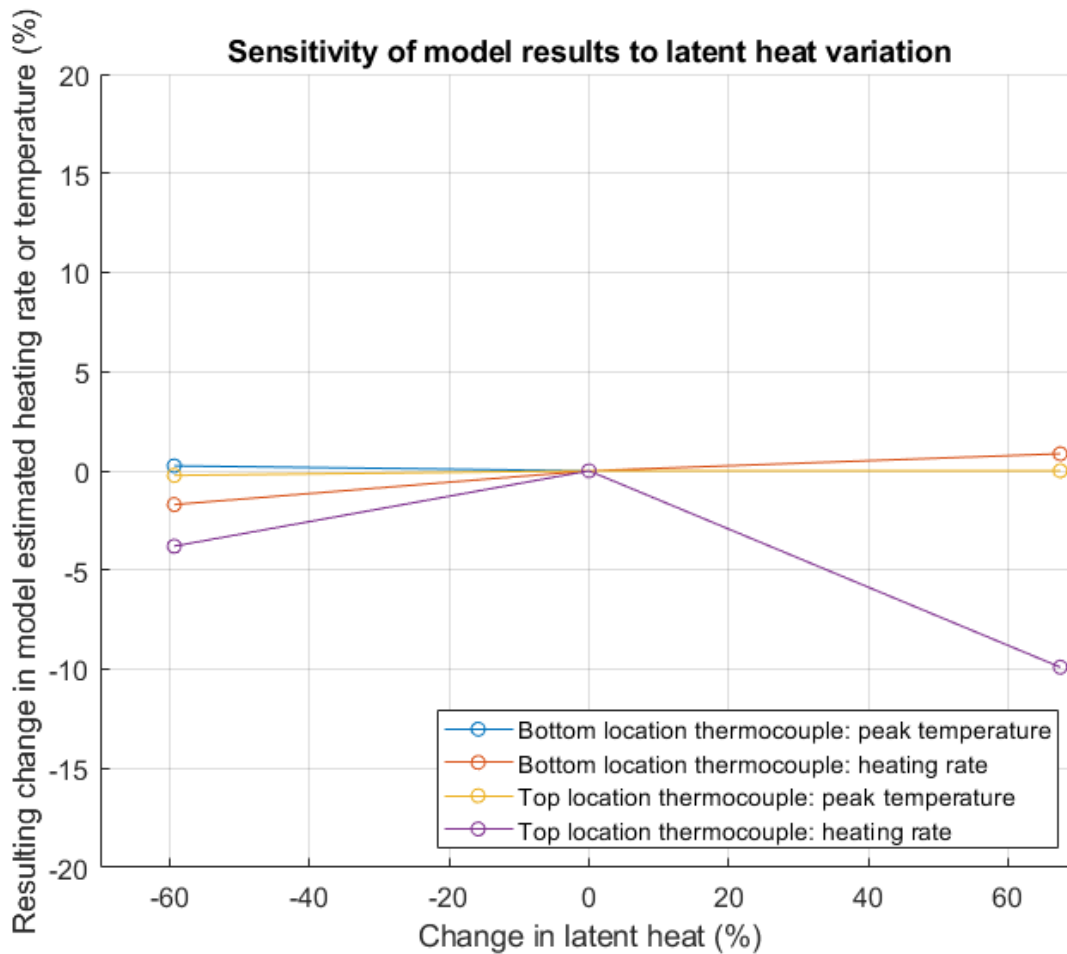


Figure 43: Sensitivity analysis of the latent heat of phase transformation. Variations of latent heat by $\pm 60\%$ have a relatively small effect on modelled heating rates and peak temperatures, excepting the modelled heating rate at the bottom of the sample..

5.3.LAZ Microstructure Validation

The microstructure of the laser austenitized zone has been analysed using various methods. The cases for which including an EBSD profile, scanning electron and optical microscopy of a 400W, small spot size sample, and optical microscopy with grain size measurement and hardness depth and grid measurements on a 1750 W, large spot size sample. These samples represent their respective classes, and were obtained with the Trumpf HL3006D and the HL4506.

5.3.1. Low-Powered Laser Sample

Figure 45 shows an EBSD depth profile of the laser affected zone in a low power sample. The austenite grains are the presented microstructural constituent, shown with an Euler angle colour map superimposed on the band contrast image. The austenite grain boundaries are marked in the image, where the white boundaries denote boundaries within a small tolerance ($\pm 2.5^\circ$) of a 60° misorientation angle, denoting a dominant twinning orientation in austenite, and black boundaries denote arbitrary misorientation. Furthermore, beyond the LAZ interface, where a martensitic microstructure is dominant, the approximate locations of the A_s and A_f isotherm have been marked, and correspond rather well with the transition from grains which

are completely austenite, and grains beyond this point were reconstructed by grouping retained austenite grains by orientation, and assigning previous austenite grain boundaries (PAGB) by a Voronoi approach.

An overview of the low power sample is given in Figure 44. In the upper left, Figure 44a, the model temperature field is shown, along with isotherms representing the austenite finish temperature (803 K) and the austenite start temperature (713 K). This figure is superimposed on the cross section of the low-powered sample 4, which is presented alongside in Figure 44b. This figure also shows the location of two hardness depth profiles. Figure 44c shows a smaller micrograph of the interface between the LAZ and the martensitic parent structure, and Figure 44d shows the results, in HV0.2, of the hardness measurement along the depth line. Based on the hardness, 4 distinct regions were identified, where the first region, with relatively small grain sizes, nevertheless has a significantly smaller hardness than the large austenitic grains somewhat deeper in the sample, region 2. Region 3, denoting the interface, is dark-etching in optical microscopy, and the hardness gradually increases up to the bulk hardness, shown in region 4. The bulk hardness is subject to a significant scatter, which is assumed to be related to the microstructural banding in the material.

Of particular interest is region 1, where the hardness is unexpectedly low. From the EBSD results, this region partially massive martensite, and partially small grained austenite. Therefore, a low hardness would not be expected. However, based on the results observed in dilatometry, if decarburisation at this surface has taken place, this might explain the formation of the surface martensite, along with the free surface effect. Furthermore, the small-grained austenite formed at below the interface, at distances between 50 and 150 microns in depth, may have formed under conditions of high heating rate, but insufficient decarburisation, as observed in the 500 K/s dilatometry sample.

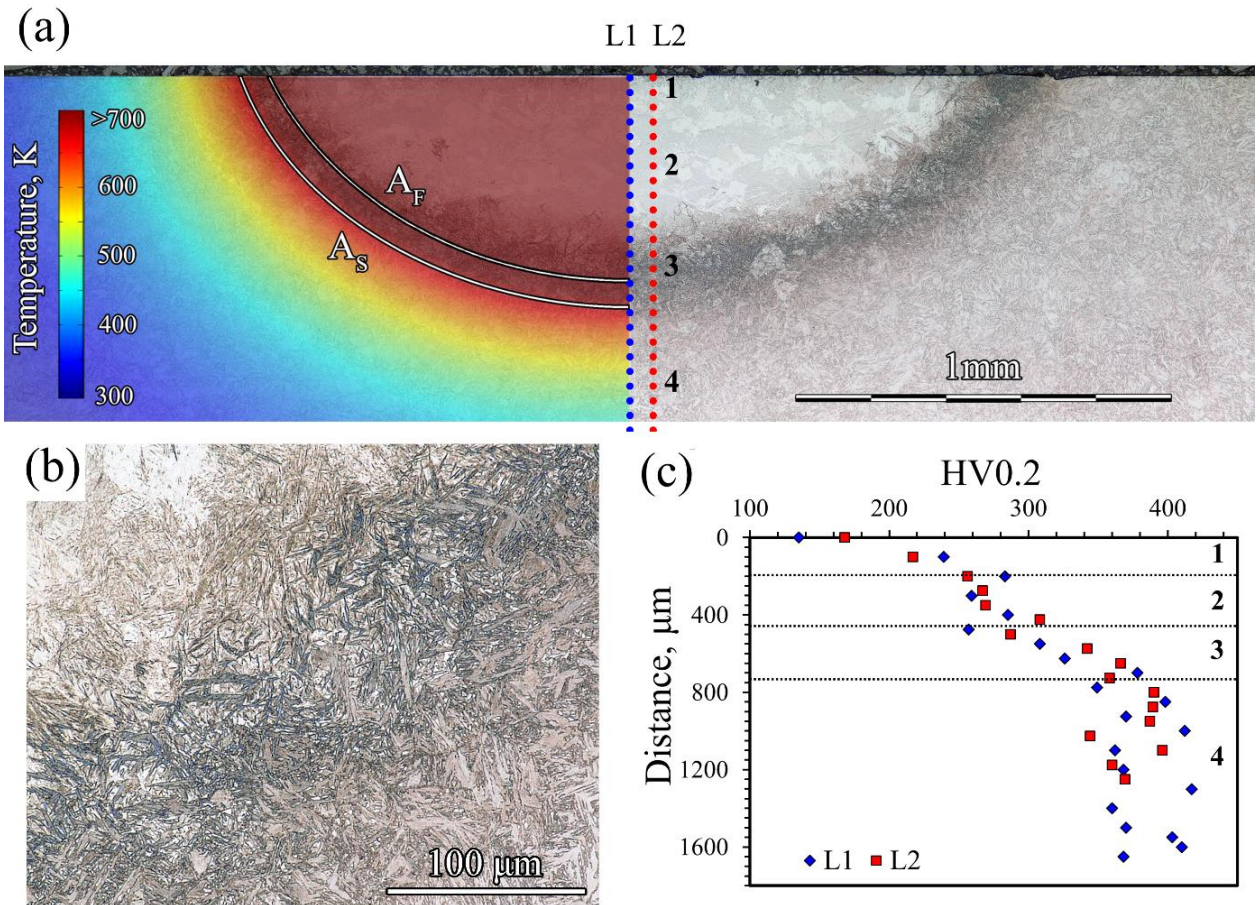


Figure 44: Low power laser sample: Model and overview (a), Microstructure of the interface (b), and Hardness (c).

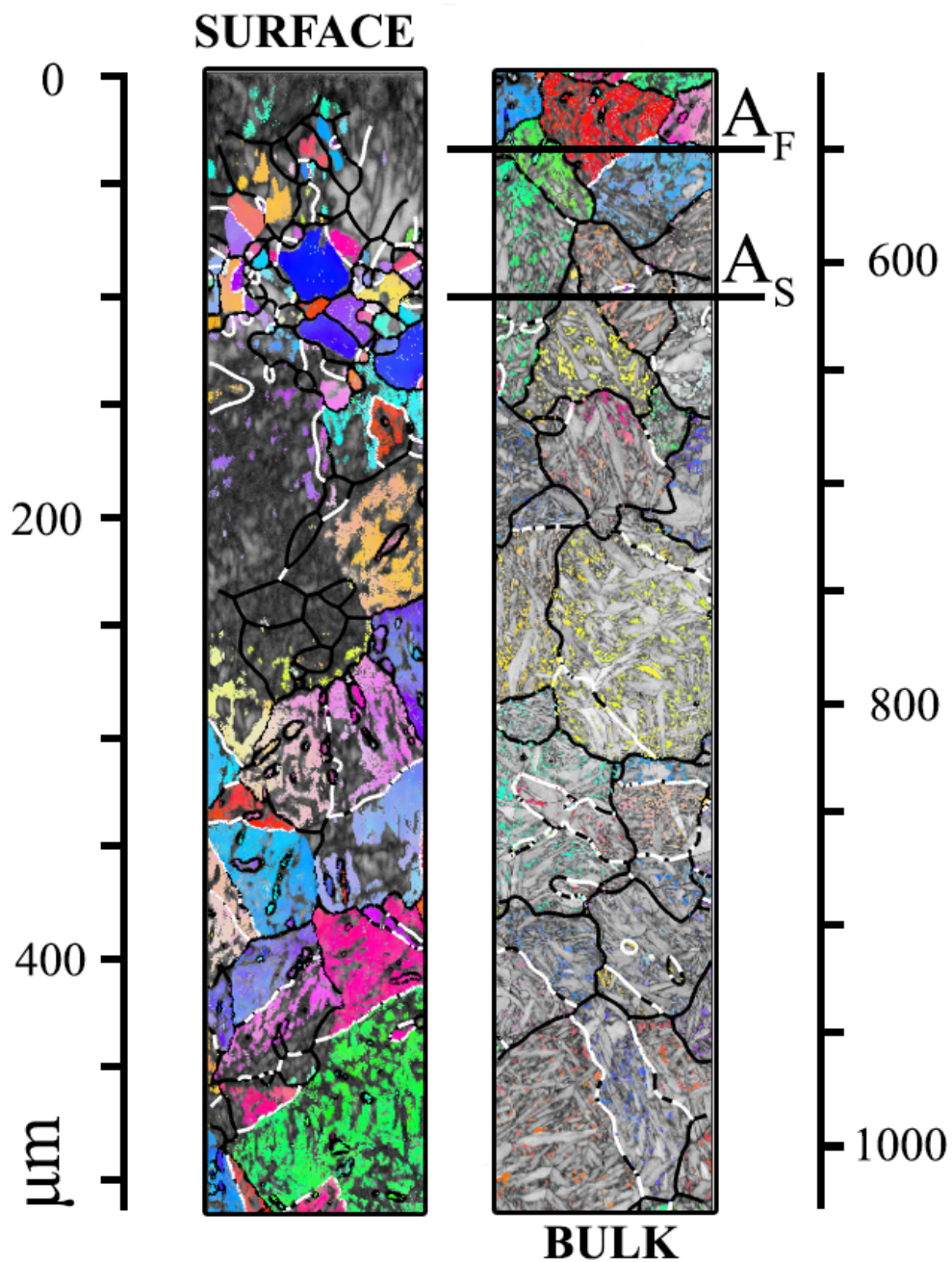


Figure 45: EBSD Depth Profile from the surface at the upper left column to the sample bulk at the lower right. A band contrast image is overlain with an inverse pole figure colour map of the austenite phase. Reconstructed grain boundaries are shown in black, whereas prior twin boundaries are highlighted in white. Additionally, the model-estimation location where A_f and A_s are reached are indicated in the figure.

LAZ-parent martensite interface

The interface of the LAZ was studied using scanning electron microscopy. This interface, also shown by optical microscopy in Figure 44b, has a distinctly different martensitic microstructure when compared to the bulk. In Figure 46 studied secondary electron images of the bulk and interface martensite are shown. The most pronounced difference is the presence of very fine, nanoscale laths in the deep-etched regions of the interface martensite, which are not present in the quenched microstructure. These laths may be carbides, studied in a comparable alloy by Apple and Krauss, using transmission electron spectroscopy [4]. They show the presence of these carbides during intercritical austenitization, in the untransformed martensite, in both low and high heating rate experiments.

precipitation, in a region where based on the model, austenite formation is to be expected, seems to be a major reason why this martensite does not transform, but stabilizes, at temperatures above A_f when considering the bulk alloy composition.

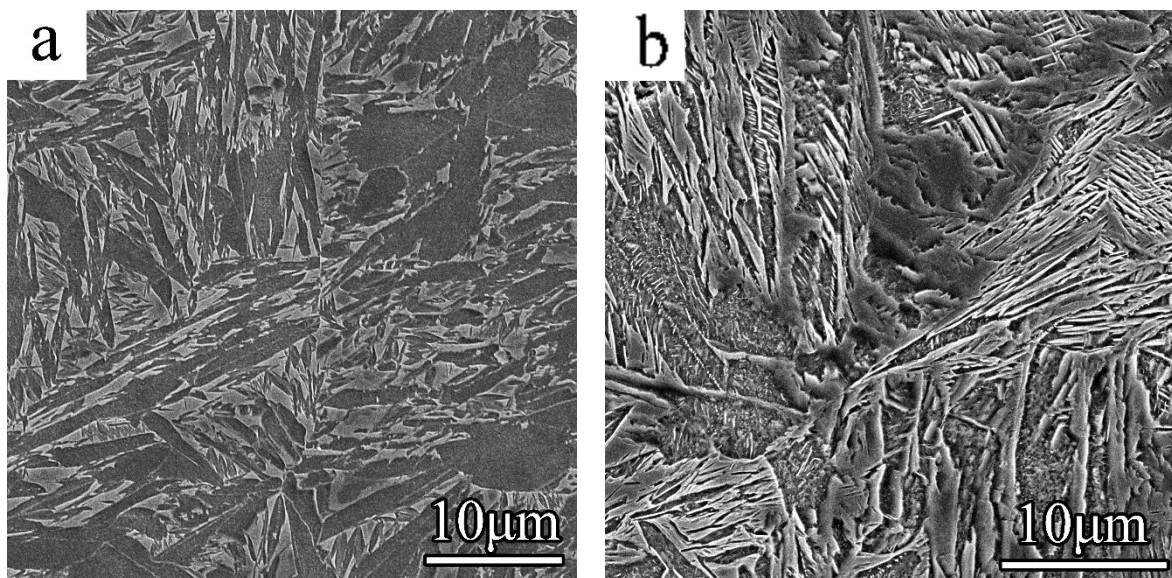


Figure 46: As-quenched (a) and interface (b) martensite

5.3.2. LAZ high-power microstructure and synthesis

In Figure 47, the microstructure formed by the high-powered laser experiments is presented. The process parameters to obtain this specimen were as follows: $P = 1750$ W, $v = 2$ m/min, $r_s = 2.87$ mm. The austenitic microstructure in the upper $100 \mu\text{m}$ of the LAZ is relatively dark-etched, and more pronouncedly so near the interface. This dark etching gradually decreases in the next $150 \mu\text{m}$, although the grain boundaries are still distinctly visible in this region. The deeper part of the austenitic zone etches brightly, and grain boundaries are only visible as very fine line. Due to the short etching time with Nital 2%, the martensitic structure is only revealed in the interface, and the bulk microstructure beyond the interface is bright and hardly etched. The overall depth of the LAZ is $950 \mu\text{m}$, and the full width (not shown) is $2850 \mu\text{m}$. The zonation, which is not present in the low-powered samples, is described in this section, along with several other aspects which distinguish this sample from the low-powered samples.

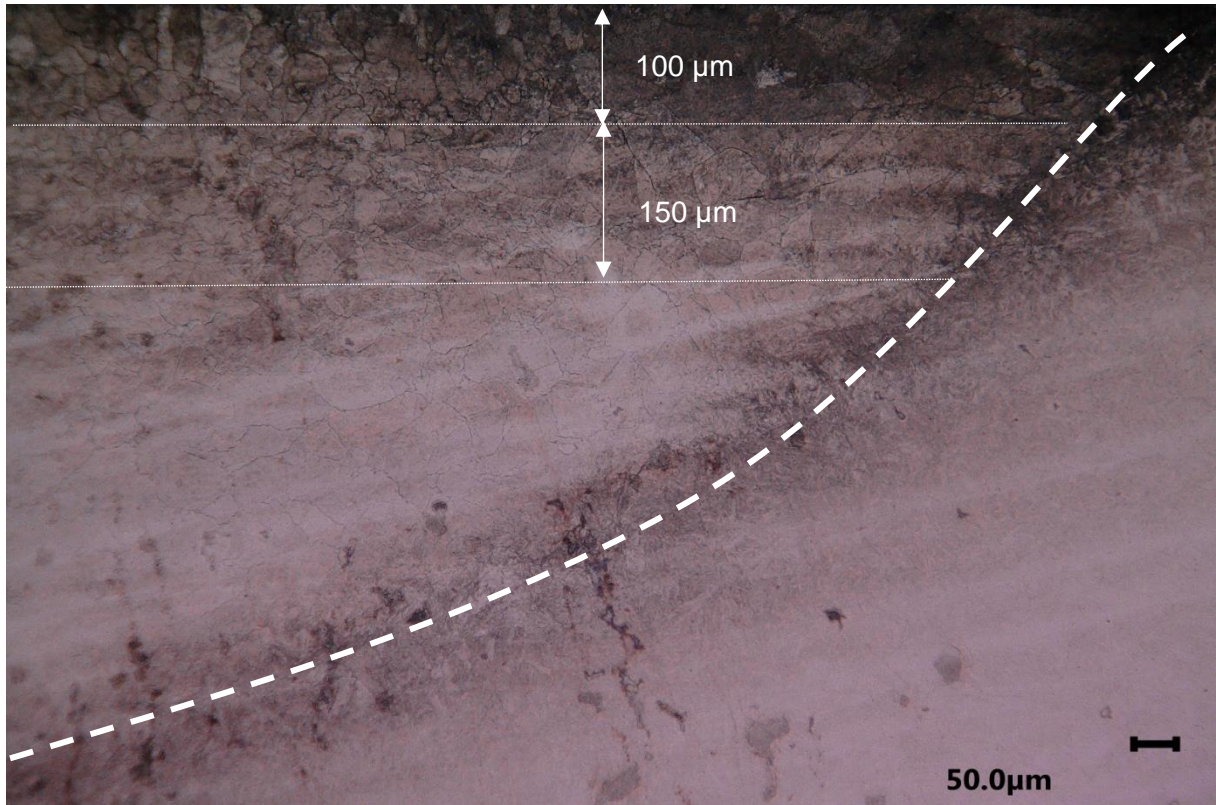


Figure 47: High-powered laser specimen 4. The upper edge of the image is the sample surface, and the relatively dark-etching interface is denoted by the dashed white line. The austenitic structure near the surface shows relatively dark etching, and wide grain boundaries. The martensitic parent structure in the lower right corner is very lightly etched. Etchant: 2% Nital pre-etch (2 seconds), followed by swabbing Kalling's No.2 (15 seconds).

Free surface and upper region

Micrographs near the sample free surface are shown in Figure 48 and Figure 49. The sample free surface shown in Figure 48 is at the centre of the LAZ, and shows a layer of 10 – 20 μm of small grains, 1 – 5 μm in diameter. These grains are also present in the grain boundaries of the larger austenite grains, up to a depth of 150 μm. Lastly, they are occasionally present at seemingly random sites within the larger austenite grains, and in straight lines which are likely twin boundaries in the larger austenite grains.

In Figure 49, the sample free surface near the LAZ-martensite interface, small grains of similar size dominantly populate the larger austenite grains, to the extent that these larger grains are still discernible, but almost completely subsumed by the small grains. The presence of these small grains is the reason for the darkest etched part of the upper layer near the interface, as seen in Figure 47, and this zone extends inwards from the interface, in this upper layer only, for about 400 μm. An area of 100 μm deep and 600 μm wide was analysed for a grain size measurement. The grain sizes in this region were measured using the approach described in section 3.6.1. The average grain size was found to be 21 μm. This average is a measure of the 'macro-grains' only, since the (sub-)micron grains could not be processed for a reliable measurement.

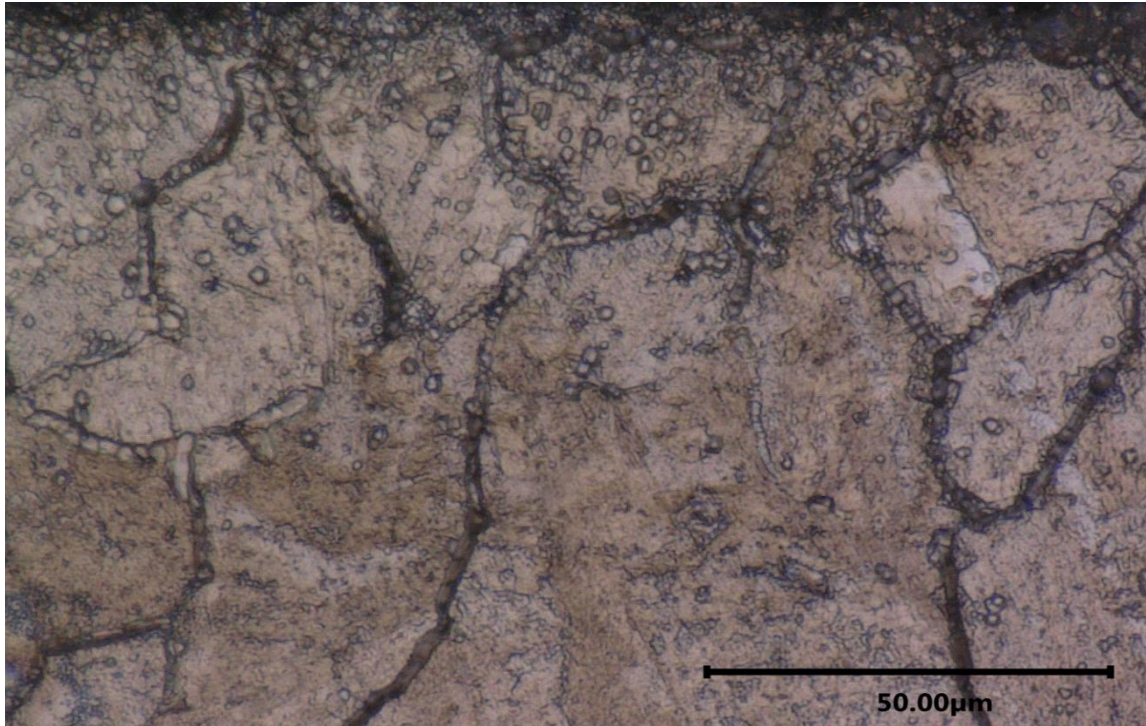


Figure 49: Specimen 4, free surface (upper edge) in the centre of the LAZ. In grain boundaries and the free surface, the (sub-)micron grains are clearly visible.

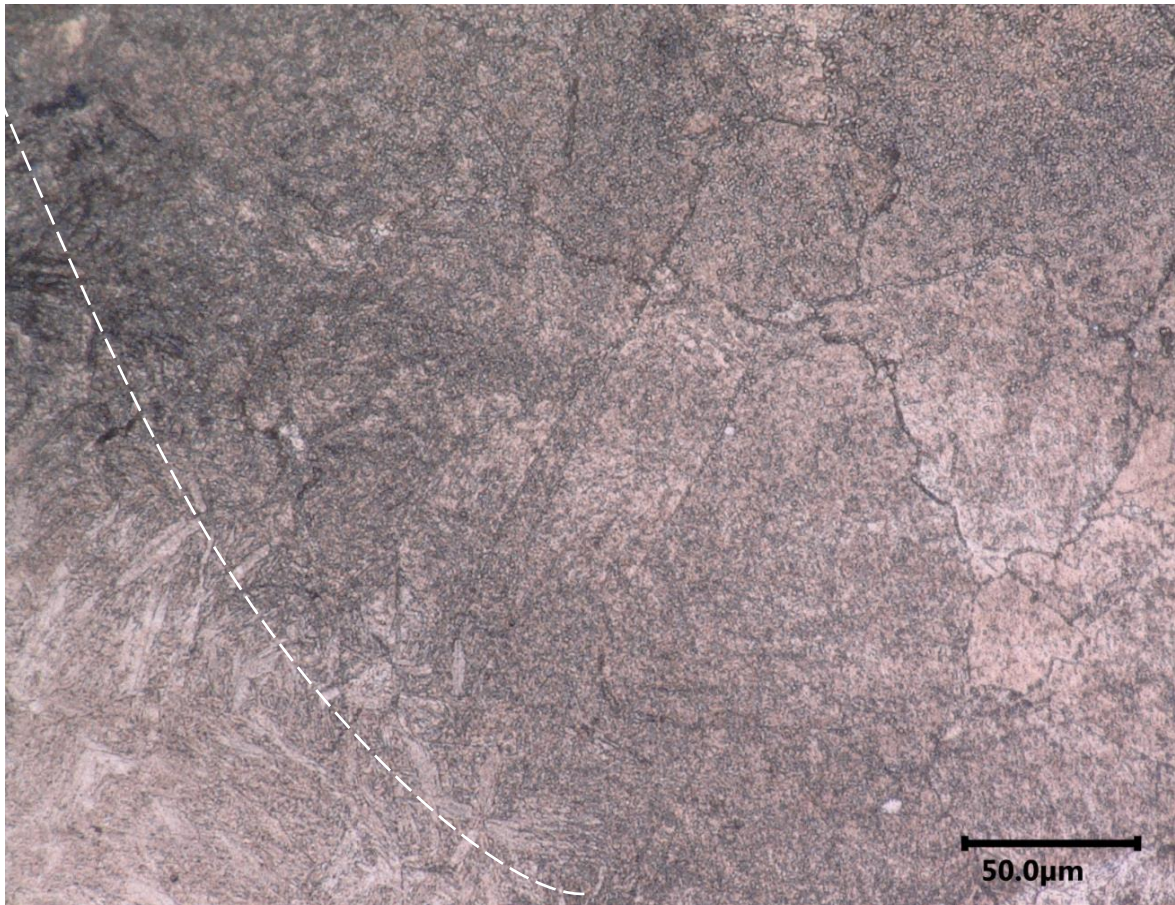


Figure 48: Specimen 4, free surface (upper edge) near the interface (dashed line) between the LAZ and the martensitic bulk

Middle region

The second region in specimen 4, shown in Figure 47 starting at a depth of 100 μm , and 150 μm deep, constitutes a gradual decrease in the presence and diameter of the smaller grains. In Figure 50, representative of the middle region, the grains in grain boundaries are still present, albeit smaller still, and at sub-micron sizes. For a section of the LAZ within this zone, 150 μm deep and 500 μm wide grains were measured to obtain an average grain size of 14 μm . Similarly to the top region, this is a representation of the macro-grain size only.

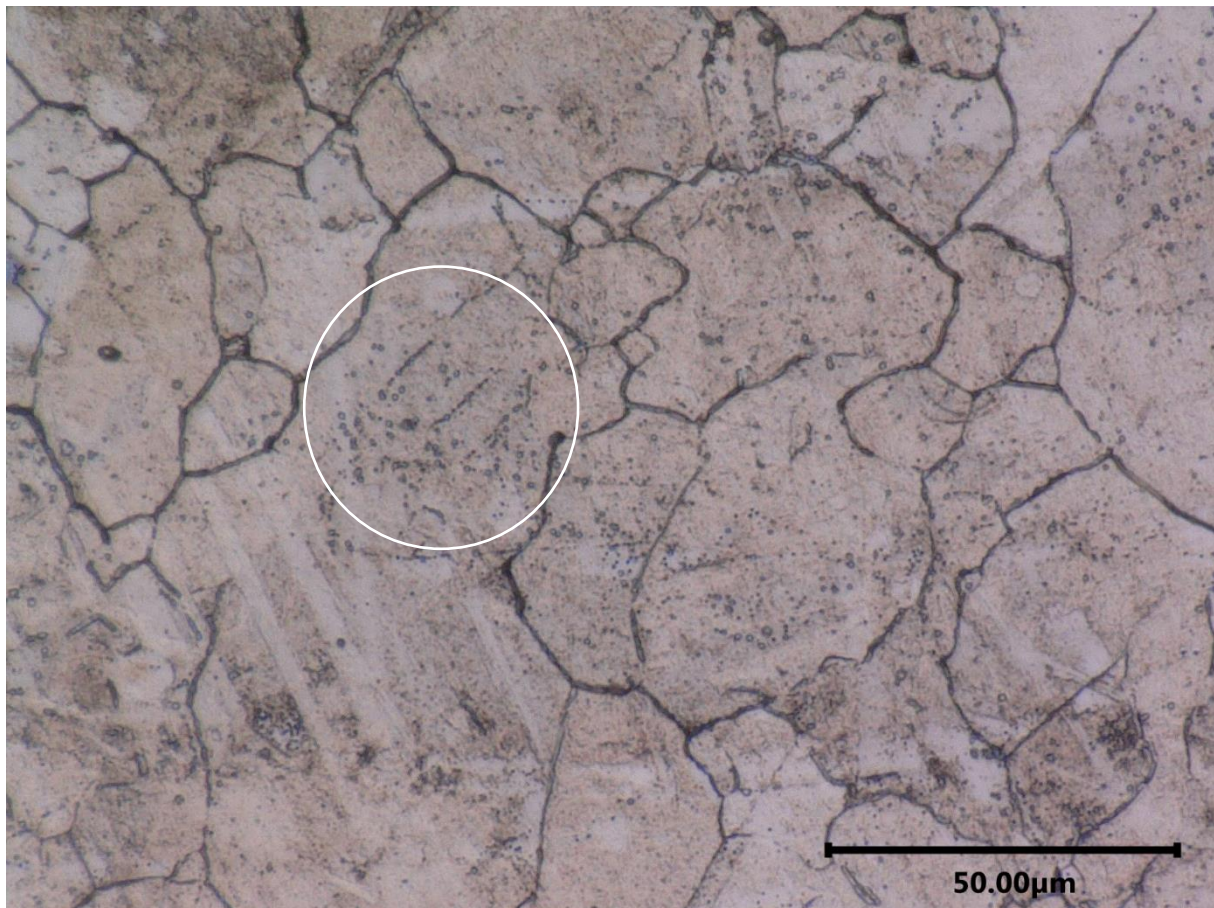


Figure 50: Specimen 4, middle region. A relatively even austenite grain size, with occasional colonies of the smaller grains, as shown in the white circle. Careful examination of grain boundaries shows a similar effect to the interface, with grain boundaries populated by small grains.

LAZ deep zone

The lower section of the LAZ, which starts at a depth of 250 μm from the specimen surface, is shown in Figure 51. This microstructure, shown here near the interface with the martensitic parent structure, is characterised by large austenite grains. The grain boundaries are reasonably completely revealed by the etchant, but are less pronounced than in either of the zones nearer to the interface. Therefore, the grain boundary effect of small grains is considered to not be extended to these depths. Notably, no small grains are observed near the interface either, although the interface had a strong effect on the presences of these grains in the upper layers. The grain size of austenite in this zone, measured over an area of 200 μm by 500 μm , was found to be 44 μm .



Figure 51: Deep zone, near the interface with martensitic parent structure (Dashed white line).

5.3.3. Hardness measurement of the high-power LAZ

Hardness measurements were carried out to further investigate the microstructural characteristics of the high-powered specimens. A spatial representation of these measurements can be seen in Figure 52. The hardness, in HV0.2, are represented as a colour map overlay of the micrograph also presented in Figure 47. These colour overlays represent two depth lines, from the centre of the LAZ straight down into the specimen, spaced 75 μm apart, and three lines along the specimen surface. The step size between consecutive measurements was also 75 μm, creating evenly spaced grids of hardness measurements in these two areas.

Hardness depth profile

In the upper region, low hardness is observed, in the order of 150-175 HV0.2. These low values are consistent across the depth line up to about 400 μm. The hardness increases rapidly between 400 and 500 μm to approx. 280 HV0.2. No notable increase in hardness is seen within the interface. Measurements taken at larger depth put hardness values of the martensitic parent material around 380 HV0.2.

Hardness surface profile

Along the surface, low hardness is observed in the range 100-150 μm deep, in the region nearest to the sample centre. The depth of the low hardness region gradually decreases, such that at a distance of 500 μm from the martensite interface, the hardness is around 240 HV0.2. This significantly higher hardness in the upper region is observed within the dark-etched zone, where the large austenite grains were almost completely subsumed by the small-grained structure.

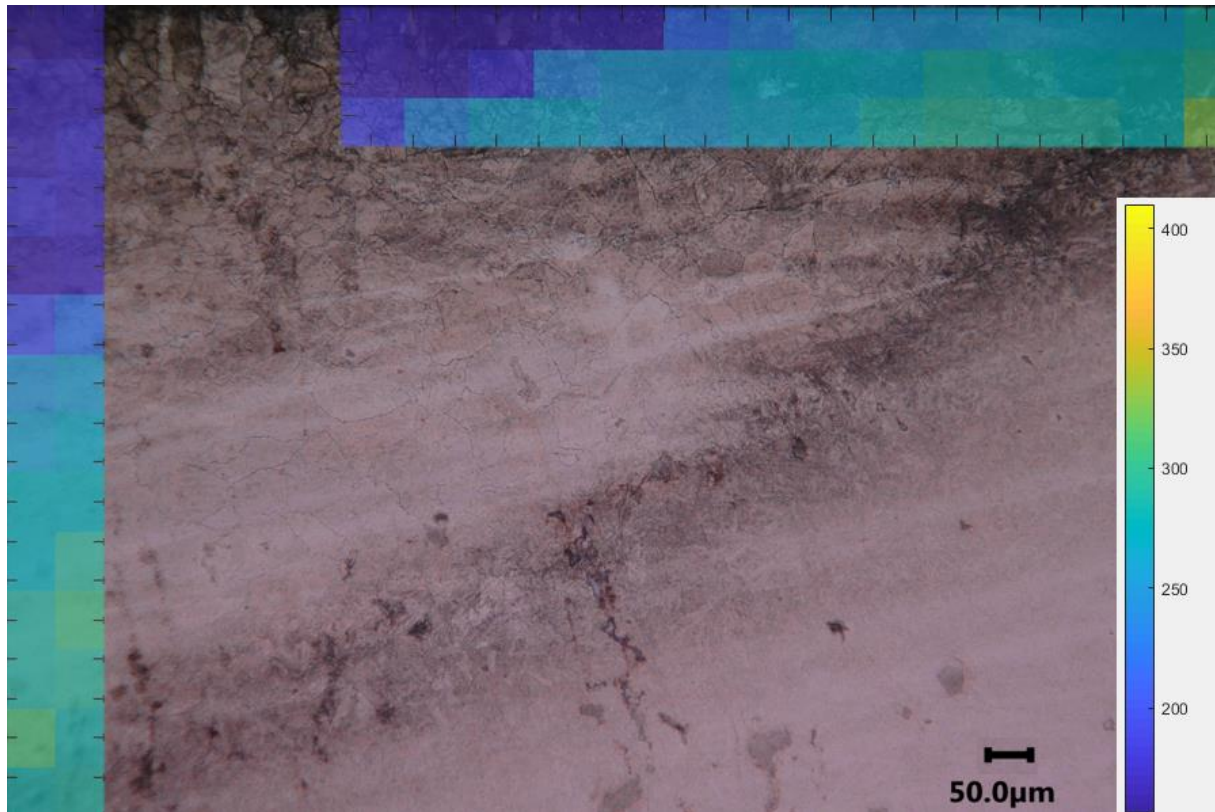


Figure 52: Hardness measurements along the interface and in sample depth for high-powered laser specimen 4. Hardness scale HV0.2. The tick-marks on the hardness maps represent a distance of 50 μm , and the pixel size is 75x75 μm .

5.4. Microstructural Discussion Laser specimens

5.4.1. Grain refinement phenomena

As presented in section 5.3.2, in the upper and middle region of the high-power sample, small grains, of the order of a few micron or smaller, are observed. These grains are present at austenite grain boundaries, such that these grain boundaries are predominantly subsumed by the (sub-)micron grains in the upper and the middle region in this specimen, up to a depth of 250 μm . Similar (sub-)micron grains are also observed in the sample free surface, as a small layer of 10-20 μm deep. Lastly, the region near the martensite interface in the upper region and part of the middle region of the specimen shows a very high density of the (sub-)micron grains, up to a depth of about 200 μm .

Grain boundary and free surface grain refinement in the centre of the LAZ

The presence of grain boundary and free surface (sub-)micron grains has been previously reported by Televich et al. [86, 87], studied in a complex alloy (Fe-0.35C-0.5Mn-0.25Si-3Ni-0.4Mo-1.2Cr-0.1V-0.02S-0.02P) at a heating rate of 300 K/s. In this alloy, an austenite reversion from martensite was studied with high-temperature XRD, to assess the X-ray diffraction pattern of the fine grained structure at the free interface of the sample. The authors conclude, based on diffraction patterns, that the formation of these grains takes place by an ordered $\alpha' \rightarrow \gamma$ transformation, with an orientation relation corresponding to $\{211\}_{\gamma} \parallel \{110\}_{\alpha'}$, $\langle 0\ 1\ 1 \rangle_{\gamma} \parallel \langle 1\ 1\ 2 \rangle_{\alpha'}$. This orientation relation is distinct from that in the “internal”, macro-grain austenite, which undergoes reestablishment of the previous austenite grain orientation

upon reversion from martensite. Based on this, the authors conclude that recrystallization does not play a role in this phenomenon and that large angle boundary surfaces provide a catalytic effect on the formation of these comparatively small grains.

The morphology described by Televich et al is similar to the LAZ microstructure observed in the central upper region of the high-power laser specimen. This would suggest that the transformation mechanism in this region is similarly ordered, with an interface-catalysed formation of the (sub-)micron grains, followed by displacive transformation in the internal grain to restore previous austenite grain size. An explanation for the observed reduction in austenite grain size in this region, relative to the initial austenite grain size before cryogenic quenching, can be found in the population of twin boundaries of the previous austenite grains by the (sub-)micron grains. Grain boundaries populated by the (sub-)micron grains were included in the grain size measurement, whereas for the initial austenite grain size measurement, twin boundaries were disregarded [67].

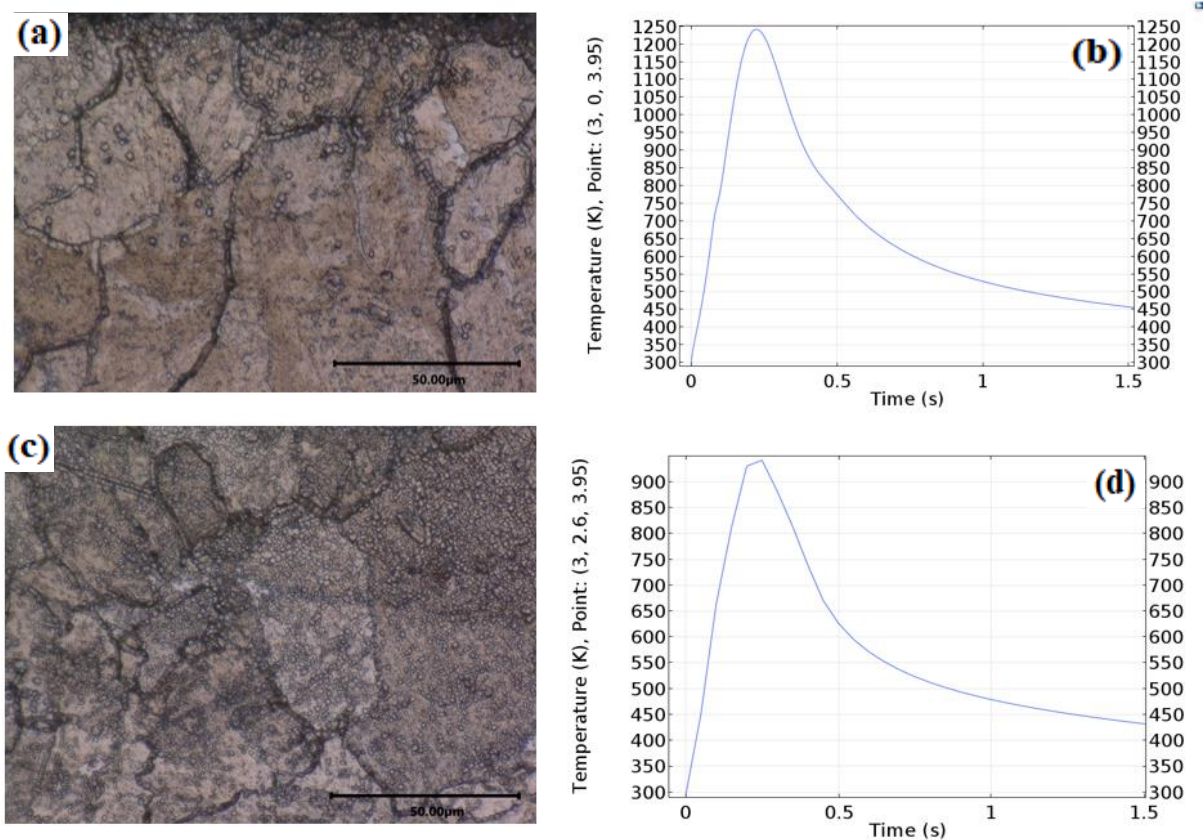


Figure 53: Comparison of Microstructures and Heating rates in the upper region. The top row shows the sample centre at a depth of 50 micron (a) and the thermal history there (b). The bottom row shows the region near the martensite interface (c), at the same depth, and its thermal history (d).

The centre of the upper region is shown in Figure 53a, accompanied by the model-estimated thermal history, shown in Figure 53b. The estimated heating rate in this zone is 6000 K/s, up to a peak temperature of 1230 K. For heating rates of this order, Figure 28, the dilatometric measurements carried out by Apple and Krauss [4], shows results that suggest a (partially) displacive mechanism for austenite reversion, which agrees with the hypothesis formulated based on the microstructure of the high-power sample and the conclusions of Televich et al. [86].

Martensite interface-adjacent grain refinement

Near the martensitic interface, an additional grain refinement phenomenon was observed. In this region, the macro-grain structure in the austenite is visible due to the grain boundary effect, but internally, these macro-grains are nearly completely subsumed by (sub-)micron grains of similar size and morphology to the free surface and grain boundary grains, as seen in Figure 53c. It is evident from the ubiquity of the (sub-)micron grains that, contrary to Televich's conclusions, boundary surfaces are not a significant contributor to their formation. Their presence, significant within 500 μm from the interface, suggests a long range effect of this interface in the high-power samples.

Based on results by Bailey et al. [43], modelling residual stresses in laser surface hardening, the interface of a laser affected zone is a region with a high residual stress gradient. These stresses are caused mostly by thermal and volumetric dilatation strains. Analogous stress concentrations are to be expected in the high-power specimen, although their precise distribution is speculative, since the findings by Bailey are based on an austenite to martensite transition. The stresses near the martensitic interface in this work would represent a significant driving force for recrystallization, leading to the grain refinement in this region. This would require the assumption, however, that despite similarities in size and morphology, the (sub-)micron grains in this region that are not situated on grain boundaries are formed by a different mechanism.

The thermal history, shown in Figure 53d, shows a heating rate of 4650 K/s, to a peak temperature of 930 K. This heating rate is of the same order as the centre of the sample, albeit slightly lower, suggesting the same formation mechanism for both the grain boundary (sub-)micron grains, and the macro-grains. The (partially) displacive-formed macro grains near the interface, containing higher dislocation densities than those nearer the centre of the LAZ, due to the added interface stresses, can then be concluded to have a very high driving force for recrystallization. If the assumptions on mechanism and interface effect, for which at the moment little experimental evidence besides the observed microstructures and literature, hold, it can be concluded that recrystallization takes place with a high nucleation rate, creating the large amount of (sub-)micron grains.

Low power grain refinement

A dissimilar grain refinement effect is observed in the low-power specimen, where the EBSD profile, presented in Figure 45, shows a small-grained austenite region in the upper zone. This region is characterized by a high twin boundary density and a grain size which, while not (sub-)micron in order, is significantly smaller than the austenite grain size in the bulk of the low-power specimen LAZ. Figure 54 shows the modelled thermal history of the refined-grain region, at a depth of 100 μm . The peak temperature reached here was 1600 K, and the heating rate 8750 K/s. At somewhat higher depths, where the grain refinement effect is not observed, heating rates are of the order of 7500 K/s. Throughout most of the low-power specimen, modelled heating rates are significantly higher than in the high-power specimen. Since the grain boundary effect is not observed in the low-power specimen, the higher heating rate may be suppressing the catalytic effect of the grain boundaries, creating large grains by a displacive transformation. At the surface, where the microstructure is at an elevated temperature comparatively long, this dislocation structure inherited from the martensite during displacive austenite reversion might have been sufficient for substantial recrystallization in this upper region.

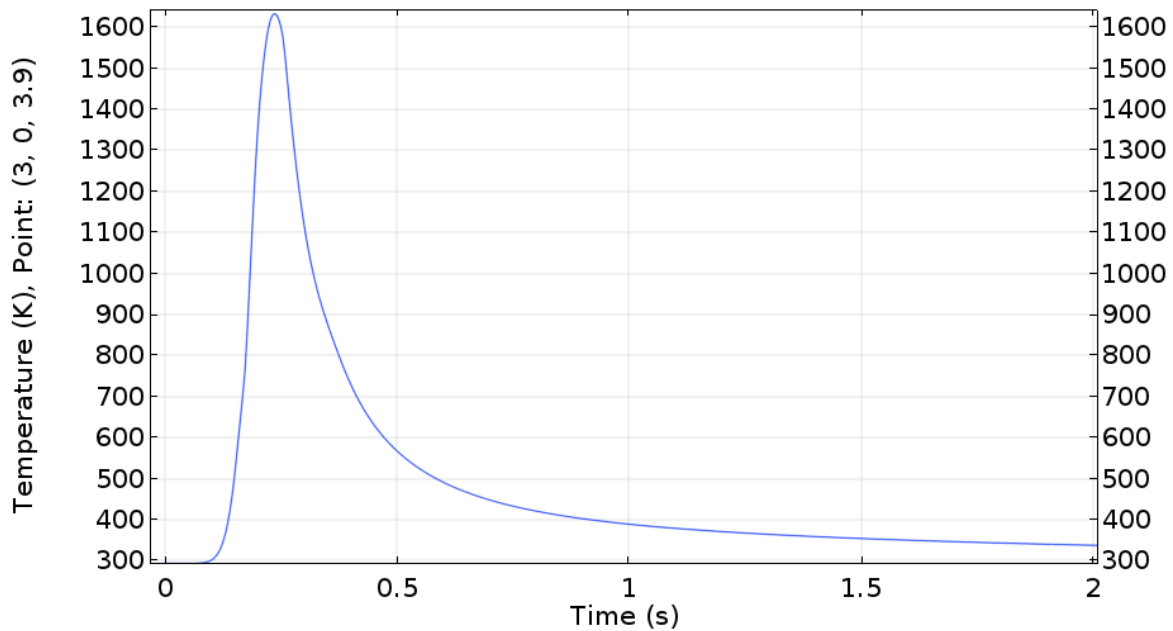


Figure 54: Model thermal history of low-power sample, in the centre of the LAZ, at a depth of 100 μm .

5.4.2. Low hardness near specimen free surface

The laser affected zone shows, in both the low-power and the high-power case, a distinct low hardness region near its free surface. In the high-power specimen, the depth up to which the low hardness values are observed correspond roughly to the upper and middle regions defined in Section 5.4.3. These regions are characterized by the prominent presence and gradual decrease in the (sub-)micron grains found in the grain boundaries, respectively. Furthermore, while slight differences are observed between the two in grain size, the average grain sizes of the macro-grains are significantly lower than those observed in the deep region, where higher hardness is measured. This contravenes the correlation between grain size and hardness that is generally observed in steels, where grain refinement leads to higher hardness [88]. The microstructural observations on the high-powered laser specimen are summarized in Table 12.

In the low-power specimen, low hardness values as demonstrated in Figure 43c, are only present near the interface, at a depth of 50-100 μm . This depth corresponds to a fine-grained region observed in the EBSD profile of the low-power laser line. The microstructure in this narrow region is relatively small-grained, compared to the rest of the sample, as demonstrated by the EBSD profile in Figure 45. Additionally, some massive martensite was observed at the surface. Here, the same discrepancy between refined grain structure and low hardness is observed. Whether the surface martensite has an effect on the hardness measured here can't be resolved, due to its proximity to a free interface. However, any contribution from the martensite would be expected to increase the hardness in this region, based on its high hardness as measured in the bulk martensite.

Table 12: Summary of Microstructural results for the high-powered laser specimen

	Grain Size (macro-grains)	Sub-micron grains	Hardness
Upper central region,	21 μm	1-5 μm , abundant at grain boundaries and free surface	Approx. 160 HV0.2
Upper Interface α' region,	21 μm	1-5 μm , ubiquitous	Approx. 250 HV0.2
Middle region	14 μm	< 1 μm , mostly at grain boundaries	160 HV0.2
Deep region	44 μm	Not observed	250-290 HV0.2

Based on the following observations, a possible mechanism behind the low hardness region can be formulated:

- Free interface effect on hardness measurement: Although these measurements were taken near the free interface, which can adversely affect measurement quality, low hardness was consistent up to a large depth in the high-power sample. Furthermore, the surface profile in this specimen shows distinct regions of both low and high hardness.
- Microstructures in the low and high power samples are dissimilar, although both regions are characterized by a relatively low austenite grain size compared to the overall austenite grain size in their respective specimens.
 - Low power sample:
 - i. Free surface martensite
 - ii. Small-grained austenite (around 20 μm)
 - iii. High twin boundary density
 - High power sample
 - i. Free surface equiaxed (sub-)micron austenite
 - ii. Grain boundary equiaxed (sub-)micron austenite
 - iii. Gradual decrease in prevalence of these (sub-)micron features
 - iv. Macro-grain size 14-21 μm

Based on the absence of an experimental or microstructural effect as the cause of the low hardness region, the strengthening mechanisms related to dislocation density and solute content are regarded as the likely causes of the low hardness region. In the preceding section on the grain refinement phenomena, a hypothesis was formulated regarding recrystallization in the upper region of the low-power sample. The rearrangement of dislocations during recrystallization, followed by grain growth, would account for the reduction in hardness, as well as the relatively small grains, and the high twin boundary density. However, attribution of the low hardness effect to recrystallization alone is not feasible, due to the limited recrystallization in the low hardness region of the high-power sample. The supposed recrystallization in the near-interface region of the high power sample, conversely, shows an increase in hardness, due to grain boundary strengthening. Therefore, a decrease in solute strengthening by decarburisation is more likely to be a significant contributor to this effect.

6. Conclusions

In conclusion, a short summary of this work can be given, and some main findings can be stated, subdivided by the aspects of this work.

The microstructural characteristics of Laser Austenitized Zones (LAZ) in cryogenically formed martensitic microstructures of a metastable austenitic steel were investigated. This investigation was carried out by:

- A dilatometric study, to assess the behaviour of the martensite-to-austenite reversion which is also observed during the laser heat treatment.
- A thermal model of the laser heat treatment.
- A microstructural characterisation of laser treated samples of two types:
 - Low power, small laser spot experiments.
 - High power, large laser spot experiments.

In the laser treated samples, microstructural characteristics were found that could not be fully rationalized by the thermal history estimated by the model. Nevertheless, based on observations and literature sources, hypotheses regarding the microstructural formation could be formulated.

Dilatometry

1. Heating rates have a distinct influence on martensite-to-austenite reversion temperatures in Fe-0.2C-25Ni in the range from 5 to 1000 K/s.
2. At these heating rates, no evidence is found for the onset of a (partially) displacive mechanism for the reversion.
3. Hollow samples behave similarly in conventional heating rate experiments and can be used to attain data at higher heating rates than solid samples.
4. Upon cooling, hollow dilatometry samples display the onset of martensitic transformation.
 - a. Martensite formation is observed to take place in a surface layer, suggesting the contribution of a free surface effect.
 - b. Decarburization was found to be significant in the hollow samples.
5. Hollow dilatometry specimens highlight the prominent effect of free surfaces and decarburization on martensitic transformation, and results in the formation of a martensitic surface layers. These effects of free surface and decarburization will play a significant role in laser processes in thin specimens and foils, and must therefore be carefully considered.

Model

1. A valid thermal model for a solid state laser surface treatment was created, using transient properties and implementing a phase change hysteresis.
 - a. Extent of laser affected zones were slightly overestimated, up to approx. 10% in most cases
 - b. Heating rates and peak temperatures showed close correspondence for the thermocouples at the same side of the laser heat flux, and a distinct underestimation of both parameter when compared to thermocouples at the far side of the laser specimen.
2. A sensitivity analysis show that absorptivity has a strong influence on heating rates experienced within a modelled specimen.
3. The implemented phase change hysteresis is not attempted in any literature source and is shown in the sensitivity analysis to affect heating rates at large distances to the laser spot significantly, and non-linearly.

Localised Laser Heat Treatment

1. During localised laser heat treatments, significant microstructural variation is observed over short distances.
 - a. In high-power experiments, three zones are observed.
 - i. In the region near the free surface (sub-)micron grains are observed along grain boundary surfaces of larger austenite grains and in the free interface. The formation mechanism is assumed to be by ordered transformation.
 - ii. Near the martensitic interface, large amounts of (sub-)micron grains are observed in the grain interior of austenite grains, while also exhibiting the grain boundary effect. These grains may be formed by recrystallization, under the influence of significant interface stresses caused by dilatation.
 - iii. In deeper regions, large austenite grains are observed.
 - b. In low-power experiments, a distinct grain refinement and limited martensite formation is observed at the sample surface.
2. Austenite formed by reversion at the extremely high heating rates experienced in laser treatments shows microstructural characteristics strongly dissimilar to those formed by dilatometry at conventional or high heating rates.
3. Differences within the laser affected zone are not explained sufficiently by the local thermal history supplied by the model.
4. Martensite in the interface between the laser-affected zone and the as-quenched parent material is stabilised by carbide precipitation during the laser heat treatment, rather than formed under the influence of near-interface strain.

7. Recommendations

Based on the conclusions and observations from this work, some recommendations can be made for future research in this area.

Model

1. The latent heat of phase transformation in these treatments, assessed by detailed calorimetric studies, is advisable. This will elucidate the effect of the phase change hysteresis in the model.
2. The absorptivity and its relation to surface properties should be considered carefully in further attempts to predict the laser austenitized zone.
3. The physics-based modelling in this work lends itself to prediction of temperature field in samples of the same material, but different geometry. It should be noted here, however, that heating rate, peak temperature, and decarburisation might result in strong effects on obtained microstructures, such that they are not necessarily comparable to the microstructures described in this work. Pronounced differences can be expected in e.g. thin samples, where the LAZ penetrates the entire sample.

Dilatometry

1. Further dilatometry studies on this alloy, at even higher heating rates, may corroborate the measurements by Apple and Krauss, and would be valuable for further understanding of the localised laser heat treatments.
2. Dilatometry studies assessing the effect of high heating rates to intercritical temperatures would be of interest to a further study of the interface between martensitic parent material and the laser-formed austenite.

Localised Laser Heat Treatments

1. Using the model, localised laser heat treatments can be designed with reasonable confidence. This lends itself to the prediction of size and shape of the LAZ in complex architected structures, or in work pieces with different geometries.
2. A targeted investigation into the 'grain boundary' sub-micron grain effect can be carried out using the alloy and laser heat treatment considered in this work, and its possible connection to the sub-micron grains observed near the martensitic interface. In-situ EBSD measurements using high heating rates would be ideal, but likely not feasible.
3. An EPMA analysis of carbon distribution in these samples, when subjected to laser treatment in air, would yield valuable information regarding the decarburisation behaviour during the localised laser heat treatments, and carbon redistribution within the LAZ at high heating rates and short heating times.
4. Microstructures formed by multi-pass or interlaced localised laser heat treatments are in interesting area for further investigation, provided the single-pass microstructural mechanisms are understood. This research should be carried out to facilitate the creation of entirely austenitized surface layers by the treatment used in this work.

8. Bibliography

- [1] A. J. Bierens, P. P. Van Houten, H. Lanwehr, and J. A. Reijne, "Architected Steel Microstructures by Laser Treatment," June 5th 2018.
- [2] R. Honeycombe and H. Bhadeshia, *Steels, Microstructure and Properties, Metallurgy and Materials Science*. Edward Arnold Butterworth Heinemann, London, England, 1995.
- [3] L. Swartzendruber, V. Itkin, and C. Alcock, "The Fe-Ni (iron-nickel) system," *Journal of phase equilibria*, vol. 12, no. 3, pp. 288-312, 1991.
- [4] C. A. Apple and G. Krauss, "The effect of heating rate on the martensite to austenite transformation in Fe-Ni-C alloys," *Acta metallurgica*, vol. 20, no. 7, pp. 849-856, 1972.
- [5] M. Picasso and A. F. A. Hoadley, "Finite element simulation of laser surface treatments including convection in the melt pool," *International Journal of Numerical Methods for Heat & Fluid Flow*, vol. 4, no. 1, pp. 61-83, 1994.
- [6] J. Mazumder, "Laser heat treatment: the state of the art," *JOM*, vol. 35, no. 5, pp. 18-26, 1983.
- [7] A. O. Andreev *et al.*, "Effect of the laser heat treatment on the formation of the gradient structures in alloys based on Fe – Cr – Ni system," *Journal of Physics: Conference Series*, vol. 941, p. 012027, 2017.
- [8] A. Järvenpää, M. Jaskari, M. Hietala, and K. Mäntyjärvi, "Local Laser Heat Treatments of Steel Sheets," *Physics Procedia*, vol. 78, pp. 296-304, 2015.
- [9] P. Lehtinen, T. Väisänen, and M. Salmi, "The Effect of Local Heating by Laser Irradiation for Aluminum, Deep Drawing Steel and Copper Sheets in Incremental Sheet Forming," *Physics Procedia*, vol. 78, pp. 312-319, 2015.
- [10] A. Andreev, M. Galkin, M. Libman, V. Mironov, V. Petrovskii, and E. Éstrin, "Use of laser heat treatment for creating gradient materials based on the Fe–Cr–Ni system," *Metal Science and Heat Treatment*, vol. 56, no. 1-2, pp. 53-56, 2014.
- [11] T. Chiba, H. Shirazi, G. Miyamoto, and T. Furuhashi, "Grain Refinement by Cyclic Displacive Forward/Reverse Transformation in Fe-High-Ni Alloys," *Metallurgical and Materials Transactions A*, vol. 48, no. 9, pp. 4204-4210, 2017.
- [12] A. Levin *et al.*, "Creating a gradient material for aviation generators," *Steel in Translation*, vol. 38, no. 9, pp. 786-790, 2008.
- [13] D. Embury and O. Bouaziz, "Steel-Based Composites: Driving Forces and Classifications," *Annual Review of Materials Research*, vol. 40, no. 1, pp. 213-241, 2010.
- [14] P. Jacques, F. Delannay, and J. Ladrière, "On the influence of interactions between phases on the mechanical stability of retained austenite in transformation-induced plasticity multiphase steels," *Metallurgical and materials transactions A*, vol. 32, no. 11, pp. 2759-2768, 2001.
- [15] J. Hidalgo, R. M. Huizenga, K. Findley, and M. Santofimia, "Interplay between metastable phases controls strength and ductility in steels," *Materials Science and Engineering A*, vol. 745, pp. 185-194, 02/02 2019.
- [16] M. Libman and E. Estrin, "Stability of the high-temperature phase in composites with a specified distribution of ferromagnetic and paramagnetic regions," *Steel in Translation*, vol. 44, no. 10, pp. 779-781, 2014.
- [17] S. Y. Lim and C. R. Chatwin, "Spatial chaos aspects of laser-material interaction," *Optics and lasers in engineering*, vol. 20, no. 5, pp. 341-356, 1994.
- [18] G. R. Römer, "Modelling and control of laser surface treatment," Doctoral Thesis, University of Twente, 1999.
- [19] R. G. Thiessen, "Physically-based modelling of material response to welding," Doctoral, Material Science and Engineering, Delft University of Technology, 2006.

- [20] J. Mazumder and W. Steen, "Heat transfer model for CW laser material processing," *Journal of Applied Physics*, vol. 51, no. 2, pp. 941-947, 1980.
- [21] M. M. Pariona, F. de Oliveira, V. Teleginski, S. Machado, and M. A. V. Pinto, "Simulation and optimization of Al-Fe aerospace alloy processed by laser surface remelting using geometric Multigrid solver and experimental validation," *Heat and Mass Transfer*, vol. 52, no. 5, pp. 1037-1049, 2016.
- [22] S. V. Telrandhe, J. Bhagyaraj, S. Mishra, and S. Karagadde, "A new approach to control and optimize the laser surface heat treatment of materials," *Journal of Materials Processing Technology*, vol. 262, pp. 492-502, 2018.
- [23] H. Shirazi, G. Miyamoto, S. Hossein Nedjad, T. Chiba, M. Nili Ahmadabadi, and T. Furuhashi, "Microstructure evolution during austenite reversion in Fe-Ni martensitic alloys," *Acta Materialia*, vol. 144, pp. 269-280, 2018.
- [24] X. Zhang, G. Miyamoto, T. Kaneshita, Y. Yoshida, Y. Toji, and T. Furuhashi, "Growth mode of austenite during reversion from martensite in Fe-2Mn-1.5Si-0.3C alloy: A transition in kinetics and morphology," *Acta Materialia*, vol. 154, pp. 1-13, 2018.
- [25] X. Zhang, G. Miyamoto, Y. Toji, and T. Furuhashi, "Effects of Heating Rate on Formation of Globular and Acicular Austenite during Reversion from Martensite," *Metals*, vol. 9, no. 2, p. 266, 2019.
- [26] V. N. Gridnev, "Evolution and Modern Ideas of Martensitic Transformations Reversibility," *Soviet Scientific Reviews A Physics*, vol. 10, pp. 133-165, 1989.
- [27] Y. Y. Meshkov and E. V. Pereloma, "The effect of heating rate on reverse transformations in steels and Fe-Ni-based alloys," in *Phase Transformations in Steels*, 2012, pp. 581-618.
- [28] V. I. Savran, "Austenite formation in C-Mn steel," 2009.
- [29] "COMSOL Multiphysics® v. 5.3a", ed. Stockholm, Sweden: COMSOL AB.
- [30] B. Wilthan, W. Schützenhöfer, and G. Pottlacher, "Thermal Diffusivity and Thermal Conductivity of Five Different Steel Alloys in the Solid and Liquid Phases," *International Journal of Thermophysics*, vol. 36, no. 8, pp. 2259-2272, 2015.
- [31] D. Bergström, "The absorption of laser light by rough metal surfaces," Doctoral Thesis, Luleå tekniska universitet, 2008.
- [32] A. P. Mackwood and R. C. Crafer, "Thermal modelling of laser welding and related processes: a literature review," *Optics & Laser Technology*, vol. 37, no. 2, pp. 99-115, 2005.
- [33] R. Vilar, "Laser surface modification of steel and cast iron for corrosion resistance," pp. 3-40, 2012.
- [34] S. I. Anisimov and B. Rethfeld, "Theory of ultrashort laser pulse interaction with a metal," in *Nonresonant Laser-Matter Interaction (NLMI-9)*, 1997, vol. 3093, pp. 192-204: International Society for Optics and Photonics.
- [35] D. R. Poirier and G. Geiger, *Transport phenomena in materials processing*. Springer, 2016.
- [36] J. C. Ion, H. R. Shercliff, and M. F. Ashby, "Diagrams for laser materials processing," *Acta Metallurgica et Materialia*, vol. 40, no. 7, pp. 1539-1551, 1992.
- [37] D. Rosenthal, "The theory of moving sources of heat and its application of metal treatments," *Transactions of ASME*, vol. 68, pp. 849-866, 1946.
- [38] A. Nunes, "An extended Rosenthal weld model," *Welding journal*, vol. 62, no. 6, pp. 165s-170s, 1983.
- [39] M. Ashby and K. E. Easterling, "The transformation hardening of steel surfaces by laser beams—I. Hypo-eutectoid steels," *Acta metallurgica*, vol. 32, no. 11, pp. 1935-1948, 1984.
- [40] W.-B. Li, K. E. Easterling, and M. Ashby, "Laser transformation hardening of steel—II. Hypereutectoid steels," *Acta Metallurgica*, vol. 34, no. 8, pp. 1533-1543, 1986.
- [41] H. R. Shercliff and M. Ashby, "The prediction of case depth in laser transformation hardening," *Metallurgical Transactions A*, vol. 22, no. 10, pp. 2459-2466, 1991.
- [42] D. Gnanamuthu, "Laser surface treatment," *Optical Engineering*, vol. 19, no. 5, p. 195783, 1980.

- [43] N. S. Bailey, W. Tan, and Y. C. Shin, "Predictive modeling and experimental results for residual stresses in laser hardening of AISI 4140 steel by a high power diode laser," *Surface and Coatings Technology*, vol. 203, no. 14, pp. 2003-2012, 2009/04/15/ 2009.
- [44] T. Mioković, V. Schulze, O. Vöhringer, and D. Löhe, "Prediction of phase transformations during laser surface hardening of AISI 4140 including the effects of inhomogeneous austenite formation," *Materials Science and Engineering: A*, vol. 435-436, pp. 547-555, 2006.
- [45] R. Patwa and Y. C. Shin, "Predictive modeling of laser hardening of AISI5150H steels," *International Journal of Machine Tools and Manufacture*, vol. 47, no. 2, pp. 307-320, 2007.
- [46] L. Orazi, A. Fortunato, G. Cuccolini, and G. Tani, "An efficient model for laser surface hardening of hypo-eutectoid steels," *Applied Surface Science*, vol. 256, no. 6, pp. 1913-1919, 2010.
- [47] T. Mioković, J. Schwarzer, V. Schulze, O. Vöhringer, and D. Löhe, "Description of short time phase transformations during the heating of steels based on high-rate experimental data," in *Journal de Physique IV (Proceedings)*, 2004, vol. 120, pp. 591-598: EDP sciences.
- [48] J. Goldak, A. Chakravarti, and M. Bibby, "A new finite element model for welding heat sources," *Metallurgical transactions B*, vol. 15, no. 2, pp. 299-305, 1984.
- [49] I. Kozelkova, C. Dagbert, P. Gregoire, J. Galland, and L. Hyspecka, "Kinetics of austenite to martensite transformations in iron-nickel-carbone alloys during their cooling or tensile testing," *Le Journal de Physique IV*, vol. 5, no. C8, pp. C8-323-C8-328, 1995.
- [50] N. Fonstein, *Advanced high strength sheet steels: physical metallurgy, design, processing, and properties*. Springer, 2015.
- [51] M. F. McGuire, *Stainless steels for design engineers*. Asm International, 2008.
- [52] D. A. Porter, K. E. Easterling, and M. Sherif, *Phase Transformations in Metals and Alloys, (Revised Reprint)*. CRC press, 2009.
- [53] H. Sato and S. Zaefferer, "A study on the formation mechanisms of butterfly-type martensite in Fe-30% Ni alloy using EBSD-based orientation microscopy," *Acta Materialia*, vol. 57, no. 6, pp. 1931-1937, 2009.
- [54] C. Dagbert, M. Sehili, P. Gregoire, J. Galland, and L. Hyspecká, "Mechanical study of instability of austenitic FeNiC alloys—Effect of hydrogen," *Acta materialia*, vol. 44, no. 7, pp. 2643-2650, 1996.
- [55] J. Hidalgo, K. O. Findley, and M. J. Santofimia, "Thermal and mechanical stability of retained austenite surrounded by martensite with different degrees of tempering," *Materials Science and Engineering: A*, vol. 690, pp. 337-347, 2017.
- [56] L. Kaufman and M. Cohen, "The martensitic transformation in the iron-nickel system," *JOM*, vol. 8, no. 10, pp. 1393-1401, 1956.
- [57] D. De Knijf, C. Föjer, L. A. Kestens, and R. Petrov, "Factors influencing the austenite stability during tensile testing of Quenching and Partitioning steel determined via in-situ Electron Backscatter Diffraction," *Materials Science and Engineering: A*, vol. 638, pp. 219-227, 2015.
- [58] H. Kessler and W. Pitsch, "On the nature of the martensite to austenite reverse transformation," *Acta Metallurgica*, vol. 15, no. 2, pp. 401-405, 1967.
- [59] J.-O. Andersson, T. Helander, L. Höglund, P. Shi, and B. Sundman, "Thermo-Calc & DICTRA, computational tools for materials science," *Calphad*, vol. 26, no. 2, pp. 273-312, 2002.
- [60] S. Software Ltd and J. Hu, *JMatPro Flyer*. 2015.
- [61] G. Mohapatra, "Phase transformation kinetics: the role of stress," 2006.
- [62] J. D'Errico, "Shape Language Model ", 1.14 ed: Mathworks File Exchange, 2017, p. Least squares spline modeling using shape primitives.
- [63] J. O. Ramsay, "Monotone regression splines in action," *Statistical science*, vol. 3, no. 4, pp. 425-441, 1988.

- [64] "MATLAB," R2018b ed. Natick, Massachusetts: The Mathworks Inc. , 2018.
- [65] G. F. Vander Voort, *Metallography, principles and practice*. ASM International, 1999.
- [66] P. Lehto, H. Remes, T. Saukkonen, H. Hänninen, J. J. M. S. Romanoff, and E. A, "Influence of grain size distribution on the Hall–Petch relationship of welded structural steel," vol. 592, pp. 28-39, 2014.
- [67] G. F. Vander Voort, "Color metallography," *Microscopy Today*, vol. 13, no. 6, pp. 22-27, 2005.
- [68] B. Sjodin, "What's The Difference Between FEM, FDM, and FVM? ," in *Technologies: FEA and Simulation*, ed: www.machinedesign.com, 2016.
- [69] M. Tabatabaian, *COMSOL5 for Engineers*. Stylus Publishing, LLC, 2015.
- [70] C. Grossmann, H.-G. Roos, and M. Stynes, *Numerical treatment of partial differential equations*. Springer, 2007.
- [71] T. Chung, *Computational fluid dynamics*. Cambridge university press, 2010.
- [72] C. Vuik, P. Van Beek, F. Vermolen, and J. Van Kan, "Numerieke methoden voor differentiaalvergelijkingen," ed: VSSD, 2006.
- [73] C. Multiphysics, "Comsol multiphysics reference manual," *COMSOL: Grenoble, France*, p. 1084, 2013.
- [74] R. LeSar, *Introduction to computational materials science: fundamentals to applications*. Cambridge University Press, 2013.
- [75] R. Indhu, V. Vivek, L. Sarathkumar, A. Bharatish, and S. Soundarapandian, "Overview of Laser Absorptivity Measurement Techniques for Material Processing," *Lasers in Manufacturing and Materials Processing*, vol. 5, no. 4, pp. 458-481, 2018.
- [76] R. J. Naumann, *Introduction to the Physics and Chemistry of Materials*. CRC Press, 2008.
- [77] *Thermal properties of metals* (ASM ready reference). Materials Park: ASM International, 2002.
- [78] A. G. f. A. R. North Atlantic Treaty Organization and Development, *Material properties handbook. Vol. 2, Steels*. London: Royal Aeronautical Society, 1958.
- [79] "Appendix A - Thermophysical Properties of Materials," in *Process Heat Transfer (Second Edition)*, R. W. Serth and T. G. Lestina, Eds. Boston: Academic Press, 2014, pp. 555-580.
- [80] H.-S. Yang and H. Bhadeshia, "Uncertainties in dilatometric determination of martensite start temperature," *Materials Science and Technology*, vol. 23, no. 5, pp. 556-560, 2007.
- [81] Z. Guo, N. Saunders, A. P. Miodownik, and J. P. Schillé, "Modelling of materials properties and behaviour critical to casting simulation," *Materials Science and Engineering: A*, vol. 413-414, pp. 465-469, 2005.
- [82] J. S. Chickos, "A protocol for correcting experimental fusion enthalpies to 298.15 K and it's application in indirect measurements of sublimation enthalpy at 298.15 K," *Thermochimica acta*, vol. 313, no. 1, pp. 19-26, 1998.
- [83] N. Scheerlinck, K. Fikim, P. Verboven, J. De Baerdemaeker, and B. Nicolaï, "Numerical solution of phase change heat transfer problems with moving boundaries using an improved finite element enthalpy method," *WIT Transactions on Modelling and Simulation*, vol. 18, 1997.
- [84] C. Graham, B. Lorenz, M. Citrin, D. Greenstein, and R. Xu, "Reversion of Martensite in 304 Stainless Steel Studied by Dilatometry and Calorimetry," *Journal of Material Science & Engineering*, vol. 07, no. 02, 2018.
- [85] Y. U. Wang, Y. M. Jin, and A. G. Khachaturyan, "The effects of free surfaces on martensite microstructures: 3D phase field microelasticity simulation study," *Acta Materialia*, vol. 52, no. 4, pp. 1039-1050, 2004.
- [86] R. Televich, O. Kocherga, S. Prikhod'ko, and E. Yakushechkin, "Crystallographic Pattern of Near-Interface Austenite Formation," *Phys. Met.(Ukraine)*, vol. 13, no. 9, pp. 1160-1167, 1991.
- [87] R. Televich and S. Prikhod'ko, "Formation of Austenite Structure in Prequenched Alloy Steels", " 1994.

- [88] J. Morris, "The influence of grain size on the mechanical properties of steel," Lawrence Berkeley National Lab.(LBNL), Berkeley, CA (United States)2001.